5-2018

Analysis of a High-Temperature Spectroscopic Gas Cell Design

Travis Lee Johnson
University of Tennessee

To the Graduate Council:

I am submitting herewith a thesis written by Travis Lee Johnson entitled "Analysis of a High-Temperature Spectroscopic Gas Cell Design." I have examined the final electronic copy of this thesis for form and content and recommend that it be accepted in partial fulfillment of the requirements for the degree of Master of Science, with a major in Aerospace Engineering.

Trevor M. Moeller, Major Professor

We have read this thesis and recommend its acceptance:

Christopher S. Combs, Feng-Yuan Zhang

Accepted for the Council:
Dixie L. Thompson

Vice Provost and Dean of the Graduate School

(Original signatures are on file with official student records.)

Analysis of a High-Temperature Spectroscopic Gas Cell Design

A Thesis Presented for the

Master of Science

Degree

The University of Tennessee, Knoxville

Travis Lee Johnson

May 2018

Dedication

I dedicate this work to my parents and family for supporting me and believing in me and to all my friends who have encouraged me along the way.

Acknowledgments

I would like to thank the Test Resource Management Center (TRMC) Test & Evaluation/Science & Technology program and High Speed Systems Test (HSST) for funding this work under contract number FA9101-15-D-0002. I would also like to thank my advisors Drs. Feng-Yuan Zhang and Christopher Combs for their guidance and my supervisor and primary advisor Dr. Trevor Moeller for both bringing me on this project and guiding me through it. I'd also like to thank my coworkers Robert Rhodes and Katrina Sweetland and our contacts from NAS out at AEDC, Dr. David Plemmons and Roy Schultz, who worked closely with me throughout this project. Finally, I'd like to thank my colleagues Kenneth "Adam" Croft and Andrew Bell for their assistance and advice in setting up these simulations.

Abstract

Database parameters for line spectra are collected from many studies and require independent verification for use in the design and measurements of laser absorption spectroscopy systems. While many lower temperature lines are well characterized, the higher temperature and pressure lines found in studies of combustion products rely on theoretical scaling. High-temperature calibration devices are therefore desired to allow experimental validation of parameters under test conditions. For this research, the design of a high-temperature, three-zone gas cell is proposed as a replacement for the current absorption cell system at The University of Tennessee Space Institute (UTSI). This new design, a prototype of which has been built and tested at The Technical University of Denmark, allows for measurements of test gas samples at uniform temperatures of at least 1300K. A computational fluid dynamics (CFD) model is shown for the current UTSI gas cell that has <6% difference with measured flange temperatures and <7% difference from axial gas temperature measurements. This CFD model is then used to predict material and centerline gas temperatures expected at the limit of the proposed design. The model results show that the proposed cell design has a high temperature uniformity in the test section and flange temperatures well below the temperature limits of the desired O-ring materials and indicate that water-cooling will be unnecessary.

Table of Contents

List of Tables

List of Figures

Nomenclature

α	thermal diffusivity $\left[\frac{m^2}{s}\right]$
β	thermal expansion coefficient $\left[\frac{1}{K}\right]$
Δ	pressure-induced line shift
$\dot{Q}$	heat transfer per unit time $\left[\frac{J}{s}\right]$
$\dot{q}$	heat transfer per unit time per area $\left[\frac{J}{m^2 s}\right]$
ϵ_b	emissivity of the thermocouple bead
η	polynomial function of F_D and F_L
Γ	pressure-broadened half-width at half-maximum (HWHM)
Γ_D	Doppler half-width at half-maximum (HWHM)
λ	wavelength [m]
ν	frequency [Hz]
ν_0	frequency of laser [Hz]
ν_c	line-center frequency of the transition [Hz]
ϕ_ν	lineshape profile i.e. normalized Voigt Profile
σ	Stefan-Boltzmann constant, 5.67x 10^{-8} $\left[\frac{W}{m^2 K^4}\right]$
ε_h^d	Discretization error of simulated result

$\widetilde{\nu}$ wavenumber [cm^{-1}]

a order of the scheme used to find discretization error

A_b surface area of thermocouple bead [m^2]

A_i area of natural log of transmittance for transition i

$a_n(T)$ slope and y-intercept of the Boltzmann plot for Multiple Isolated Lines

A_w cross-sectional area of thermocouple wires [m^2]

$A_{\perp s}$ cross-sectional area of thermocouple Inconel-600 sheath [m^2]

c speed of light in vacuum, 299,792,458 $\left[\frac{m}{s}\right]$

D diameter [m]

$E_i^{''}$ ground state energy of transition i [eV]

F_D Doppler Profile (Gaussian)

F_L Collisional Profile (Lorentzian)

g acceleration due to gravity, 9.81 $\left[\frac{m}{s^2}\right]$

h Planck's Constant, 6.62607004 10^{-34} $\left[\frac{m^2 kg}{s}\right]$

h convection heat transfer coefficient $\left[\frac{W}{m^2 K}\right]$

I_0 incident intensity of laser $\left[\frac{W}{m^2}\right]$

I_t transmitted Intensity $\left[\frac{W}{m^2}\right]$

k Boltzmann constant, 1.38064852 x 10^{-23} $\left[\frac{m^2 kg}{s^2 K}\right]$

K_s thermal conductivity of the sheath $\left[\frac{W}{mK}\right]$

K_w thermal conductivity of the wire $\left[\frac{W}{mK}\right]$

k_ν spectral absorption coefficient

L beam path length [m]

M molar mass $\left[\frac{kg}{mol}\right]$

m molecular mass $\left[\frac{kg}{molecule}\right]$

P gas pressure [Pa]

$Q(T)$ total internal partition sum at temperature T for species of interest

Ra_D Rayleigh Number based on diameter

$S_0(T_0)$ reference linestrength $\left[\frac{cm^{-1}}{molecule \cdot cm^{-2}}\right]$

$S_i(T)$ linestrength scaled to temperature T $\left[\frac{cm^{-1}}{molecule \cdot cm^{-2}}\right]$

T temperature of medium [K]

T_b thermocouple bead temperature [K]

T_g gas temperature [K]

T_n normalized temperature

T_w furnace wall temperature [K]

T_∞ freestream temperature in furnace simulations, 300 [K]

$T_{\max}$ Temperature at the surface of the flange [K]

x_{abs} mole fraction of absorbing species

Chapter 1

Introduction

Engine environments, such as rocket and scramjets, contain harsh flowfields that make conventional in-stream diagnostics difficult due to the high speed, high enthalpy, combusting environment. Optical diagnostics like laser absorption spectroscopy (LAS) offer an advantage over their mechanical counterparts due to the non-intrusive nature of the measurement [1]. With the recent development of quantum-cascade lasers capable of probing the mid infrared, spectroscopic studies in this region have become of interest for analyzing the gas species present in combustion processes [2, 3]. H_2O, CO_2, CO, and NO in particular are being utilized for measurements of combustion processes [4, 5] and efficiency [1, 2, 3, 6]. Laser absorption spectroscopy is a diagnostic technique that takes advantage of the unique absorption of each species, in this case in the infrared, to determine macroscopic properties such as the temperature, pressure, and concentration of a gas [6, 7, 8, 9]. These quantities can then be coupled with knowledge of the combustion process for the engine to determine efficiency [6, 9]. Infrared lasers used in these systems have been shown to be stable for thousands of test hours with extremely high signal-to-noise ratios upwards of 100:1 for some electromagnetic regions, so laser absorption systems (LAS) are often desired for the long-term analysis of systems with high temperatures (<600K) or other factors that make the usual diagnostic methods difficult [1, 10]. One of the limiting factors in both the design and implementation of these devices is the dependency on simulated spectra to both choose a laser and extract macroscopic values. Simulations pull parameters for a given species based on many sources and rely on theoretical scaling for regions or conditions where data is insufficient or unavailable [4, 5, 11]. This

presents a problem for scientists hoping to produce a system to measure high-temperature or high-pressure gases or test novel wavelength regions; parameters in the database may contain incorrect values, be an incomplete set, or fail to include certain values that fall below cutoff conditions. For these reasons, it is desired to have a source to verify database parameters for the region and conditions of interest [6, 7, 11]. The ideal source would have at least the temperature range of the gas being measured at the pressures desired and high temperature uniformity [12, 13]. One such device often employed is a single-zone absorption gas cell that contains the test gas sample in a tube, often made of quartz [6, 8, 14, 15], inside a furnace with optical ports for the laser. The primary issues with this design are that the materials limit the maximum temperature of the cell and temperature uniformity is often poor, requiring measures such as a heated gas line to compensate for a lack of heating uniformity [14]. An evolution of the typical design is the so-called three-zone absorption cell, which alleviates the temperature uniformity issue by filling non-uniform regions with a non-reacting gas, in this case Nitrogen (N_2), which does not absorb like the test gas sample [3, 12, 14]. The purpose of this research was to propose a three-zone cell design based on a version built at The Technical University of Denmark [12] as a replacement for the current UTSI hot gas cell and to build a computational model to validate, verify, and optimize the design for the highest temperatures possible with the new furnace.

Chapter 2

Background and Theory

2.1 Absorption Spectroscopy

Spectroscopy is the study of the interactions between matter and the electromagnetic spectrum. Absorption spectroscopy is the technique of measuring the absorption of electromagnetic radiation by matter as a function of the frequency of the incident electromagnetic waves. When radiation passes through matter, the amount that transmits is determined by interactions dependent on the properties of the medium and the frequency of the incoming radiation. Such interactions can include changes to electronic state of an atom or molecule inside the medium and other quantum mechanical changes, like induced vibrational and rotational states [3]. The latter two can occur simultaneously and are the interactions relevant to this research. The typical frequencies ν at which so-called rovibrational modes occur are between 10^{12} and 10^{14} Hz, but these are often referenced by wavenumbers $\widetilde{\nu}$, which are obtained from the formula

$$\widetilde{\nu} = \frac{\nu}{c} \tag{2.1}$$

given in cm^{-1}, where c is the speed of light. Much study has recently been done for rovibrational state transitions in the mid IR (2.5-25 μm or 400-4000 cm^{-1} [16]), typically of atmospheric gases, due to the advances in the availability of quantum cascade lasers (QCLs) capable of probing wavenumbers down to 400 cm^{-1} in the past two decades [7, 13, 15, 17].

These wavenumber-dependent transitions are characterized by the wavenumber at which a local peak in the absorption of radiation through the medium occurs. The interaction occurs when the electromagnetic radiation is incident upon a molecule and interacts with the dipole moment to produce a change in energy of the molecule from some lower state with an energy E_1 to an upper state with energy E_2. This wavenumber then corresponds to the energy of the photon absorbed that matches the energy difference of two electronic energy levels, and is related to the moment of inertia, intermolecular distance, spring constant, and bond angle of the molecule [16]. For a more complete mathematical formulation of these interactions, the reader should seek references such as [18].

A plot of optical depth, which is a measure of how much the initial signal is attenuated by the material, versus wavenumber, called an absorption spectrum, is comprised of the sum of many so-called "lines", each an individual transition to a different state caused by the absorption of incoming radiation by an atom or molecule in the medium. These spectra are unique to a given species [3], and the lines comprising them are typically referenced by the wavenumber $\widetilde{\nu}_c$ at the center of the peak. This wavenumber is determined by the structure of the atom or molecule and represents a transference of radiative energy into a particular quantum state. While this transition occurs when a specific wavenumber $\widetilde{\nu}_c$ of energy is absorbed, the probabilistic nature of quantum mechanics and natural movements of the molecules causes the immediate surrounding wavenumber range to contain a lower chance of the transition occurring, which approaches zero at a distance dependent on the shape of the line. This leads to the characteristic shape of a line, which is typically approximated by a Voigt Profile [19].

A Voigt Profile is a spectral lineshape, which can be considered a probability distribution if normalized, created from the convolution of independent Gaussian and Lorentz probability distribution functions [1, 20]. This Voigt Profile is the current standard for high resolution spectroscopic studies as it fits the shape of the lines well and with less computationally expensive algorithms than more accurate modelling techniques [20]. Additionally, the constants present in the Lorentzian and Gaussian functions can be related to macroscopic variables of the medium [1]. While each line is primarily dependent on the frequency of radiation and the molecules or atoms forming the medium, the shape, center, and magnitude

of the profile can be altered by macroscopic properties such as pressure, concentration, temperature, path length, and mean velocity. The three primary physical factors associated with line shape changes are the Heisenberg time-energy uncertainty principle, the Doppler Effect, and collisional effects [20]. The Heisenberg time-energy uncertainty effects and the resulting Lorentzian Profile, which represents the natural width of the line, can usually be neglected outside of ultra-low temperature cases. The Doppler Effect, which is due to the thermal translational motion of the spectroscopically active molecule at velocity v_a, gives the incoming radiation, of frequency ν_0, a frequency shift of $\Delta\nu = \pm(v_a/c)\nu_0$ in the molecular frame of reference. The resulting Doppler Profile F_D can be expressed in terms of the unitless Doppler half-width [19, 20], Γ_D, by the Gaussian function in Equation 2.2 given the Doppler half-width definition shown in Equation 2.3.

$$F_D(\nu - \nu_0) = \sqrt{(\frac{\ln(2)}{\pi}}\frac{1}{\Gamma_D}\exp\Big[-\ln(2)\Big(\frac{\nu-\nu_0}{\Gamma_D}\Big)^2\Big] \tag{2.2}$$

For a given temperature T, in K, and molecular mass m, in kg, the Doppler half-width becomes

$$\Gamma_D = \sqrt{\frac{2\ln(2)kT}{mc^2}}\nu_0 \tag{2.3}$$

In terms of molar mass M in $\frac{kg}{mol}$, the Doppler half-width becomes

$$\Gamma_D = 3.581163 \times 10^{-7}\nu_0\sqrt{\frac{T}{M}} \tag{2.4}$$

This means that the Doppler half-width is dependent on temperature, the absorbing species of the medium, and frequency of the incoming radiation, which in the case of zero macroscopic velocity is also the line-center wavenumber of the transition. Collisional effects are due to the individual collisions of molecules, which leads to energy exchanges [1, 19, 20]. These collisions can induce shifts in the central frequency, ν_c, of the line and an overall broadening of the line profile. If one assumes that the effects of pressure broadening and pressure-induced line shifts are independent, one obtains the homogeneous Lorentzian profile in Equation 2.5 with the pressure-broadened line half-width at half-max, Γ, and the pressure-induced line shift, Δ [20].

$$F_L(\nu - \nu_0) = \frac{1}{\pi} \frac{\Gamma}{(\nu - \nu_0 - \Delta)^2 + \Gamma^2} \tag{2.5}$$

The Voigt Profile calculation requires solving an integral that cannot be solved analytically, but several fast computational procedures exist to bypass this [21, 22]. Some spectroscopic codes avoid the integral entirely by using a so-called normalized pseudo-Voigt profile $V_p(\nu)$, of the form defined in Equation 2.6, which treats the profile as a linear combination of the Lorentzian and Gaussian profiles instead, with a chosen polynomial function η dependent on both the Lorentzian and Gaussian profiles.

$$V_P(\nu) = \eta \cdot F_L + (1 - \eta) \cdot F_D \quad \text{with} \quad 0 < \eta < 1 \tag{2.6}$$

It should also be noted that while the Voigt profile is by far the most common fit used for spectral line shapes, its use can lead to widespread errors, such as systematic underestimation of line intensities, for example, as was found for measurements of water vapor in both the laboratory and the atmosphere [11]. While other line shapes have been proposed, such as the Hartmann-Tran Profile, the Voigt Profile is still the current standard for which line parameter databases such as HITEMP and HITRAN are tabulated [20].

2.2 Laser Absorption Spectroscopy

One of the most common uses of absorption spectroscopy is in trace gas analysis, with the goal of determining the temperature, concentration, or identity of a gas [1, 6, 9, 7]. A laser with a tunable, monochromatic frequency, typically by altering current or temperature of the laser, is fired through a gas and onto a detector [6, 10, 23]. The ratio of the transmitted intensity to the incident intensity is recorded along with the frequency of the laser. This ratio, $\frac{I_t}{I_0}$, called the transmittance, is related to the spectral absorbance in frequency, $k_\nu L$, where k_ν is the spectral absorbance coefficient and L is the beam path length. This leads to the Beer-Lambert Law, shown by Equation 2.7, which relates the attenuation of the laser to the macroscopic properties of the material through which the beam is traveling [1, 8].

$$\left(\frac{I_t}{I_0}\right)_\nu = \exp(-k_\nu L) = \exp(-P x_{\text{abs}} S_{\text{i}}(T) \phi_\nu L) \tag{2.7}$$

The Beer-Lambert Law relates gas pressure P, transition linestrength $S_i(T)$, mole fraction of absorbing species x_{abs}, and lineshape function ϕ_ν. The linestrength $S_i(T)$ at an arbitrary temperature T for an isolated transition can be found by scaling the reference line strength $S_0(T_0)$ by Equation 2.8, where E'' is the energy of the lower state, h is Plancks constant, c is the speed of light, k is the Boltzmann constant, and ν_c is the line-center frequency of the transition [1, 6, 8]. The total internal molecular partition function $Q(T)$ gives information on how the probabilities of certain quantum states are partitioned based on their individual energies, and is used to determine how molecules in thermodynamic equilibrium are distributed among the various energy states at a particular temperature. The calculation of these functions involves the summation over lower energy levels, potentially thousands, for the species of interest at each temperature [24], and are referenced from databases such as HITRAN [5] and HITEMP [4].

$$S_i(T) = S_0(T_0)\frac{Q(T_0)}{Q(T)}\left(\frac{T_0}{T}\right)\exp\left[-\frac{hcE''}{k}\left(\frac{1}{T}-\frac{1}{T_0}\right)\right]\times\frac{\left[1-\exp\left(\frac{-hc\nu_c}{kT}\right)\right]}{\left[1-\exp\left(\frac{-hc\nu_c}{kT_0}\right)\right]} \tag{2.8}$$

Methods of measuring strong lines in the mid IR most often use direct absorption wavelength scans. Weaker lines can be measured using other methods, such as Wavelength Modulation Spectroscopy (WMS) [7], but this is often not necessary with the temperatures, pressures, and concentrations seen in combustion environments [9]. If one is probing rovibratonal transitions that occur in this wavenumber range, two of the most common techniques of measuring values from the gas are two-line thermometry and Boltzmann plots, where Boltzmann plots are an extension of the theory of two-line thermometry to additional lines [1]. In practice, applications of these transitions are focused on obtaining the path-averaged temperature and concentration of the absorbing species. For this technique, the lines are required to be isolated from interference due to other lines. Methods for using

spectroscopic absorption to determine temperature and concentration begin with the Beer-Lambert Law (Eq. 2.7). Since transmittance is a function of ν (or $\widetilde{\nu}$), the normalized line-shape function ϕ_ν can be integrated out by defining an area A_i as shown in Equation 2.9 [6, 1, 9, 8].

$$A_i = \int_{-\infty}^{\infty} -\ln\left(\frac{I_t}{I_0}\right) d\nu = P x_{\text{abs}} S_i(T) L \tag{2.9}$$

For two-line thermometry, the integrated absorbance of two transitions are measured simultaneously with the same pressure, mole fraction, and path length. If the two lines are very close in wavenumber, the ratio of the two areas then simplifies to Equation 2.10.

$$\frac{A_1}{A_2} = \frac{S_1(T)}{S_2(T)} = \frac{S_{01}(T_0)}{S_{02}(T_0)} \exp\left[-\frac{hc}{k}(E_1'' - E_2'')\left(\frac{1}{T} - \frac{1}{T_0}\right)\right] \tag{2.10}$$

This equation can be solved for T to obtain Equation 2.11 [6, 1].

$$T = \frac{\left(\frac{hc}{k}\right)(E_2'' - E_1'')}{\ln\left(\frac{A_1}{A_2}\right) + \ln\left(\frac{S_{02}(T_0)}{S_{01}(T_0)}\right) + \left(\frac{hc}{k}\right)\left(\frac{E_2'' - E_1''}{T_0}\right)} \tag{2.11}$$

In addition to the proximity requirement of the two transitions, the temperature scales with the difference in lower-state energies between the two states. This factor determines the sensitivity of the temperature measurement [7]. Because of the implicit uniform gas assumption along the line of sight, two-line thermometry is not recommended for regions containing temperature or pressure gradients [6]. For cases where multiple lines are being used to derive temperature, the Boltzmann Plot for Multiple Isolated Absorption Lines (Boltzmann) method may be used. This method substitutes Equation 2.9 into Equation 2.8. One then obtains Equation 2.12 [1].

$$\ln\left(\frac{A_i}{S_0(T_0)}\right) = \ln\left(P x_{\text{abs}} L \frac{Q(T_0)}{Q(T)}\right) - \left[\frac{hc}{k}\left(\frac{1}{T} - \frac{1}{T_0}\right)\right] E_i'' + \ln\left[\frac{1 - \exp\left(\frac{-hc\nu_c}{kT}\right)}{1 - \exp\left(\frac{-hc\nu_c}{kT_0}\right)}\right] \tag{2.12}$$

Equation 2.12 can be simplified to the form shown in Equation 2.13, which forms the basis of the Boltzmann method. The left side of the equation is then taken as the y-axis and

the ground state energy of the transition as the x-axis. By using several lines of the same species, which each gives a single data point, and an iterative process, the slope may be used to obtain the temperature of the sample.

$$\ln\left(\frac{A_i}{S_0(T_0)}\right) = a_0(T) + a_1(T)\cdot E_i'' \tag{2.13}$$

Both of these methods only provide a path-averaged temperature and concentration value. In the case where information about a temperature distribution is required or where large temperature gradients exist, given enough strong transitions to probe for a single species, a broad scanning laser such as a Vertical Cavity Surface-Emitting Laser (VESCL), which can provide rapid single-mode scans over a wavelength range (30 cm^{-1}), can be used with Equation 2.9 to create a linear system of the form shown in Equation 2.14 or Equation 2.15 with m number of transitions and n number of temperature bins [8]. With some knowledge of the minimum and maximum temperatures and overall temperature distribution, the linear system can be solved to obtain distinct measurements of each gradient.

$$\begin{bmatrix} S_1(T_1) & S_1(T_2) & \dots & S_1(T_n) \\ S_2(T_1) & S_2(T_2) & \dots & S_2(T_n) \\ \vdots & \vdots & \ddots & \vdots \\ S_m(T_1) & S_m(T_2) & \dots & S_m(T_n) \end{bmatrix} \begin{bmatrix} (PxL)_1 \\ (PxL)_2 \\ \vdots \\ (PxL)_3 \end{bmatrix} = \begin{bmatrix} A_1 \\ A_2 \\ \vdots \\ A_3 \end{bmatrix} \tag{2.14}$$

or

$$\mathbf{Sx} = \mathbf{a} \tag{2.15}$$

This method is strongly dependent on the temperature discretization, or bin choice, and primarily suited to cases where large, sudden temperature changes occur, such as those present in boundary layers. The primary drawback is that spatial knowledge of the temperature fields is not possible to obtain without multiple line-of-sight measurements [8]. In all absorption spectroscopy methods of extracting macroscopic properties of the flow, knowledge of the parameters of a transition must be known to a high degree of accuracy to reduce the errors in measured macroscopic quantities.

2.3 Line Validation

Several databases of common gases, primarily atmospheric, have been created for use in spectroscopy. Perhaps the most widely-used database is the High-Resolution Transmission Molecular Absorption (HITRAN) Database, which contains ∼7 million spectral lines for 47 different molecules [5]. HITRAN was originally created for atmospheric studies, and contains information relevant to those conditions. This leads to deficiencies for lines that are insignificant under atmospheric conditions but relevant at higher pressures or temperatures. Lines in regions not relevant to or accessible for atmospheric studies were also sparsely included. In particular, HITRAN was found to be lacking in the near-IR and visible spectral regions, for high temperature applications, and for absorbers like H_2O and CO. This led to the creation of the high-temperature molecular spectroscopic (HITEMP) database [4]. HITEMP is structured in the same manner as HITRAN but contains only the absorbers H_2O, CO_2, CO, NO, and OH. For applications involving additional molecules, a combination of the HITEMP and HITRAN databases is used for simulating spectra.

The spectral lines chosen for trace gas analysis are dependent on the gas composition, velocity, concentrations, path length, pressure, and temperatures anticipated in the sample. Spectral simulations based on these conditions allow line candidates to be chosen while considering interference sources, laser availability, optical equipment capability, and any anticipated gradients such as those present in boundary layers. In virtually all situations, construction of a spectroscopic system requires validation of the parameters predicted in the simulations in a controlled setting [6, 7]. For example, small errors in the linestrength can cause scaling errors through Equation 2.8, errors in the collisional and Doppler widths (Eqs. 2.3 and 2.2) can hide interference from nearby lines, and lines not included in a database may become detectable at elevated temperatures. Calibration is another primary requirement necessitating a controlled environment for testing.

For low temperature lines (<1000K), verification of lines using an electrically-heated furnace [6, 10, 12] is a common approach. Furnaces can provide a stable environment over long periods of time with the option of extending the beam path length through the use of mirrors. However, furnaces often suffer from non-uniform temperature distributions or low

maximum temperatures. In past studies, test gas cells were composed of a primarily metal body, with the high conduction helping to create a more uniform temperature distribution. This limits the maximum temperature of the furnace to the melting point of the metal body. In order to adequately model the gas conditions involved in most engine combustion processes, temperatures above 2400K at high pressures are desired [12], which is well above the melting temperature for most high-temperature metal alloys. For this reason, some high-temperature gas cells use a primarily quartz body [6, 8, 14], which has a maximum operating temperature of approximately 1500K [25], and any metal components or optical components are removed from the hottest regions. While this allows metals and more optically desirable windows to be used in the construction of the cell, it necessitates large temperature gradients along the laser absorption beam path.

Chapter 3

High-Temperature Absorption Cell

3.1 UTSI System

The University of Tennessee Space Institute (UTSI) uses an absorption cell made of quartz, which is simply a quartz tube with flanges on the ends for optical ports, for laser absorption studies in the mid-infrared. It is common to pair cells of this design with a tube furnace [6, 12], which is comprised of a cylindrical furnace with the radial center bored through. Surrounding the bore are 1, 2, or 3 electrical heating coils with temperature control monitored by the same number of thermocouples, depending on the furnace configuration. The UTSI system uses a Carbolite® 3-zone tube furnace with a maximum operating temperature of 1473K to heat the quartz cell. The quartz tube has an outer diameter of 1.4" and 1/8" walls and extends 4.15" out of each end of the furnace with stainless steel flanges (3" outer diameter) supported by posts, which extends the total length to 29". Each flange contains a beveled sapphire (Al_2O_3) window and equally beveled Teflon ring. The bevels are 1.5° and each is 5 mm thick at the center with a height of 1". These two single-sided bevels are seated together with bevels opposite to create a disk with parallel faces. The inlet/outlet for each flange is a stainless steel tube on top. The system in place at UTSI is shown in Figure 3.1, and a schematic of the flange, quartz tube, sapphire window, and Teflon ring used at UTSI is shown in Figure 3.2.

The centerline temperature profile of this cell was recorded under static conditions by swapping one sapphire window and Teflon pair for a stainless steel port, allowing the

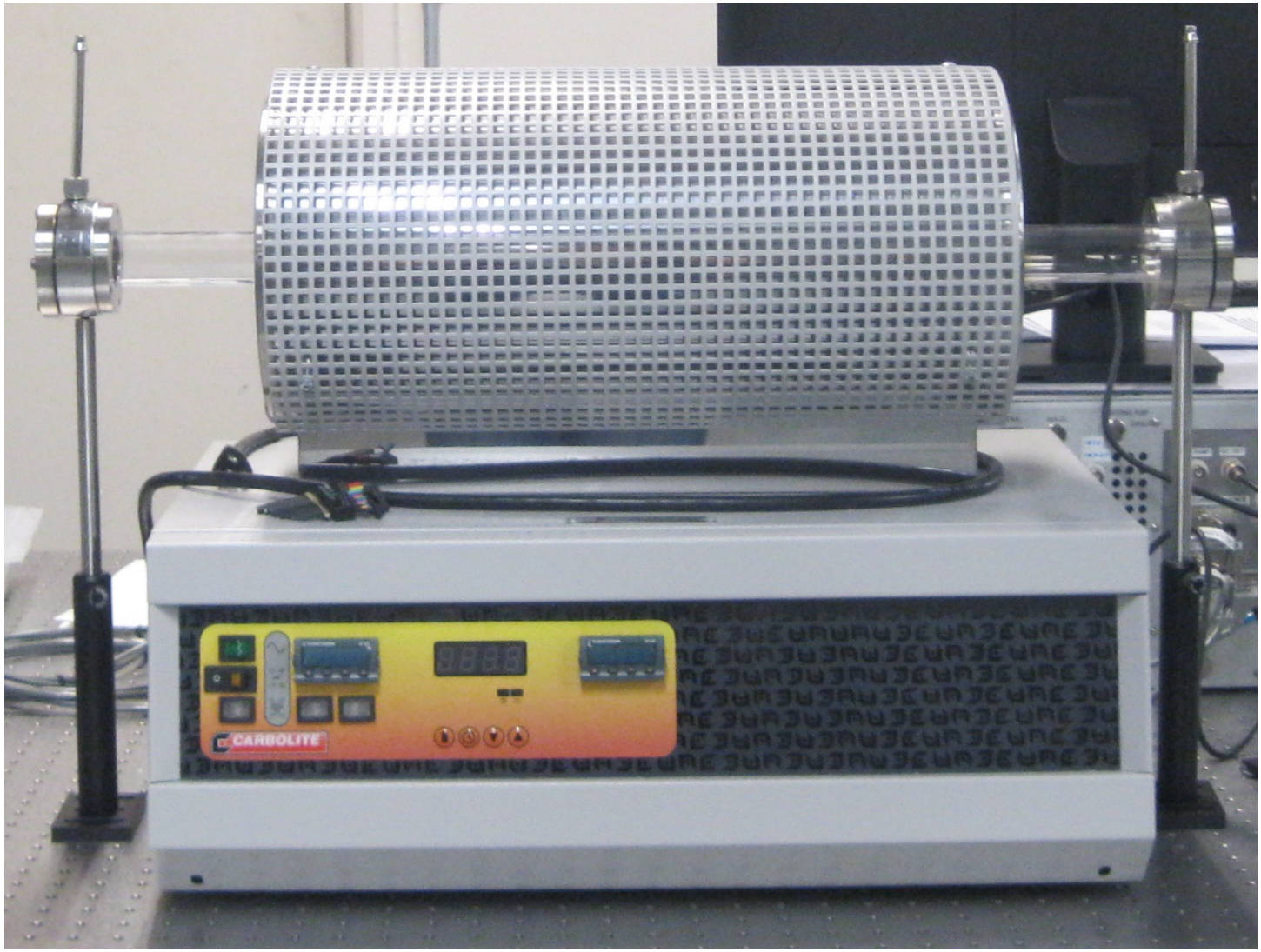

Figure 3.1: Quartz Absorption Gas Cell and Carbolite 3-Zone Tube Furnace with stainless steel flanges located at UTSI. The quartz cell sits inside the tube furnace with the steel flanges supported by posts.

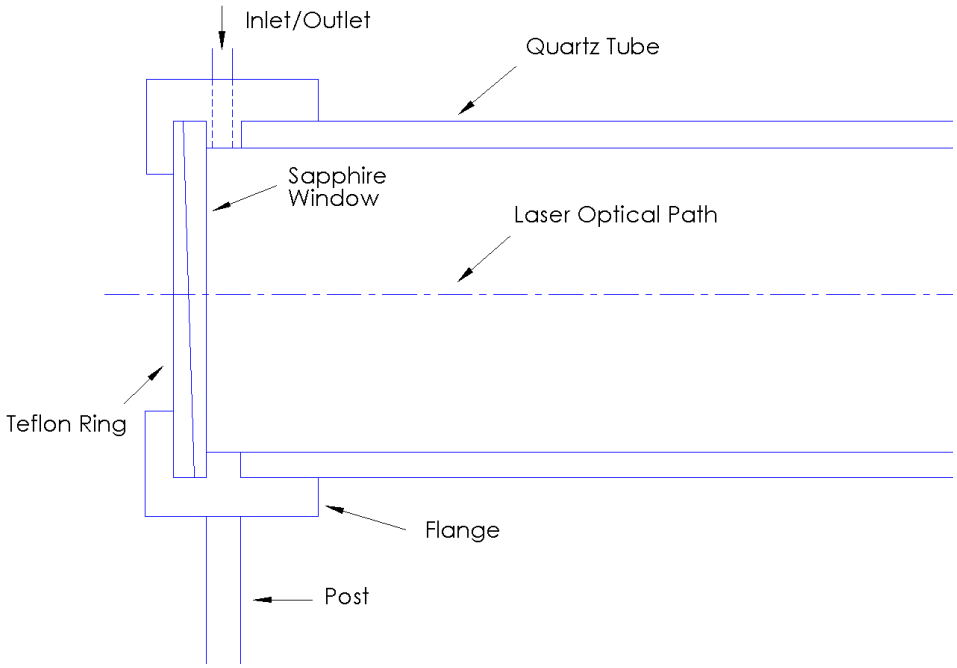

Figure 3.2: Schematic of the UTSI quartz tube and flange. The separations between the three pieces of the flange are not shown. The beveled Teflon ring and sapphire window fit together to create a disk. Image taken from SolidWorks ®.

insertion of a National Institute of Standards and Technology (NIST) certified K-type thermocouple purchased from Omega® through an alumina sheath that leaves 1/4" containing the grounded junction end exposed. This thermocouple was used to measure temperatures over half the cell length, up to the center symmetry plane, at two inch intervals with lower spacing for regions with high gradients. The furnace was set to 1173K (900°C) and left for 30 minutes after the temperature monitor reached the set temperature, at which point it was assumed to be steady state and the temperature measurements were taken. The profile was taken at intervals of 1 or 2 inches, with 1 inch intervals for the regions of high gradients. Each measured point was given at minimum four times the measured time constant of the thermocouple and sheath combination before each measurement was recorded. The furnace and cell combination is physically symmetric about the center of the tube furnace and the measurements taken from either end by switching the thermocouple insertions side were assumed to be independent measurements of the same half-profile. Each total profile was obtained by mirroring the measured values from half to reduce the conduction errors associated with measuring the entire profile from one side. Figure 3.3 shows one such

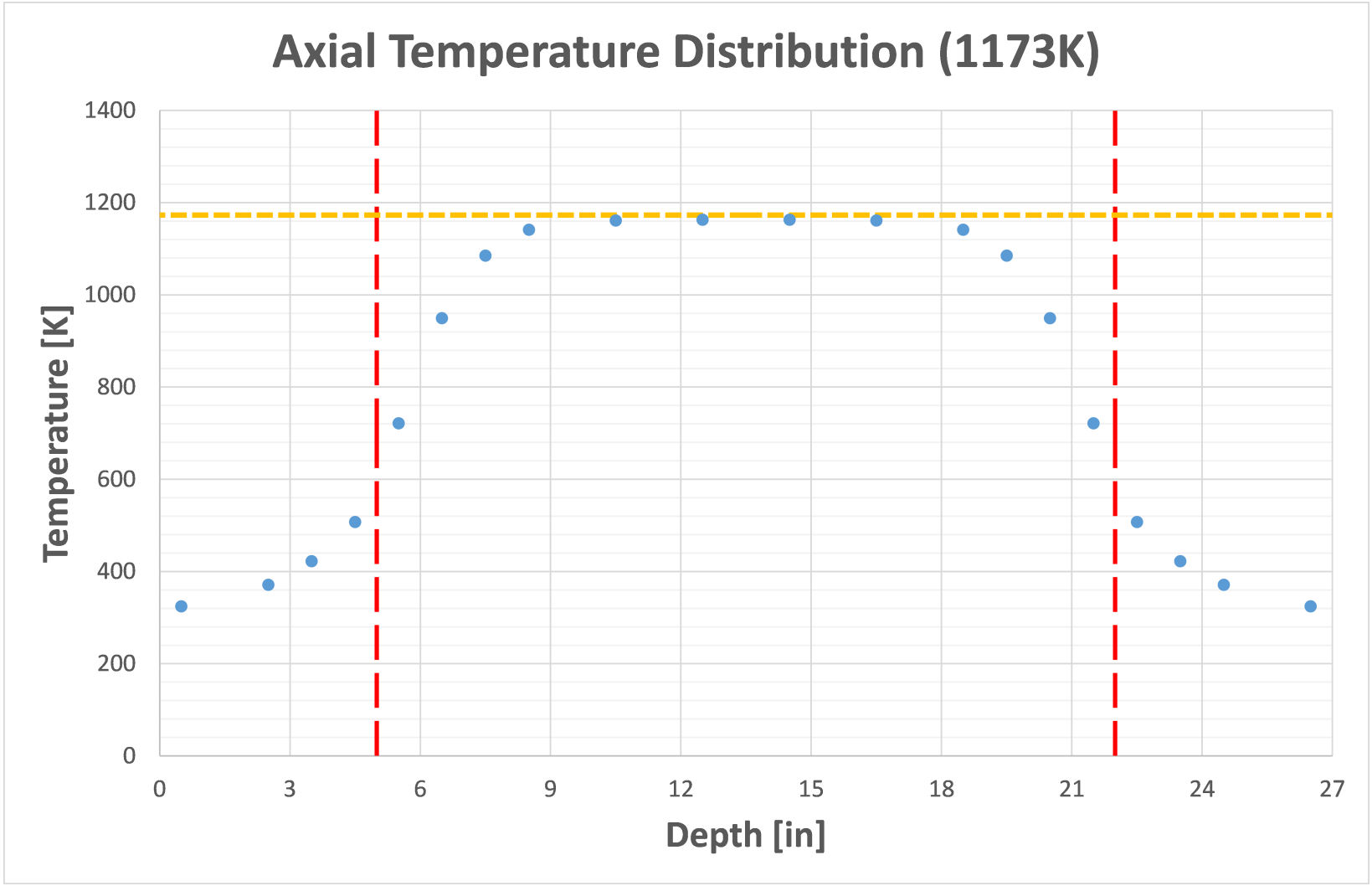

Figure 3.3: Axial temperature distribution in quartz gas cell at UTSI with the furnace set to 1173K. The red lines indicate the width of the furnace and the yellow indicates the set temperature of 1173K.

measured profile, where the red dashed lines indicate the width of the furnace and the yellow is the set temperature. The profile shows high uniformity in the center section of the furnace with a difference of 13 K from the set temperature. In order to compare the simulations of the UTSI cell, which are discussed later, to measured thermocouple values, a model for the conductive, radiative, and convective losses in the thermocouple measurement is required to provide an estimate for the true gas temperature.

3.1.1 Thermocouple Corrections

The K-type thermocouple used to measure the temperature in the UTSI furnace is a 36" long, 1/8" diameter, Inconel-600 clad, grounded thermocouple slid through an alumina sheath to reduce conduction effects and prevent the thermcouple from sagging during measurements. An analytical practice often seen is to set up an energy balance for the bead, which in this case is assumed to be the rounded end of the thermocouple due to the grounded configuration, where $\dot{Q}$ is the heat transfer per unit time and the thermocouple bead is assumed to be in steady-state [26, 27].

$$\sum \dot{Q} = \dot{Q}_{\text{cond}} + \dot{Q}_{\text{conv}} + \dot{Q}_{\text{rad}} = 0 \tag{3.1}$$

with the assumption of axial conduction only, the equation becomes

$$\sigma \epsilon_b A_b (T_w^4 - T_b^4) + h A_b (T_g - T_b) - (K_w A_w + K_s A_{\perp s}) \frac{dT}{dx}\Big|_b = 0 \tag{3.2}$$

where σ is the Stefan-Boltzmann constant, ϵ is the emissivity of the thermocouple bead, A_b is the surface area of the bead, T_w is the furnace wall temperature, T_b is the measured bead temperature, h is the convective heat transfer coefficient, T_g is the temperature of the gas, K_w is the thermal conductivity of the thermocouple wire, A_w is the area of the wire, K_s is the thermal conductivity of the Inconel-600 sheath, $A_{\perp s}$ is the cross-sectional area of the Inconel-600 sheath, and $\frac{dT}{dx}\big|_b$ is the change in temperature between the bead and the wire.

If one makes the assumption that the "bead" measures the temperature at the surface of the round end of the thermocouple, which is assumed to be perfectly hemispherical, only three unknown values remain; T_w, the temperature of the enclosure, h, the convective heat

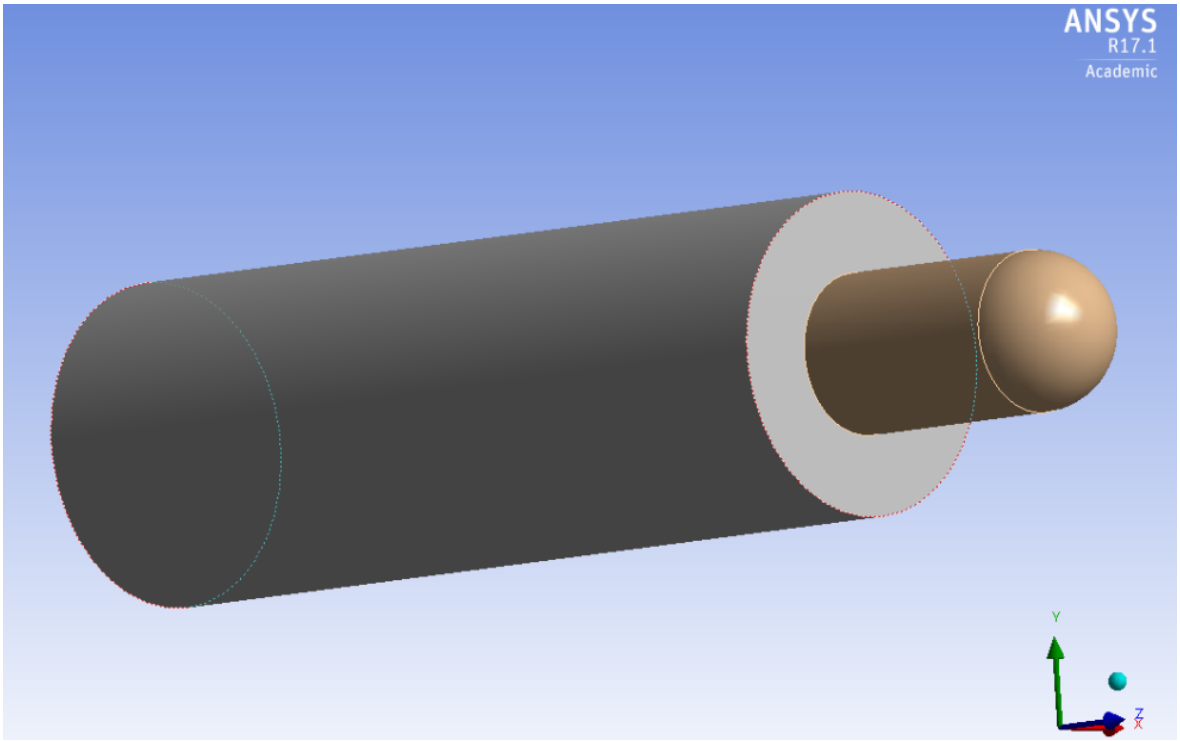

Figure 3.4: Geometry of the one-inch model of the thermocouple/alumina sheath combination. The thermocouple is modelled as a solid Inconel-600 piece and protrudes from the alumina sheath 1/4". Image used courtesy of ANSYS®, Inc.

transfer coefficient between the bead and the gas, and $\frac{dT}{dx}\big|_b$, the temperature change between the bead and the wires in the thermocouple.

To obtain an estimate for these values, a simulation was run using ANSYS® Academic Research Fluent, Release 17.1. First, a point was chosen in the gradient region of furnace profile, as these locations will contain the highest conduction error. The point at 8.5" was chosen to allow the assumption that the wall temperature T_w is the set temperature of the furnace (1173K). A one-inch model of the end of the thermocouple/alumina sheath combination was made in SolidWorks® and meshed in ANSYS® Academic Research Mesh Release 17.1, and the geometry of the model is shown in Figure 3.4 and the mesh for the middle case is shown by Figure B.1 in Appendix B. A one-inch model was chosen to allow the assumption that the piece has reached steady state and that the end opposite the bead, which is one end of the domain, can be maintained at the temperature measured for the point at 7.5" in Figure 3.3. The full set of boundary conditions (Figure 3.5) was then; uniform temperature of the furnace on the radial face of the cylindrical fluid (air) domain, which is

the size of the inner diameter of the quartz tube, the measured temperature of the adjacent point (1085K) on the boundaries for the thermocouple and sheath opposite the bead, and pressure outlets with a back flow temperature of 1173K on the gas. The Discrete Ordinates (DO) radiation model was chosen because of the optical thickness, which is discussed in more depth in Section 3.3, and the furnace was treated as a black body emitter.

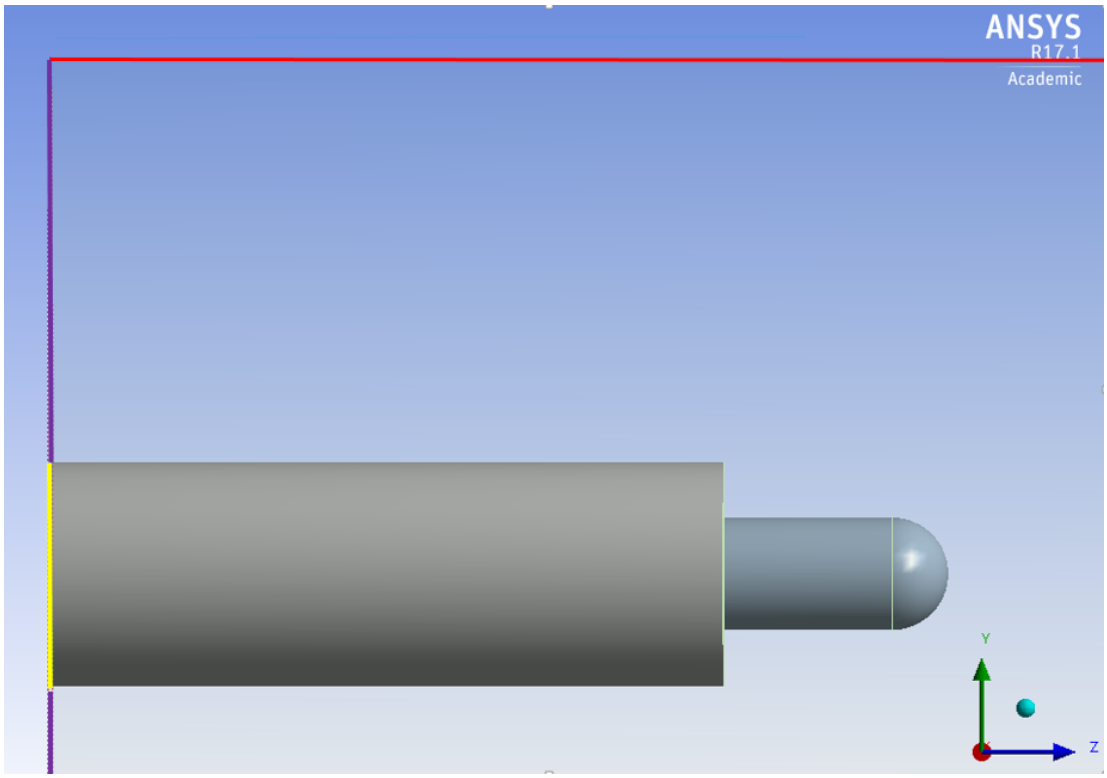

Figure 3.5: Thermocouple/alumina sheath model and the cylindrical fluid domain enclosing it. The red boundary condition it the set temperature of the furnace, the yellow is the temperature measured at the adjacent (7.5") point, and the purple are the pressure outlets with backflow total temperature of 1173K. Image used courtesy of ANSYS®, Inc.

The simulation was set to laminar, steady-state using the Boussinesq model for air as recommended by the ANSYS help documentation [28]. The Boussinesq model treats density as a constant except for when calculating buoyancy term in the momentum equation, where it is treated as a function of temperature. This model is recommended by ANSYS for cases of natural convection where temperature gradients are small [28]. To determine convergence, the average air temperature was monitored (Figure C.2 in Appendix C). The choice of laminar flow solver, DO radiation model, and convergence criterion is discussed in more detail in Section 3.3. There are 4 values of interest needed to calculate h for use with the

analytical model; T_b, which was taken to be the average temperature of the hemispherical tip shown in Figure 3.4, the average gas temperature T_g, the area-averaged surface heat flux $\dot{q}_{\text{tot}} = \dot{q}_{\text{rad}} + \dot{q}_{\text{conv}}$, and the area-averaged radiative heat flux $\dot{q}_{\text{rad}}$. There is not a singular monitor for the convective heat flux, so the radiative heat flux is subtracted from the total. These four values can then be used to determine the convective heat transfer coefficient [29].

$$h = \frac{\dot{q}_{tot} - \dot{q}_{\text{rad}}}{T_g - T_s} \tag{3.3}$$

To that end, three meshes were created from the thermocouple model; a coarse, middle, and refined that differ by a factor of ≈2 in node count. The values of interest were recorded, and, upon reaching steady state as defined by the behavior of T_g, the final 200 time steps were averaged and recorded in Table 3.1. This gives a simulated result for h, but $\frac{dT}{dx}\big|_b$ is still unknown. This value comes from the conduction portion of Eq 3.2, and represents a portion of the 1-D approximation of heat transfer due to conductive effects. This value was obtained by importing the data from each simulation into ParaView® with the "plot over line" feature along the centerline of the thermocouple to obtain a temperature profile. The temperatures from the tip of the thermocouple and 0.0625" (the radius of the hemisphere) down axially from the tip were then taken such that $\frac{dT}{dx}\big|_b \approx \frac{\Delta T}{\Delta x}$. The values from each mesh were then analyzed to find the discretization error [29, 30] using Richardson Extrapolation, which takes the form of

$$\varepsilon_h^d \approx \frac{\phi_h - \phi_{2h}}{2^a - 1} \tag{3.4}$$

where ε^d is the discretization error, ϕ is the variable of interest with h signifying the finest mesh, and a is the order of the scheme and is given by the equation

$$a = \frac{\log\left(\frac{\phi_{2h} - \phi_{4h}}{\phi_h - \phi_{2h}}\right)}{\log(2)} \tag{3.5}$$

where the "2" signifies an approximate doubling of nodal density. The values for each of the variables of interest for each mesh, order of the scheme, discretization error, and corrected grid-independent values for can be found in Table 3.1.

The grid-independent results can then be input in Equation 3.3 to give a value of $h = 365.04\ \frac{W}{m^2 K}$, then in Equation 3.2, solved for T_g, to find the correction for thermocouple

Table 3.1: Values from the thermocouple simulations. These values are corrected using the Richardson Extrapolation by calculating the discretization error and adding it to the finest mesh result.

Simulation	T_g [K]	T_b [K]	$\dot{q}_{\text{tot}}$ $\left[\frac{J}{m^2 s}\right]$	$\dot{q}_{\text{rad}}$ $\left[\frac{J}{m^2 s}\right]$	$\frac{dT}{dx}\big\vert_b$ $\left[\frac{K}{m}\right]$
Coarse (32,116 nodes)	1167.4	1151.4	7289.5	878.72	2934.5
Middle (60,723 nodes)	1167.3	1147.3	9502.6	1200.3	2082.6
Refined (120,500 nodes)	1166.8	1145.6	9710.2	1247.7	1609.7
a (Combined)	-1.7407	1.2217	3.4142	2.7603	0.8492
ε_h^d (Combined)	0.7076	-1.2996	21.489	8.2170	-589.96
Corrected Values	1167.5	1144.3	9731.7	1255.9	1019.8

losses at the singular point located at 8.5" of 1141.15K in the furnace measurements, which gives the corrected temperature for the gas at that location.

$$\begin{aligned} T_g &= \frac{-\sigma\epsilon_b(T_w^4 - T_b^4)}{h} + T_b + \frac{(K_w A_w + K_s A_{\perp s})\frac{dT}{dx}\Big|_b}{hA_b} \\ &= \frac{(-5.67\times10^{-8})(0.53)(1173^4 - 1141.15^4)}{365.04} \cdots \\ &\ldots + 1144.3 + \frac{[(19)(\pi 0.0004^2) + (27.5)(\pi 0.0015875^2 - \pi 0.0004^2)](1019.8)}{(365.04)(2\pi 0.0015875^2)} \\ &= 1167.2\text{K} \end{aligned} \tag{3.6}$$

This could be taken as an estimate of the true gas temperature at that location, which seems like a reasonable value for that point, but the author prefers to leave it as an error term. There are two reasons for this; the hefty amount of assumptions required to reach a correction factor for this single point and that these calculated values will not hold true for any other measured point in the furnace. Therefore, this term (1162.6-1141.2 = 21.4K) is treated as a positive uncertainty for each measurement representing a estimated "maximum loss" value, since the temperature of the bead, given the method of measurement of waiting four time constants and the assumed steady state of the furnace, is not expected to be above the actual gas temperature. The full list of uncertainties considered for this measurement is shown in Table C.1 and the uncertainty values are shown in Table C.2 in Appendix C.

3.2 3-Zone Absorption Cell

In the ideal spectroscopic study, only the test gas contained in the uniformly-heated center section would be measured, but the location of the optical ports in the UTSI system requires the laser to traverse the entire length of the cell. The colder wings of the temperature profile contain the test gas at a lower temperature and add to the optical depth recorded from the transmittance measured by the detector. An example of the difference is shown in Figure 3.6. Spectra for 10% H_2O were generated from the HITRAN database for the "ideal" and "real" cases. The uniform section data includes only the uniformly-heated center section, which is the center 2/3 of this furnace, at 1173K. The total furnace spectrum was created by splitting the furnace axial temperature distribution into nine segments and adding the resulting optical depths. Each segment contains an error based on the temperature measurement and resolution of the segment. Therefore, in order to make a simulated spectrum to compare to experimental results, the entire temperature distribution must be known at high resolution and with modelling for radiative, conductive, and convective losses in the measurement device for each furnace temperature of interest. Additionally, if any discrepancies are found between the simulated and experimentally measured spectra, the segments must be decoupled to find those deficiencies in the database values or the presence of undocumented lines. Since each segment represents a slice of test gas at some temperature, decoupling the segments would require a method like the one shown in Eqs. 2.14 and 2.15. However, a simpler solution is to avoid these undesirable regions entirely.

The temperature gradient problem can be circumvented by creating a so-called three-zone gas cell. The basic premise of the three-zone gas cell is to keep the regions containing undesirable temperature gradients filled with a non-reacting gas which does not absorb electromagnetic radiation at the wavenumber of the laser. The uniform temperature region in the center of the furnace and cell would contain only the test gas. The structure of the cell depends on the size and configuration of the furnace. The cell, which is only accessible through either side of the bore in the furnace, must allow for all gas inlets and outlets, instrumentation ports, and optical ports for the laser. The method of creating the non-reacting zones chosen by Christiansen, et al. was to cantilever two inner tubes inside the

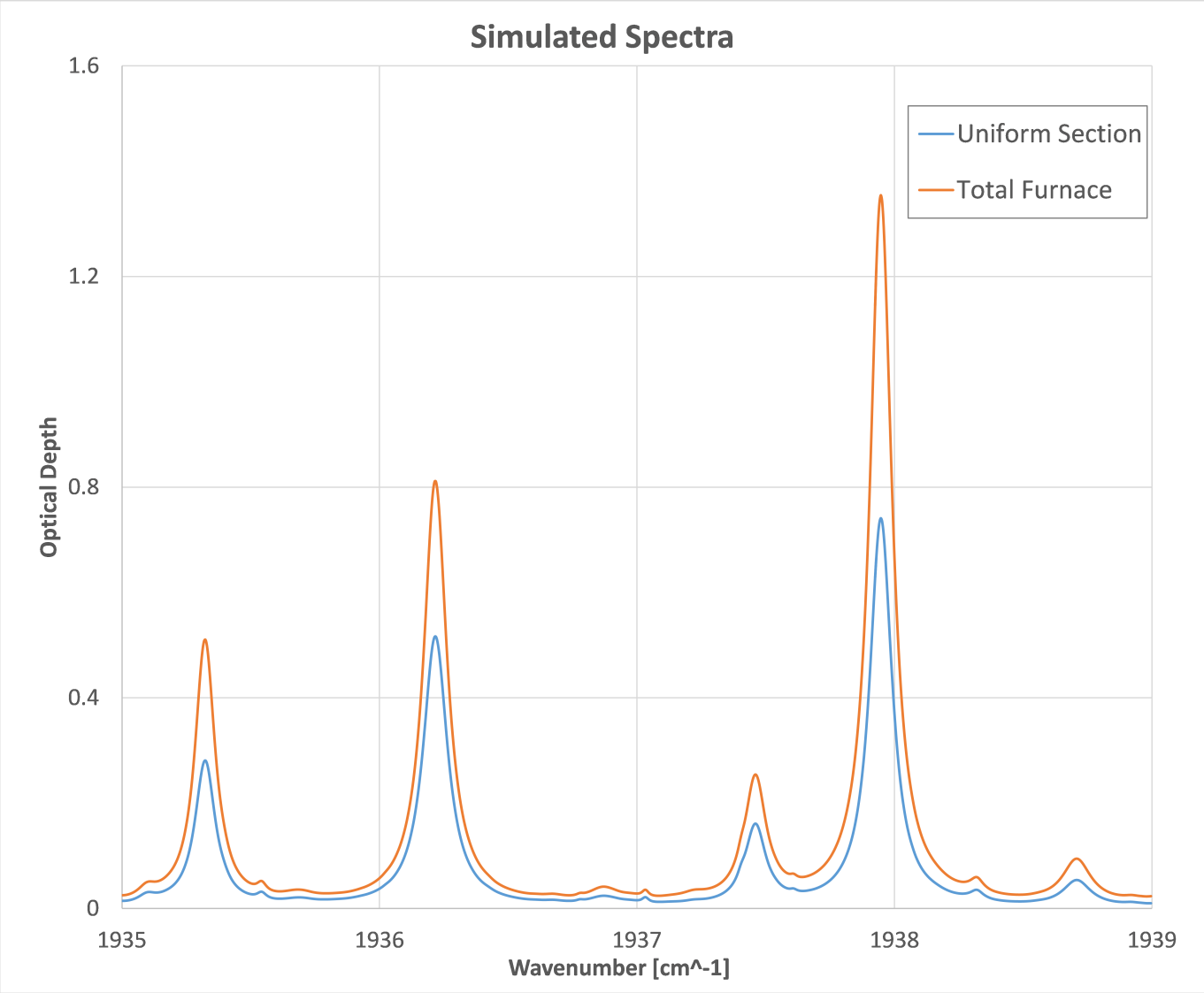

Figure 3.6: Comparison of two simulated spectra obtained for 10% H_2O by volume at 1800K. The uniform data set includes only the uniform region at the center of the furnace while the total furnace data includes the entire length the cell.

outer tube that forms the cell with single-side beveled windows epoxied as inner caps, using a high-temperature alumina and water based epoxy, to create a gas-tight seal [12]. A schematic of this design is shown in Figure 3.7.

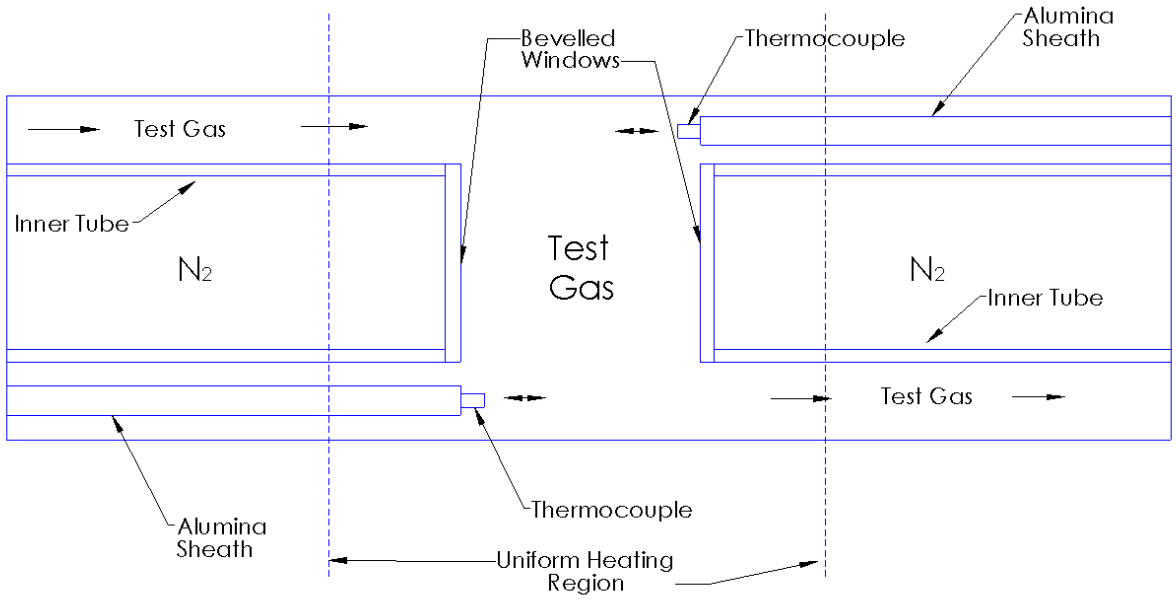

Figure 3.7: Schematic of a three-zone gas cell with axial thermocouple measurements. The N_2, or nonreacting, regions are contained by the inner tubes and the laser enters from left to right. Not shown are the flanges that cantilever the inner tubes.

In addition to removing temperature gradients from absorption measurements, this design adds the capability of making temperature distribution measurements during testing, which is not possible using the UTSI system, by leaving room for alumina sheathed thermocouples at the same radial distance from the center as the inlet/outlet. The sheaths are secured and end just outside the testing region, but the thermocouples can be adjusted horizontally, allowing for axial temperature measurements to be made. In a typical high-temperature gas cell, beveled windows are used to prevent reflections of the laser, as anti-reflective coatings limits the maximum temperature of the windows to below the ∼1300 K capability of sapphire. The window material will be dependent on the wavenumber of the laser, which depends on the lines of interest. For mid-infrared studies of combustion gases, sapphire has high transmission (>80%) over the 2000-35,000 cm^{-1} range (Figure 3.8 [31]) with high temperature capabilities

and is, along with quartz [6, 9], one of the window materials most often seen when infrared lasers are used [10, 12]. Sapphire was initially chosen in this case for the transmission capabilities at wavelengths in the 5 μm range.

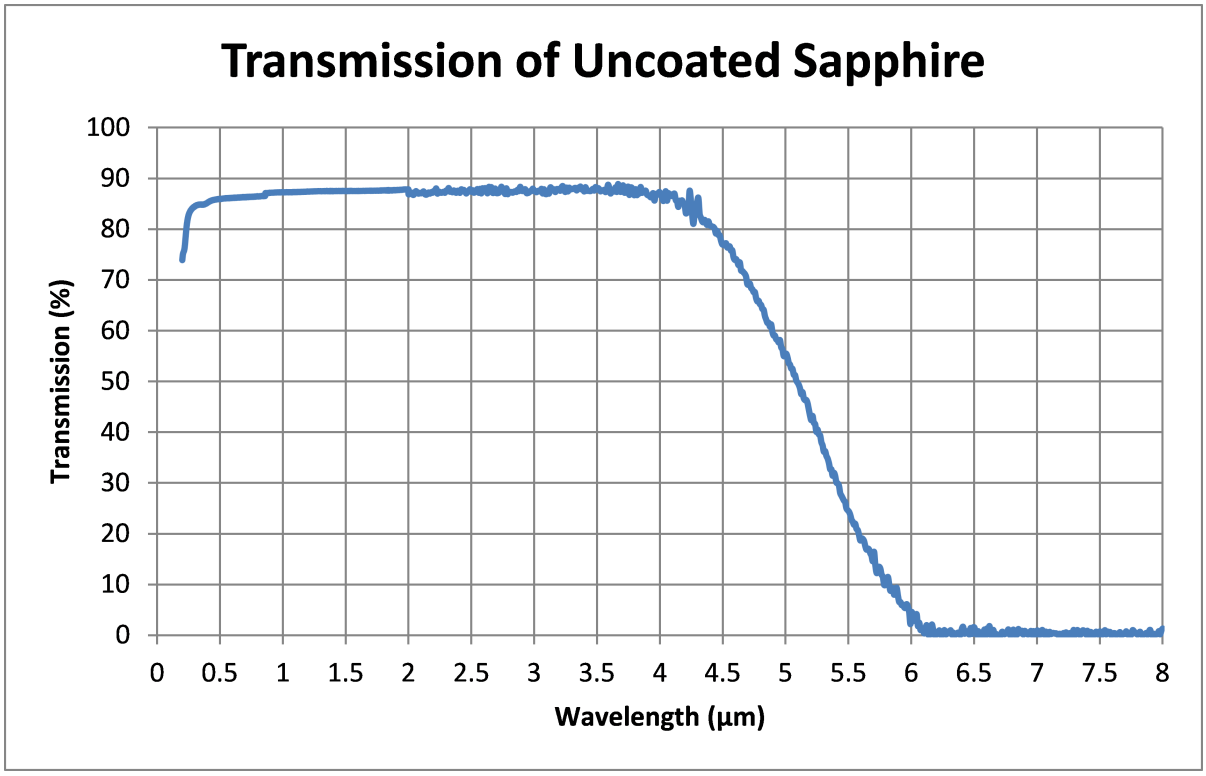

Figure 3.8: Transmission curve obtained from ThorLabs, Inc. for 5mm thick uncoated sapphire window at 350K.

Nitrogen gas (N_2) has negligible absorption in the mid-infrared range at the temperatures obtained in engine combustion, with less than 0.001% reduction in transmission at combustion temperatures for the mid-IR region. This makes it ideal for both diluting sample gases and filling the non-reacting region [10, 12, 14, 15, 32]. The sample gas enters the cell through an inlet and flows along the length of the non-reacting tube. In a static test, the furnace would then be set to heat the gas to the desired temperature. In a flowing test, a flow rate that maintains the temperature uniformity of the central test section would be maintained. Flowing tests are generally preferred because any outgassing or leaking effects are minimized and the resulting Doppler shifts (Eq. 2.2) are negligible at low speeds. The remaining space between the non-reacting region and gas cell wall are used for thermocouples or pressure gauges. The thermocouples run parallel to the non-reacting zones and are

sheathed in an insulating material, such as alumina (Al_2O_3), to reduce conduction effects due to the non-uniform temperature regions. The sheath remains fixed while the thermocouple can be fed through, allowing one to make axial temperature measurements along the uniform region. This is particularly useful during flowing tests, where higher flow rates alter the temperature profile of the test gas.

A prototype of this design was built and tested by Christiansen, Stolberg-Rohr, Fateev, and Clausen at the Technical University of Denmark [12]. The inner and outer tubes of the cell and thermocouple sheaths were made of alumina, a high-temperature ceramic that exhibits high strength at temperatures approaching 2000K [12]. The beveled windows were made of sapphire and bonded to the ends of the inner tubes using a glass bond that was not listed. Sapphire and alumina have similar coefficients of thermal expansion of 5 - 8.3×10^{-6} (perpendicular to optical axis at 273-1273K [33]) and 6.7 - 9.8×10^{-6} (273-1273K [34]), which reduces thermal stresses that can cause leaks in the glass bond. A water-cooled brass flange was epoxied to the outer alumina tube using a high-temperature epoxy (J-B Weld) that is rated for up to 383K. The cell is housed in a thermally insulated box with three distinct heating coils protected by ceramic beads. One is centered on the uniform test section with one coil on each side. Each coil uses separate heating, temperature monitoring, and temperature control to offset temperature gradients. Additionally, six ceramic sheaths flank the non-reacting zones that can house thermocouples capable of measuring the axial temperature distribution in the test section. Christiansen, et al. did not mention the presence of gradients in the test section due to buoyancy effects, but it's assumed that the reported temperature distribution was obtained as an average of thermocouple readings from the six sheath locations. The maximum operating temperature of this cell was reported as 1300K with a pressure range of 1-200 bar. The uniformity of the reported temperature profiles in the test section for two temperature settings were 445K$\pm$2K to 1000$\pm$1K, which indicates an extremely low temperature uncertainty contribution to the total error.

The materials listed for this cell were chosen for high temperatures and pressures. High-purity alumina has a maximum operating temperature of 2000K. Alumina-based epoxies, such as Resbond® 940HT alumina adhesive, which is used to bond alumina and sapphire, are commercially available for temperatures close to 2000K. The maximum operating

temperature of sapphire windows is typically reported as 1300K, but the melting point is 2300K. However, according to ThorLabs, Inc.® sapphire starts to become soluble to water at temperatures above 1300K, but water is a primary species of interest in combustion gas analysis. This is likely why the maximum temperature of the cell created by Christiansen, et al. was reported as 1300K. The transmission of sapphire obtained from ThorLabs, Inc.® is shown in Figure 3.8. The right side of the curve shifts towards lower wavelengths as temperature of the window increases, which leads to transmission deficiencies for lasers near 5 μm. One potential replacement is Spinel ($MgAl_2O_4$), which has a nearly identical transmission curve that extends to slightly higher wavelengths. Spinel also has a slightly higher melting point than sapphire, but the author could find no reference to the water solubility of the synthetic optical material at elevated temperatures.

The intent is for a cell of this general design to be built as a replacement for the current UTSI gas cell to circumvent the temperature gradient problem, allow for temperature measurements during testing, and extend the maximum temperature of measurable lines. The construction of the body of the cell consists of three-piece stainless steel flanges, a single alumina outer tube, two alumina inner tubes, and two single-side beveled windows. The flange is the primary difference between the cell built by Christiansen, et al. and the proposed cell for UTSI. Brass is a potential substitute if the water cooling configuration requires internal piping, but all simulations herein assume that the material is 304 steel, because the current flanges are made of that material. The configuration builds on the current flange design in use at UTSI. In the order referenced from furnace outward, the first and second pieces of the flange share a seat that holds an O-Ring on the surface of the outer tube. Tightening these flanges together forces the O-ring onto the outer tube surface. These two pieces are shown in Figure 3.9.

The second flange seats on the end of the outer tube. The third flange contains a slot to hold the inner tube in place using epoxy, allowing it to cantilever inside the outer tube. This piece is shown in Figure 3.10. The second and third pieces of the flange are bolted together with an O-ring seal. The third piece contains a vertical port to allow for the continual purging of nitrogen during testing. The second and third pieces each contain a port for an

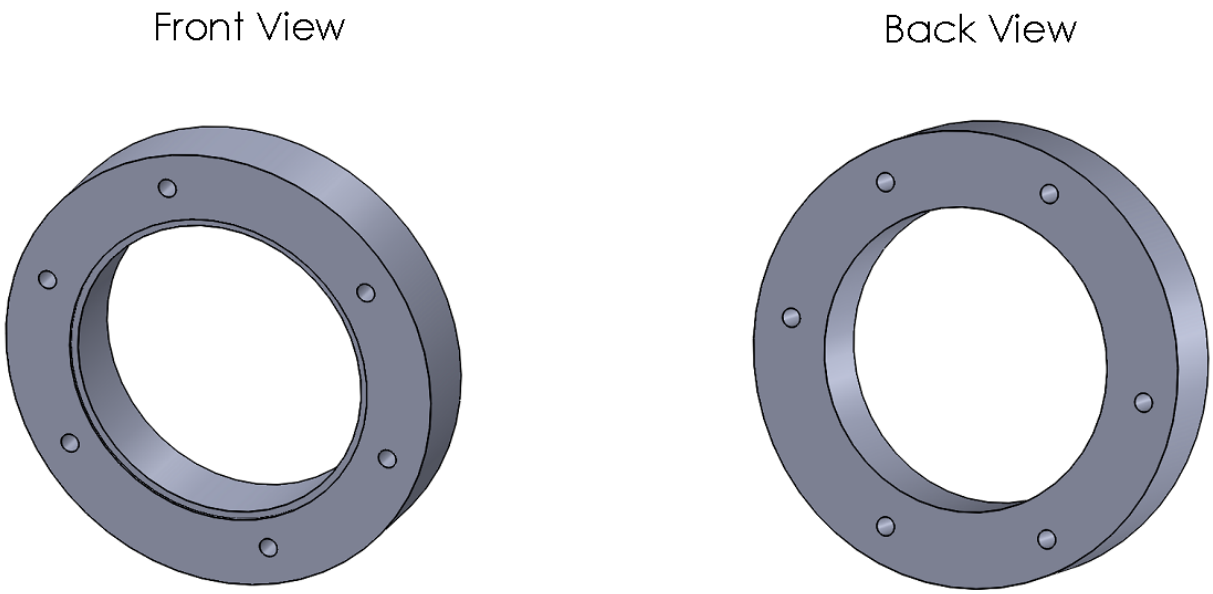

(a) FlangeOuter1

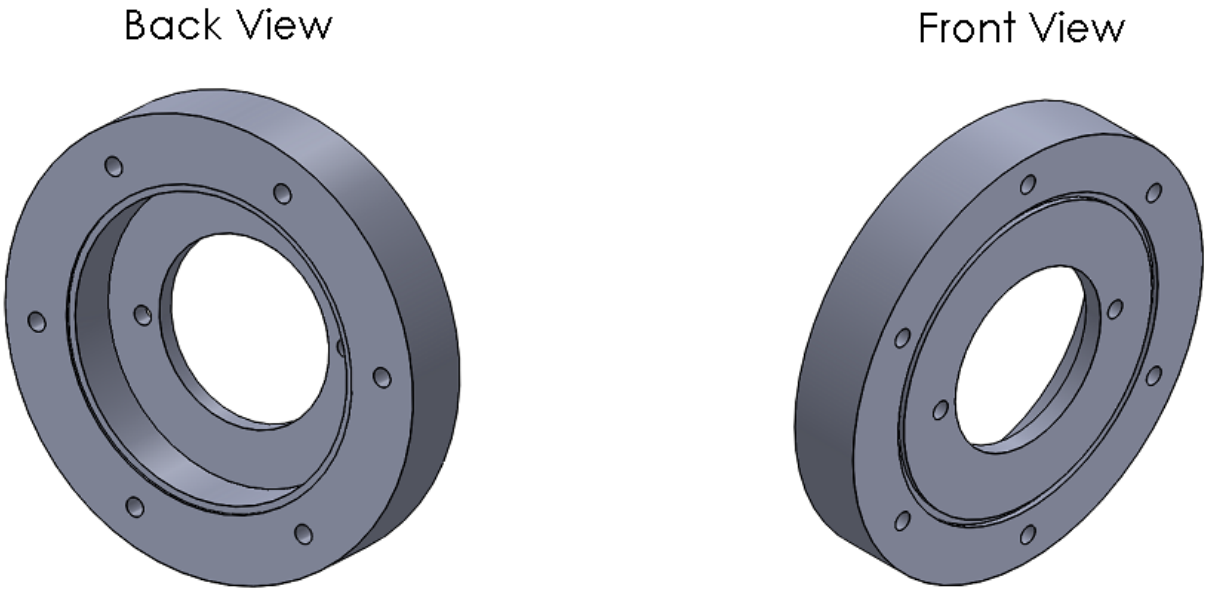

(b) FlangeOuter2

Figure 3.9: The first two pieces of the flange relative to the furnace. On the front view of Figure **(b)** are the ports for the inlet/outlet and measurement devices.

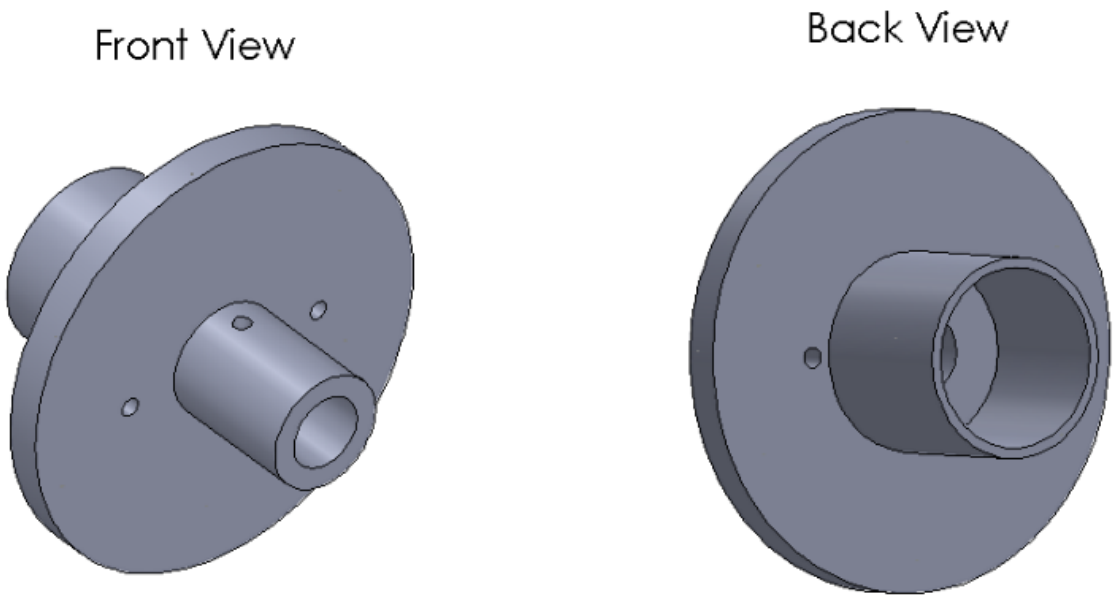

Figure 3.10: The third piece of the flange relative to the furnace. The port on the front view contains an inlet to allow for continual N_2 purging of the inner tube, and the bores flanking the port are for the inlet/outlet and thermocouple.

inlet/outlet and thermocouple, with room for additional ports at the same radial distance as needed.

In order to reduce conductive, convective and radiative effects between the bead of the thermocouple and the entry location, a fixed alumina sheath will be used up to the test section. This sheath will allow a thin thermocouple to be adjusted horizontally to allow temperature readings during both static and flowing tests. One thermocouple must be used on both the top and bottom of the cell relative to gravity to account for buoyancy effects or potential temperature non-uniformity, though early simulations show these effects to be minimal in the new cell when used in static mode. A Solidworks® model of the flange combination and a sectioned view are shown in Figures 3.11 and 3.12 without O-rings, epoxy, bolts, or thermocouple sheaths shown. Complete drawings including dimensions for each piece of the flange are included from Figures 3.13 to 3.18. These drawings also do not show the O-rings, bolts, or epoxy and are taken from SolidWorks®.

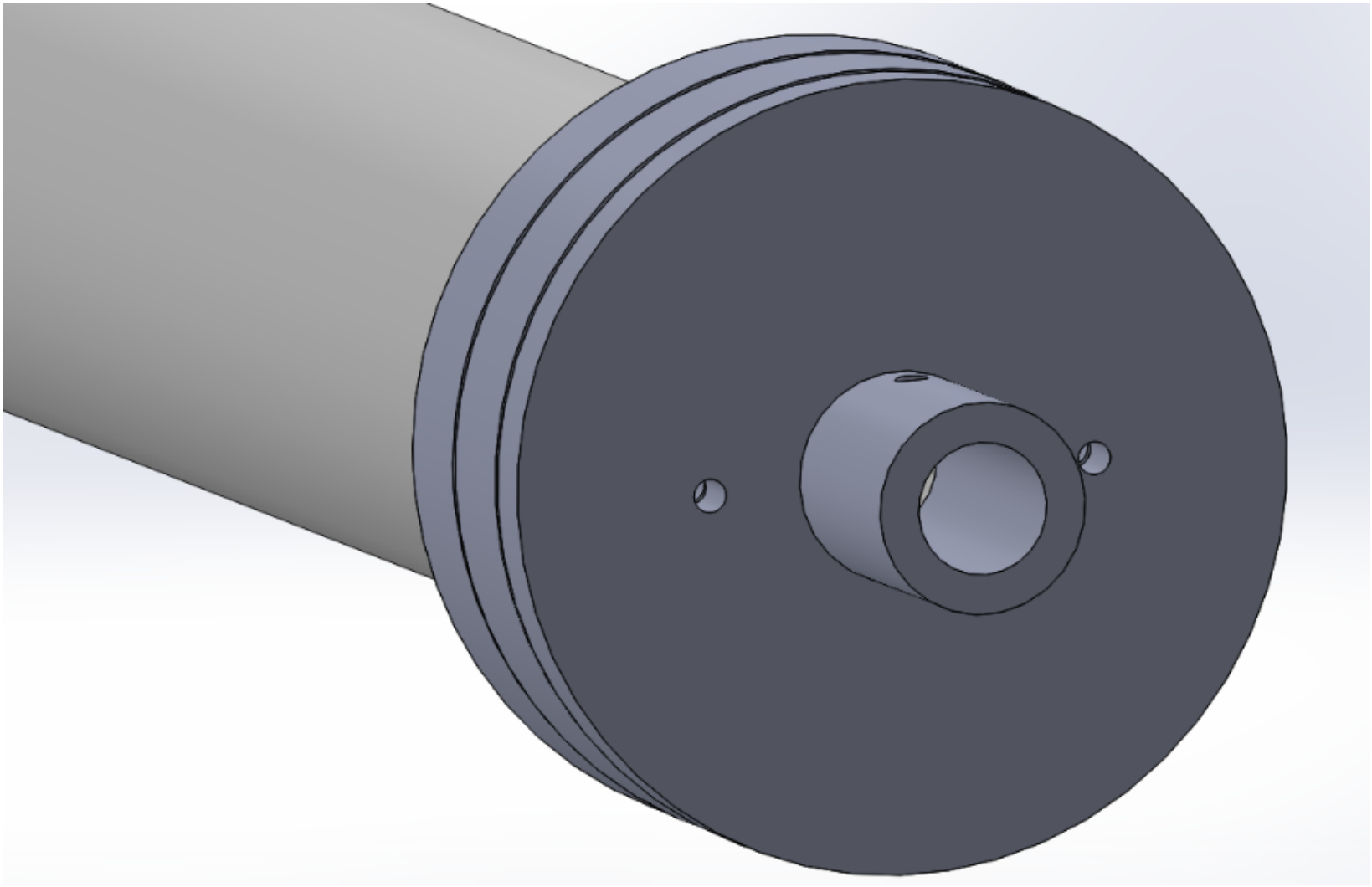

Figure 3.11: Sectioned view of one flange, inner tube, and the outer tube of the proposed cell. Not shown are the O-rings, window, bolts, epoxy for inner tube, inlet/outlet, or alumina thermocouple sheaths. Image taken from SolidWorks ®.

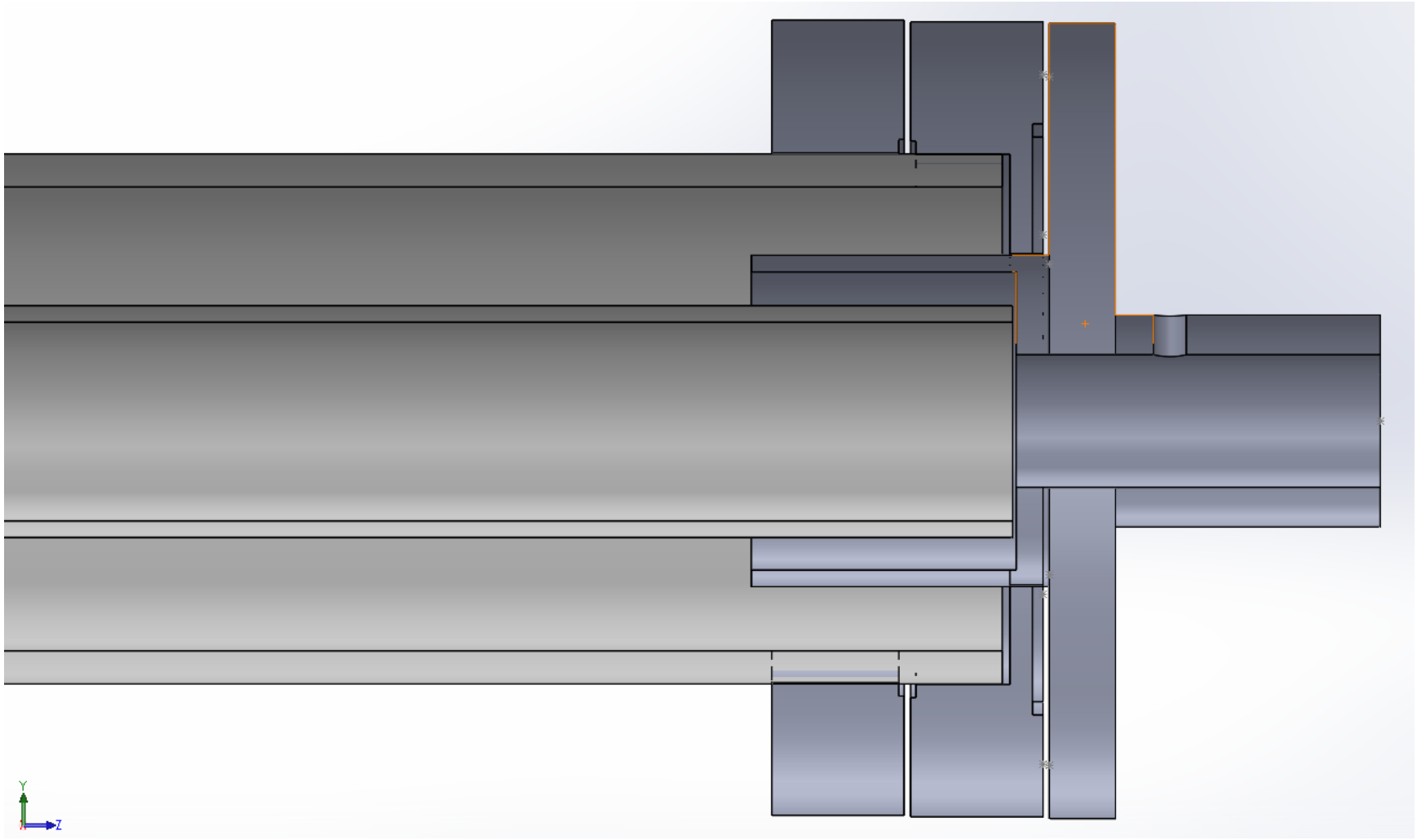

Figure 3.12: Sectioned view of one flange and the outer tube of the proposed cell. Not shown are the O-rings, windows, inner tube, bolts, epoxy for inner tube, or alumina thermocouple sheaths. Image taken from SolidWorks ®.

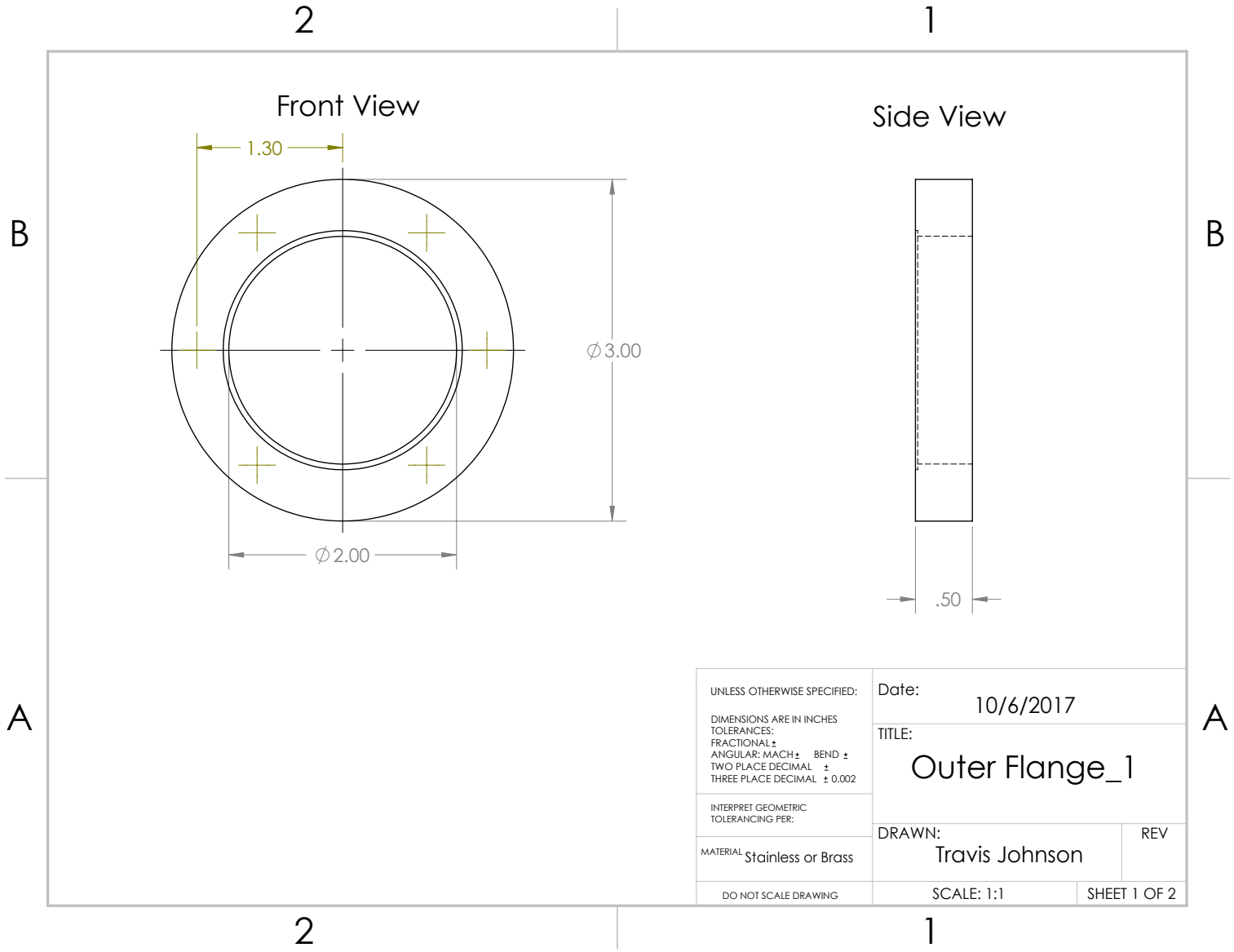

Figure 3.13: Page 1 detailing the first piece of the three piece flange. Image taken from SolidWorks ®.

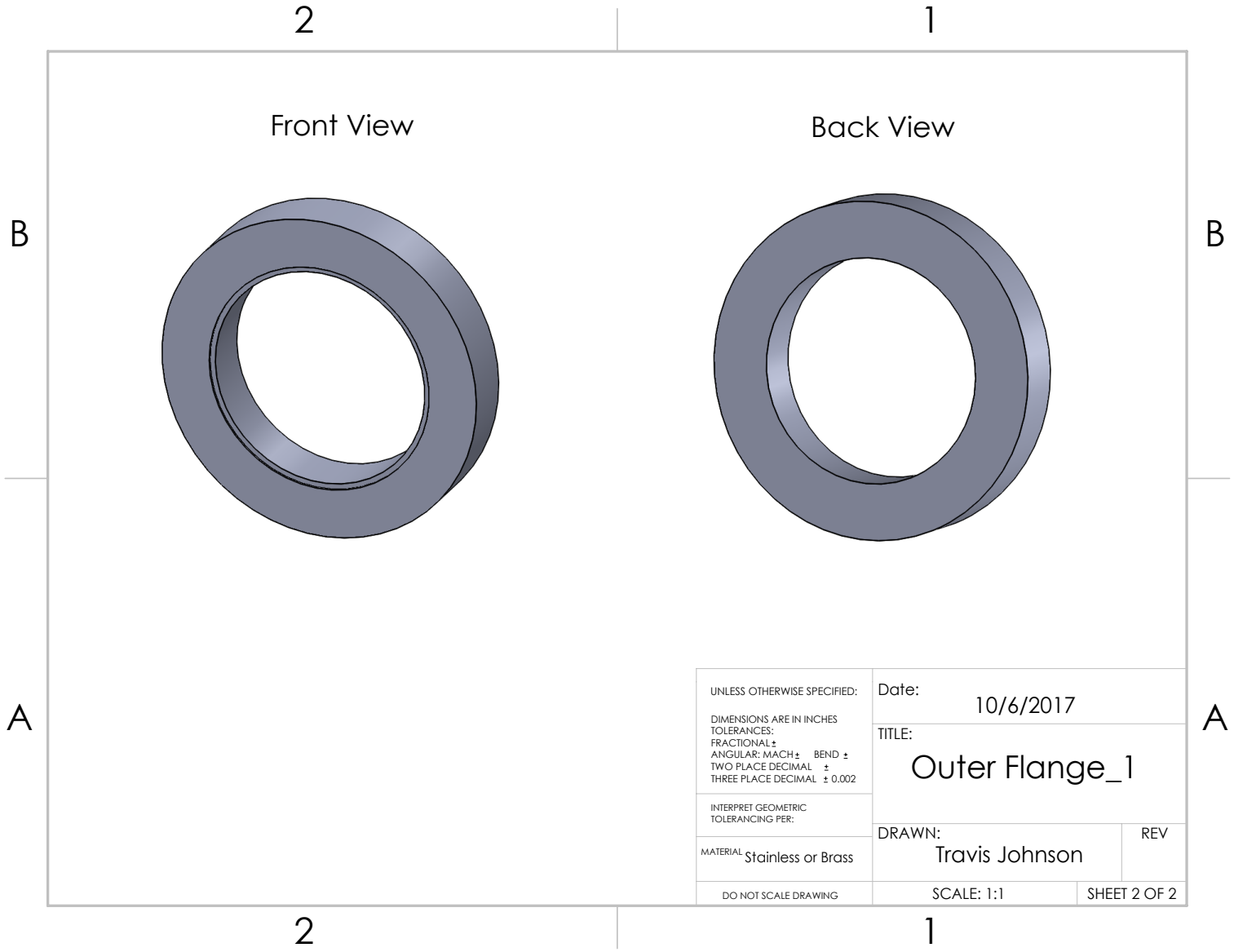

Figure 3.14: Page 2 detailing the first piece of the three piece flange. Image taken from SolidWorks ®.

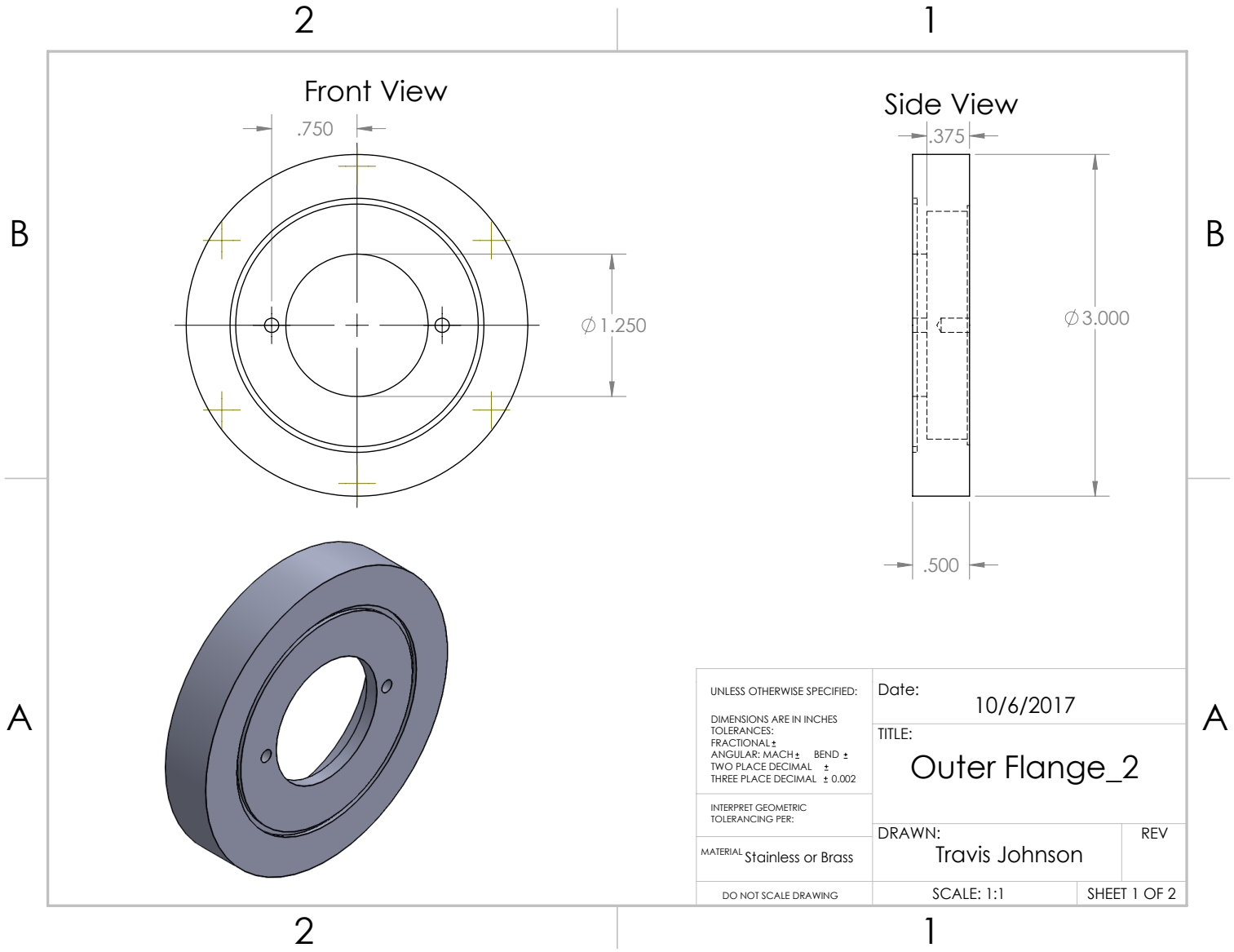

Figure 3.15: Page 1 detailing the second piece of the three piece flange. Image taken from SolidWorks ®.

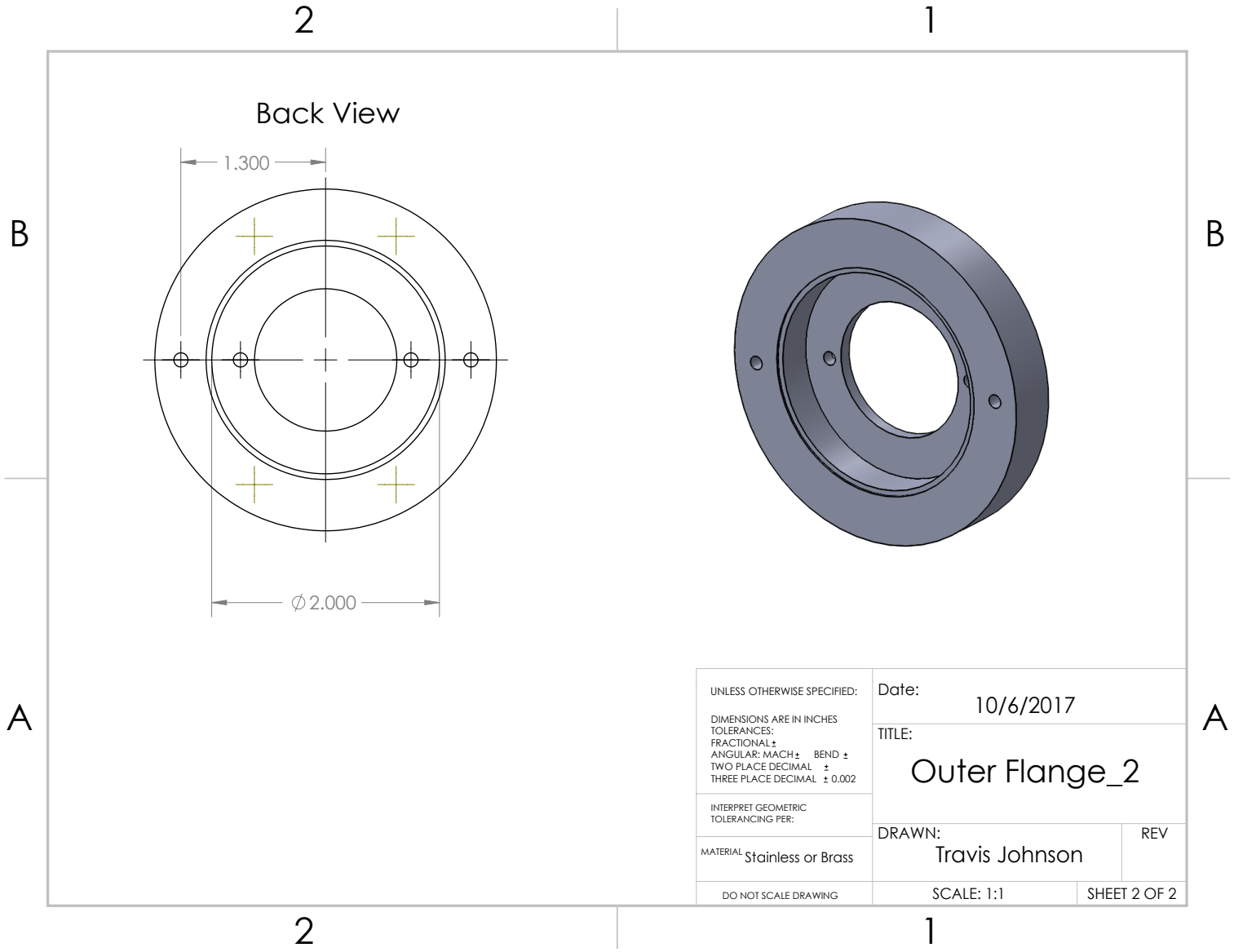

Figure 3.16: Page 2 detailing the second piece of the three piece flange. Image taken from SolidWorks ®.

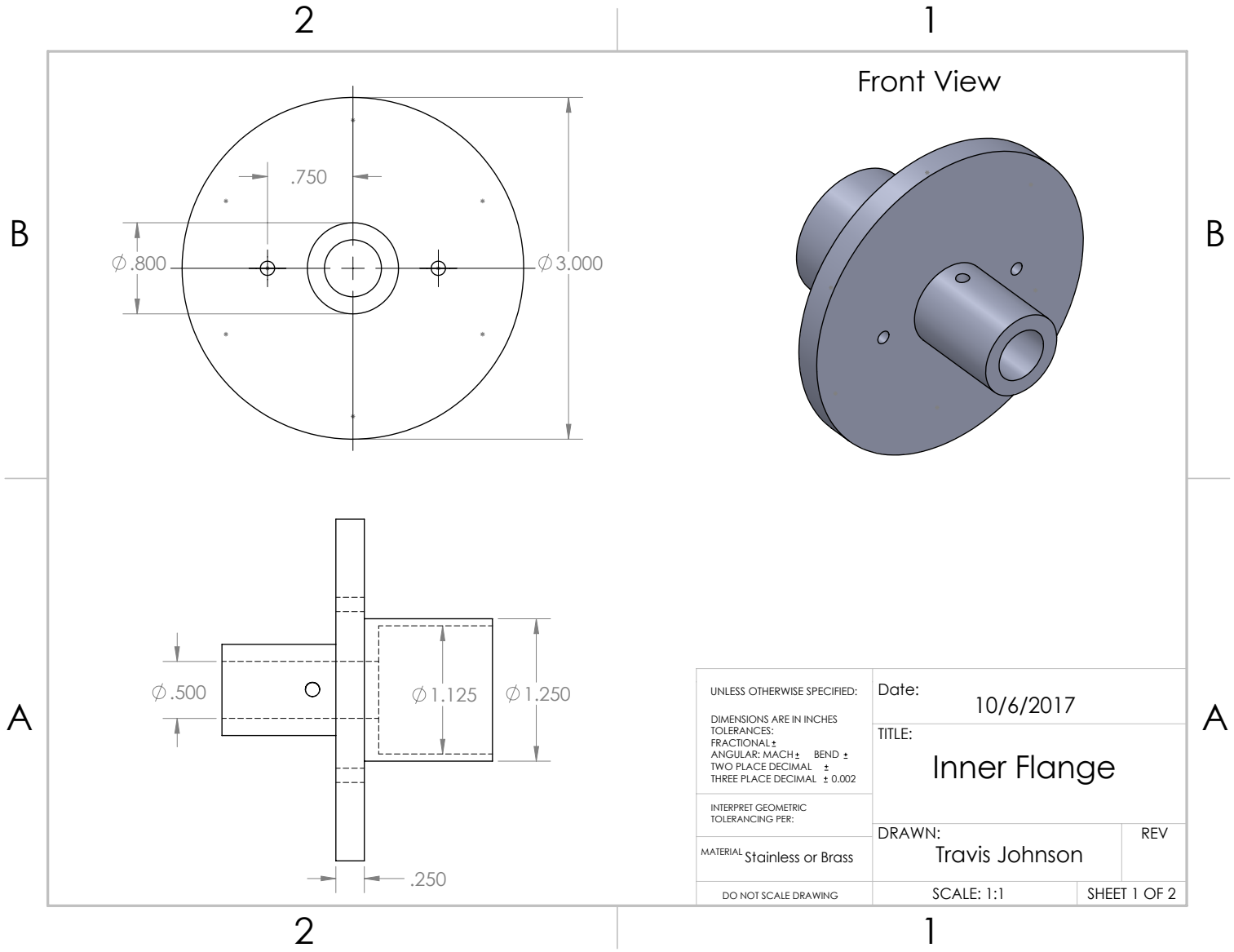

Figure 3.17: Page 1 detailing the third piece of the three piece flange. Image taken from SolidWorks ®.

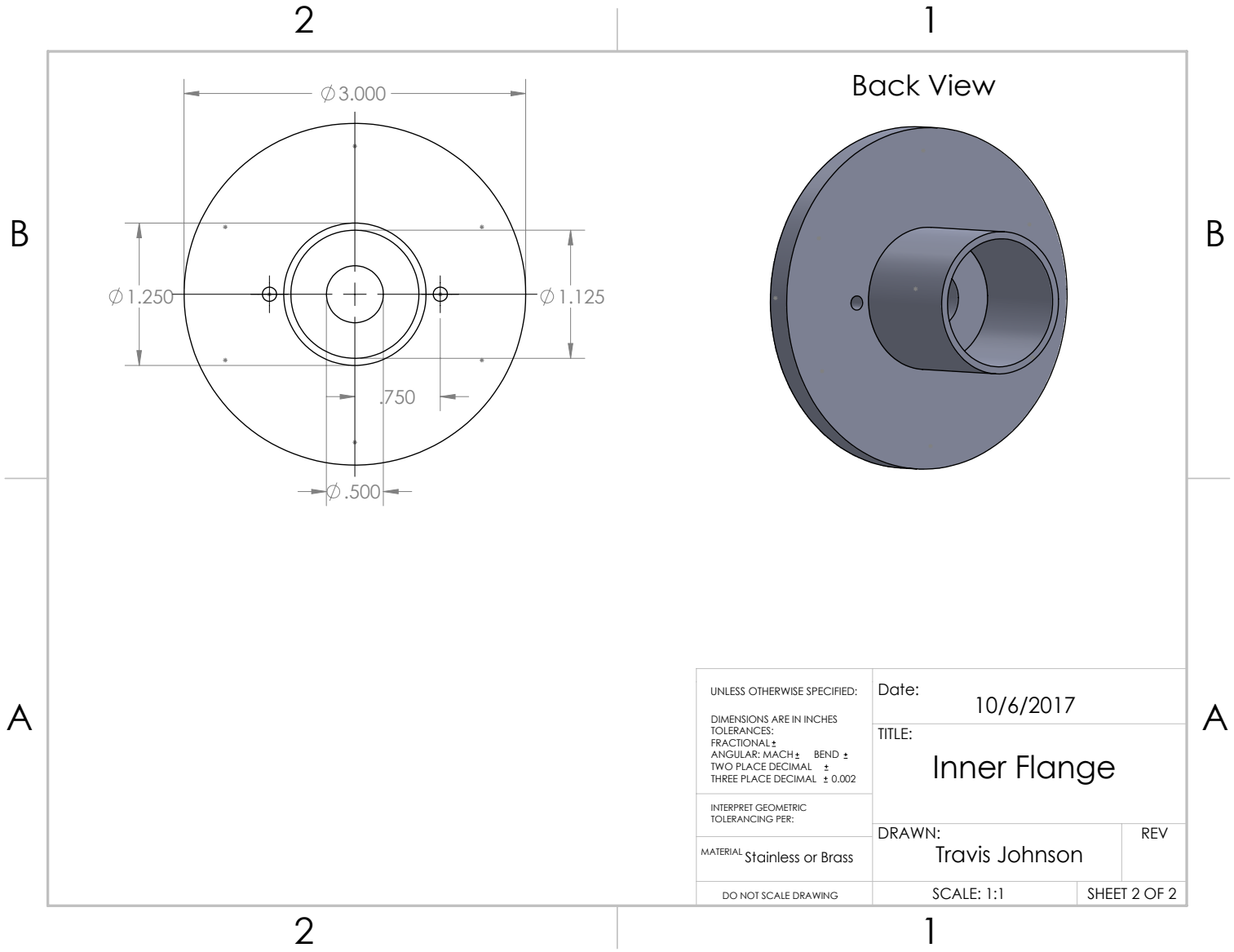

Figure 3.18: Page 2 detailing the third piece of the three piece flange. Image taken from SolidWorks ®.

3.3 Absorption Cell Simulations

Before the construction of the cell, computational modeling and simulation software, using a CFD and thermal model, has been utilized to verify design modifications required to account for temperatures up to 1773K and to verify the temperature uniformity for the chosen test section width. The maximum temperature is based on the tube furnace chosen and maximum temperature of the materials, but the maximum operating temperature will be set from transmission measurements using spinel or sapphire. The furnace chosen for this design is the Mellen Series Single-Zone TS15.5, which is a tube furnace capable of temperatures up to just over 1800K (1550°C) with a recommended maximum continuous operating temperature of 1773K [35]. The single-zone version would be preferable because the uniform section of the furnace need only extend just past the sapphire windows on the inner tubes, which will only be a few inches apart, and the CFD models use that configuration. The spacing between the windows will be adjustable by using inner tubes of different lengths and should be chosen based on the concentration and temperature of the absorbing species to avoid cases of low transmission. A single-zone will also reduce the temperature of the flanges, because it decreases the width of the uniform section, meaning that the temperature falls off closer to the center of the furnace than is the case in the current UTSI furnace.

To reduce computational time, each CFD model uses quarter symmetry. The cell is symmetric about the centerline of the furnace perpendicular to the cell and about centerline of the cell parallel to the gravitational direction vector and perpendicular to the opening of the cell. While this prevents fully 3D buoyancy effects from resolving, it was found that temperature values closely modeled measured values made using the K-type thermocouple when using this symmetry method. The geometry of the UTSI furnace and cell with the boundary conditions highlighted is shown in the in Figure 3.19. Each model will also use a single-piece solid flange excluding all O-rings and bolts. The window is treated as a solid piece of sapphire that is the size of the sapphire window and Teflon ring, and the lip between the quartz tube and window is not included. All test gases and nitrogen are treated as air. The heating component of the furnace is simulated by splitting the furnace into two sections. The first section corresponds to the region of uniform heating given by the manufacturer, and

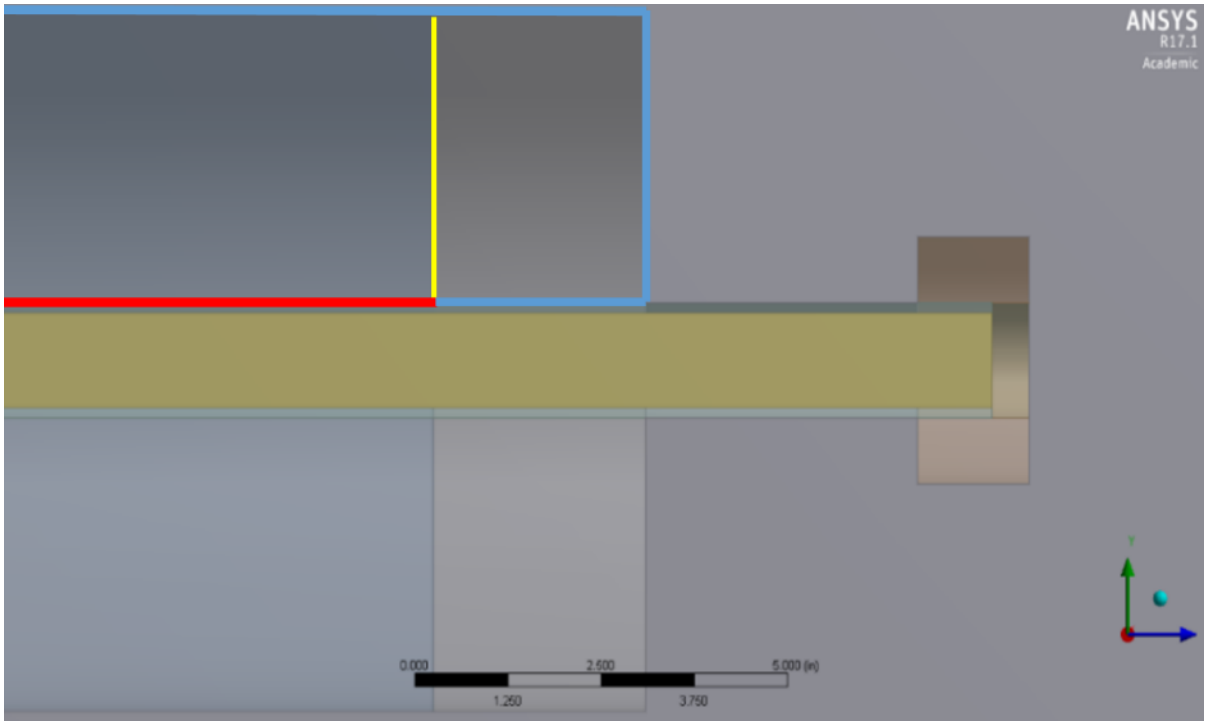

Figure 3.19: Model of the current UTSI cell and furnace in ANSYS® Academic Research Design Modeler, Release 17.1 using quarter symmetry and a simplified flange. The red line indicates where the set temperature of the furnace is applied, the blue lines indicate adiabatic boundary conditions, and the yellow line indicates a coupled wall. Image used courtesy of ANSYS®, Inc.

the boundary between the quartz cell and furnace is set to the furnace temperature. This temperature boundary condition was chosen because the temperature readings of each coil's thermocouple determine the amount of current supplied, which means that the heat flux from each coil is constantly changing before reaching steady state. This makes setting the boundary temperature preferable to creating a volumetric source term or heat flux boundary condition. The boundary between the unheated furnace section and quartz tube is treated as an adiabatic boundary with zero heat flux. This was found to be necessary to properly simulate the temperature gradients near the edges of the furnace as measured in Figure 3.3, as leaving it a coupled wall, which is the usual boundary condition between solids, results in a distribution that fails to match the thermocouple readings (Figure 3.20). The reason for the necessity of this adiabatic condition is that the inner insulation and coils of the furnace were not modeled, but the outer edges of the entire furnace were treated as adiabatic because the outer surface of the furnace, which is insulated and was not measured during testing,

is not too hot to touch. The set condition of the heated section in combination with the adiabatic boundaries therefore raises the entire furnace to the same temperature, creating an incorrect gas temperature distribution, when the wall between the unheated furnace section and quartz tube is left coupled. Finally, for the proposed three-zone absorption cell, the alumina-based epoxies were treated as part of the inner alumina tube.

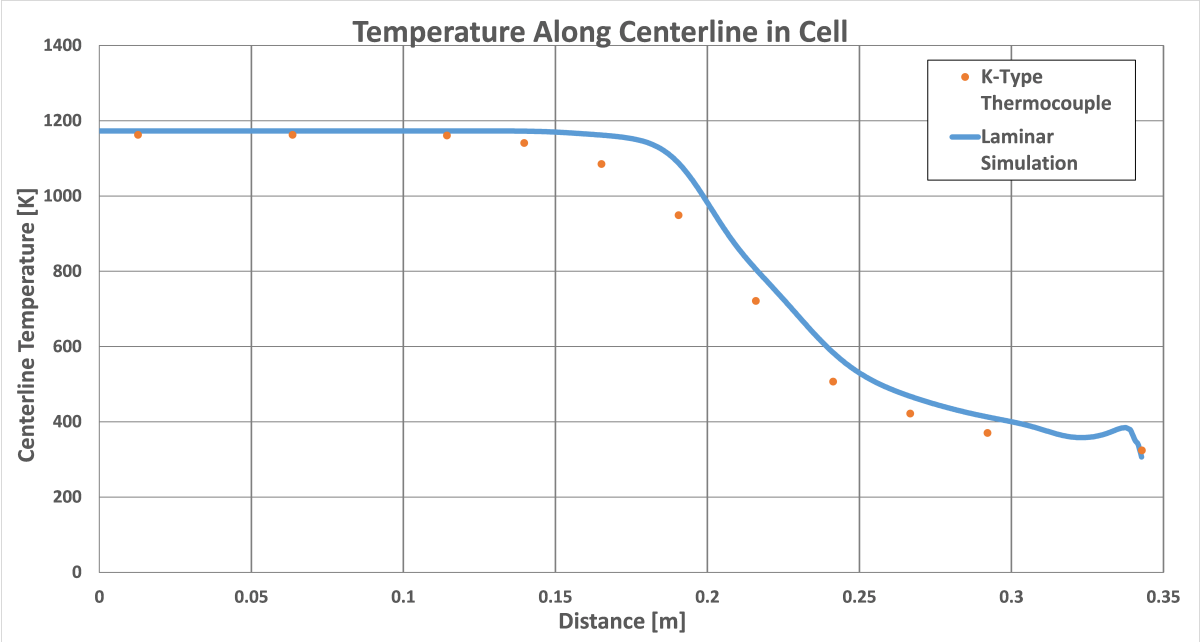

Figure 3.20: Initial results of the current UTSI furnace without the adiabatic boundary condition between the non-heated furnace section and quartz tube show higher temperature results outside the uniformly heated section than those values measured using the K-type thermocouple.

3.3.1 UTSI Cell

The primary goal of the CFD modeling was to verify that the design would be sufficient to handle the high temperatures achievable with the new furnace. First, a CFD and thermal model was built for the current UTSI cell and furnace to verify methodology and software capability. Because each system contains fluid and solid heat transfer, buoyancy effects, and radiation, ANSYS® Academic Research Fluent, Release 17.1 was chosen for simulations [36]. ParaView® [37] was used to post-process the data exported from Fluent. A simplified geometry of the cell utilizing quarter symmetry was created in SolidWorks® and meshed using the ANSYS® Academic Research Mesh Release 17.1. It is comprised of a quartz

cylinder, stainless steel flange, glass window, and heated and unheated furnace sections and is shown in Figure 3.19. The furnace temperature setting was applied to the boundary between the cylinder and the heated section of the furnace and allowed to propagate through the cylinder.

The ANSYS® help manual [28] recommends using the Rayleigh (Ra) number to determine if turbulence modeling is necessary. The Rayleigh number is the criterion for natural convection because it determines if the primary mode of heat transfer is conduction or convection, and higher convection effects require wall models found in turbulence models. In this case, which uses air only due to the unsealed condition of the cell during temperature measurement tests and similarity to test gases, the resulting values are approximated in Eq. 3.7, with the assumption of air as an ideal gas and a constant temperature of 1173K.

$$\mathrm{Ra}_D = \frac{g\beta\Delta T D^3 \rho}{\mu\alpha} \approx \frac{(9.81)\left(\frac{1}{1173}\right)(1173-300)(0.03556^3)(0.30)}{4.56\times10^{-5}\left(\frac{7.5\times10^{-5}}{0.30\cdot1.17}\right)} = 1.01\times10^4 \tag{3.7}$$

where g is the acceleration due to gravity, β is the thermal expansion coefficient, α is the thermal diffusivity, D is the outer diameter of the cell, ρ is the density of air at 1173K, and μ is the dynamic viscosity of air at 1173K [36, 38].

This is well within the laminar range, which transitions into the mixed regime at 10^8 according to the help manual [36]. This means that fluent directly solves the finite-volume Navier-Stokes, continuity, and energy equations with the implicit assumption that the grid is not fine enough to resolve turbulence effects. The implicit density-based coupled solver, where equations for continuity, energy, and momentum are solved in vector form and pressure is obtained through an equation of state [39], is recommended by ANSYS® for cases with high temperature gradients and natural convection [36], which are both present in these simulations, due to the strong coupling between density, energy, and momentum. The implicit solution approach was chosen because there are no instances of acoustic waves that can limit the time scale of the solution [39], and each solution used the second-order upwind scheme with the Green-Gauss Node-Based interpolation method of determining gradients, though in hindsight a Least-Squares Cell-Based method would have been more appropriate due to the use of the cut-cell style meshes [39].

A viscous mesh with inflation layers for both the inner and outer fluid regions was created using the cut-cell meshing approach available in ANSYS® Mesh for all regions outside the inflation layers. The cut-cell style meshing procedure converts a volumetric mesh into a Cartesian mesh that consists of hexahedral elements with faces generally aligned with the coordinate axes. Smaller elements are used to resolve geometric features [36], and the mesh was grown from solid block (flange, outer tube, etc.) faces in these simulations. Radiation was also considered in this model, and the uncoupled Discrete Ordinates (DO) model was chosen due to the optical thickness $\alpha L << 1$, using the same values given in Equation 3.7, and the presence of a local heat source as recommended by the ANSYS® help documentation [36]. The DO model solves the radiative transport equation for a finite number of discrete solid angles, with an angular discretization using the standard setting of 2 for theta and phi in these simulations. The uncoupled DO version was used, which solves for the radiation and energy intensities separately, due to the low optical thickness of the problem [36]. The mesh used to simulate the current UTSI furnace is shown in Figure B.2 in Appendix B. The model contains separate fluids for the inner and outer regions and requires a transient solution with the ideal gas setting for a furnace setting of 1173K to fully resolve natural convection effects. The material property settings for air, quartz, sapphire, alumina, and 304 stainless steel used are listed in Table A.1 in Appendix A from tables, with constant values used when temperature-dependent values were not available from a reliable source [25, 28, 33, 34, 38, 40, 41, 42].

The procedure for obtaining a solution was to initialize the simulation with low specific heats for the solids and immediately patch both furnace sections to the set temperature of the furnace. This significantly reduced computational time and was done for all simulations presented here. For determining convergence, the simulation residuals were found in all cases to be well above the recommended convergence criteria in the ANSYS® help documentation. This is due to the scaling methods of the Fluent® code, which states "In the case of natural convection in an enclosure, for example, initial momentum residuals is....not a good scale for the residual" and that instead residuals should be judged so that "...the residual continues to decrease (or remain low) for several iterations (say 50 or more) before concluding that the solution has converged." This was found to be true for the momentum and velocity

residuals, where the residuals were required to reach a steady-state value as one indicator of convergence. This effect arises because the solver's initial guesses used for those residuals' scaling are essentially zero due to the starting condition of everything at 300K and not moving, which is only true for several iterations until heat has propagated away from the set temperature boundary condition. Scaling values after those iterations by this initial guess therefore causes residual values to be elevated well above the 10^{-3} criterion suggested by Fluent® help documentation. For cases where this situation occurs, Fluent® recommends to "monitor integrated quantities...before concluding that the solution has converged" [36]. The primary indicator of convergence for these simulations was chosen to be the volumetrically averaged temperature of the flange, the furthest block from the heated furnace section for which the temperature values were desired. A plot of the values for the volume-averaged temperature taken from the laminar simulation on the UTSI furnace and cell is shown for reference in Appendex C in Figure C.3.

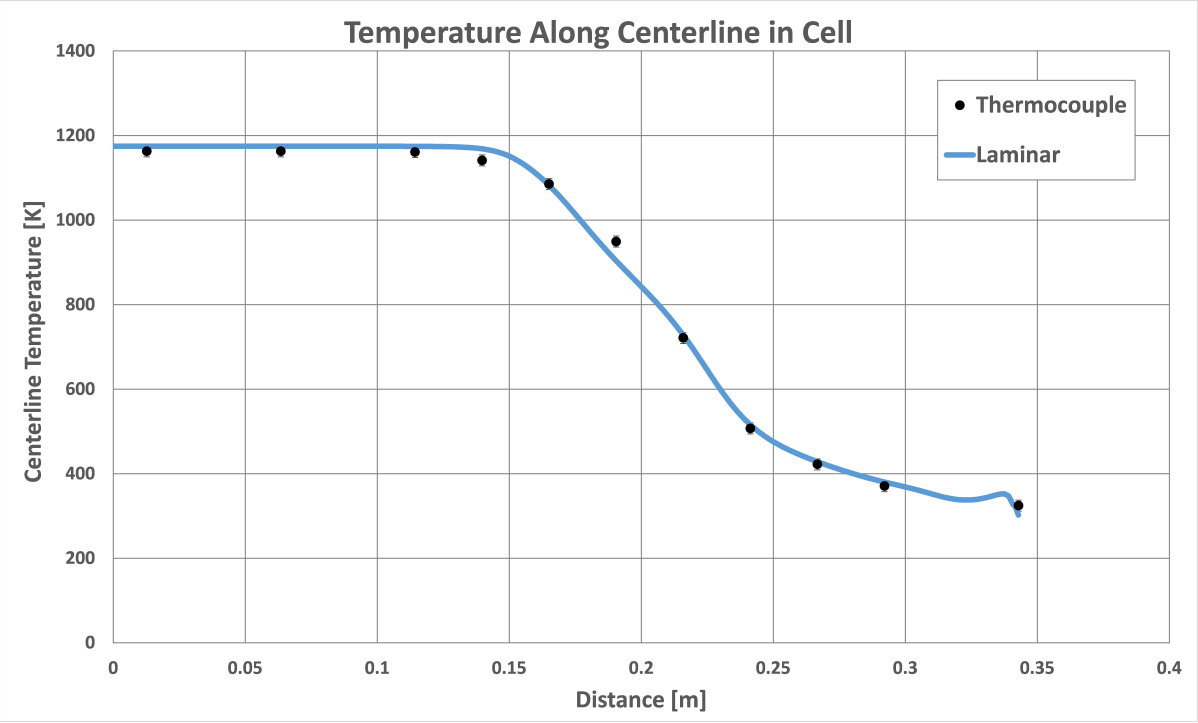

Figure 3.21: Simulation results for the centerline temperature of the current UTSI furnace and cell compared to the K-Type thermocouple. Distance is axial from the center of the furnace.

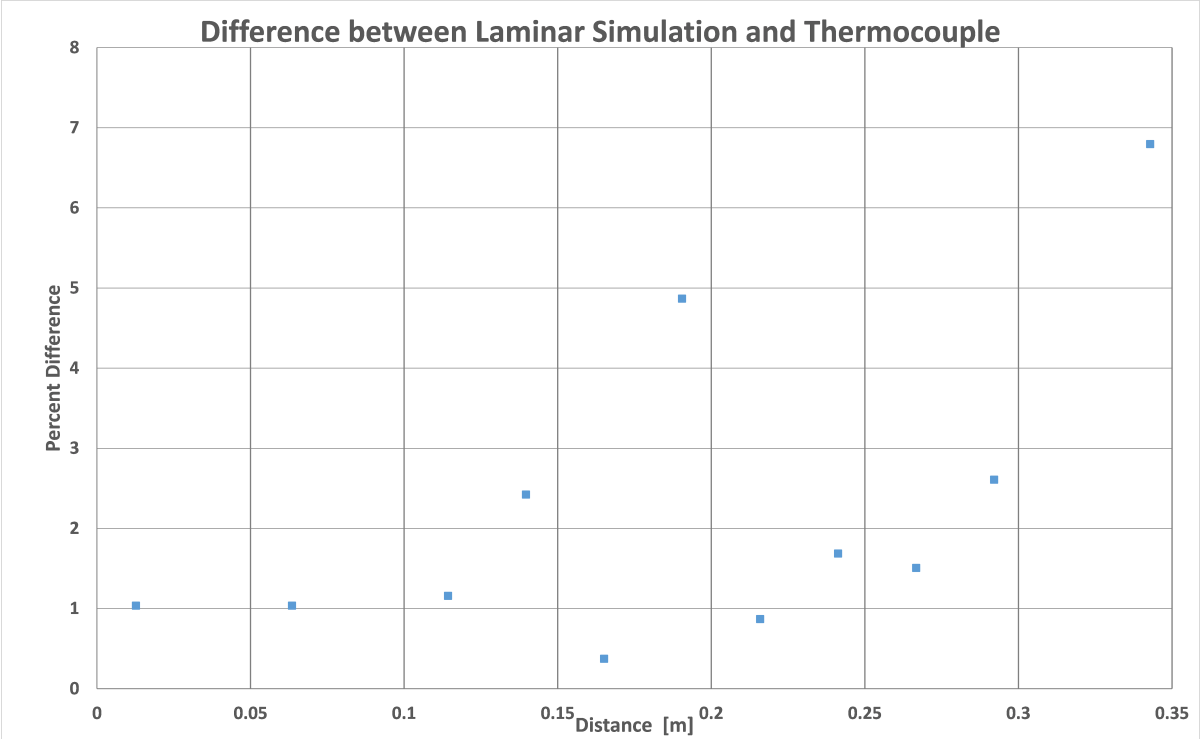

Figure 3.22: Temperature difference between simulation centerline temperatures and measurements made with an K-type thermocouple. Distance is measured from the axial center of the furnace.

The second-order simulation results were obtained for the centerline temperatures by using the "plot over line" feature in ParaView® and are compared to the K-type thermocouple measurements in Figure 3.21. The results show good agreement between the laminar simulation and K-type thermocouple results for the centerline gas temperature. The percent differences found by assuming the thermocouple values to be the true values are compared to simulation results at the same location are shown by Figure 3.22.

The effect of adding the radiation model to this simulation was also investigated. The furnace is treated as a blackbody emitter in the results labelled "Laminar Simulation" shown in 3.23 as well as those seen in Figure 3.21, where the centerline temperature was computed with the Discrete Ordinates (DO) radiation model enabled in Fluent®. This is compared to results found without the radiation model, labelled "Laminar without Radiation", and with the radiation model but the furnace sections are not included as a source of blackbody radiation, labelled "Lam without furnace radiation". The case without the DO model

and the case without the furnace radiation were found to under predict the temperatures measured with the thermocouple.

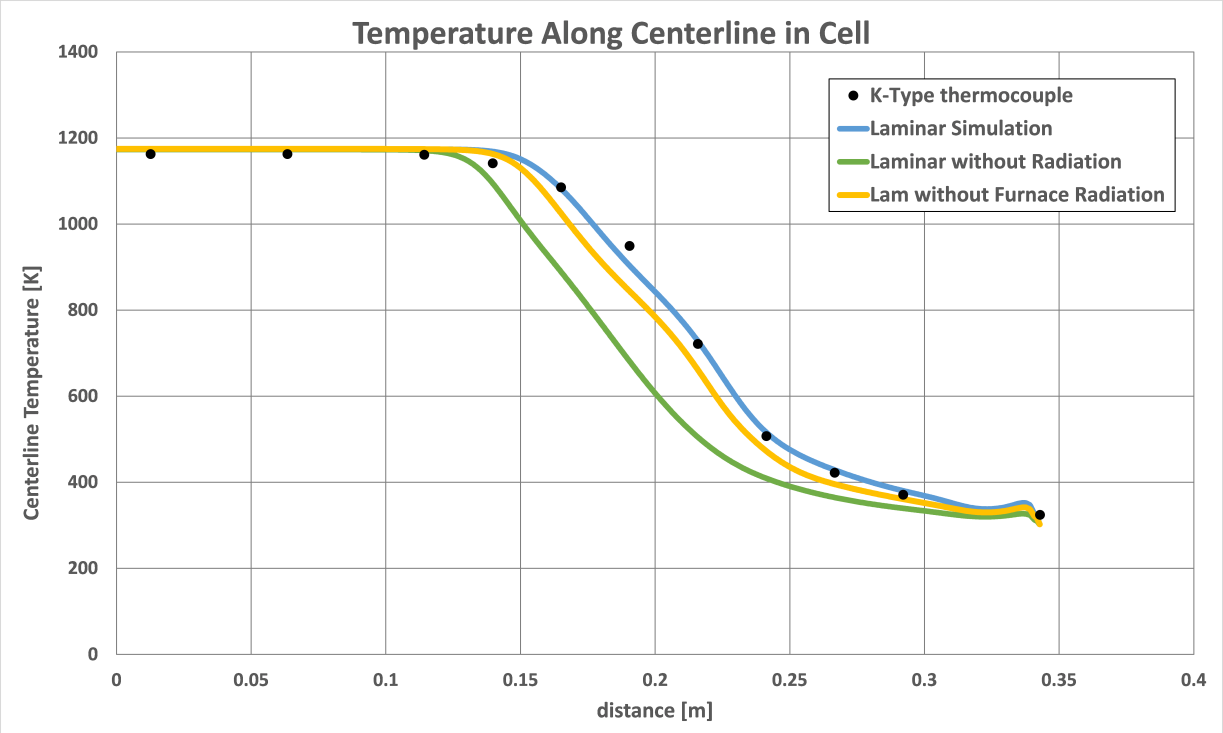

Figure 3.23: Simulation results with different radiation settings using the Discrete Ordinates (DO) Model in Fluent® for the centerline temperature of the current UTSI furnace and cell. These are compared to the measurements taken using an K-type thermocouple. Distance is measured from the axial center of the furnace.

One interesting result seen in all these cases is the rise in temperature just before the last measured value with the thermocouple. This bump is due to the circulation of flow in the quartz tube as the hot, buoyant gas turns in the direction of gravity (Figure 3.24). This effect was not seen with the thermocouple, as no measurement was made in that spacing, and requires additional testing to characterize. Figure 3.24 also includes a temperature contour plot of the entire cell. The velocity magnitude contours of the cell are shown in Figure 3.25, where the mixing inside the cell of the hot gases inside the furnace with the cooler gases outside can be seen.

The secondary measure of the models' accuracy was to measure the temperature of the cell and flange for comparison using a K-type thermocouple. Due to the inherent error attributable to conduction losses when making a surface temperature measurement, the

uncertainty estimate for these values is expected to be on the order of 3K, but additional measurement is required to verify this. This combines with the Reference Junction and Standard K-Type uncertainties to estimate total uncertainties. Those results and the resulting uncertainties compared to simulation values in Table 3.2.

The laminar simulation was found to poorly model the flange surface temperatures. These results were found to be independent of mesh refinement, and are believed to be caused by the geometry simplification of the cell. The actual flange contains a Teflon ring between the steel and the sapphire window that would act as an insulator and prevent some heat flow out of the conductive window. Additionally, the flange contains a lip between the quartz tube and sapphire window which also contains the inlet/outlet port. This is extra contact between the inner air and flange, and some heated gas may rise into the flange, which would elevate the temperature. A second model was created that more closely matches the geometry of the flange, but these values were found to be nearly identical to the previous flange temperatures. The material of the window in the first model was changed to Teflon, but the flange temperatures remained roughly approximate to those found using sapphire. Alternatively, there could be an issue with the inflation layers on the outside of the flange failing to fully capture viscous effects. This was investigated by analyzing the temperature and velocity profiles at four points along the op of the flange. Profiles rising 0.5" (in the y-direction, opposite the acceleration due to gravity) for those four points are shown in Figure 3.26. The velocity values are normalized by the value at 0.5" and the temperature values, T_n, are normalized according to Equation 3.8 by $T_{\max}$, the temperature at the surface of the flange, and T_∞, the temperature at 0.5" of 300K.

$$T_n = \frac{T - T_\infty}{T_{\max} - T_\infty} \tag{3.8}$$

It is clear from the selected locations shown in Figure 3.26 that resolution is lacking in the thermal and velocity boundary layers rising from the outer surface at the top of the flange, so additional work is required to fully resolve these layers to determine how accurately this simulation, with the current assumptions, can match the measured surface temperatures.

Table 3.2: Simulation results for points on UTSI gas cell with a furnace setting of 1173K. Thermocouple measurements are compared to simulation results for points on the exterior of the cell shown in Figure 3.27. "Bot" values are on the opposite side of the "Top" values relative to the y axis. FlangeBot2 is the location of the post and therefore omitted.

Point	Location	K-Type [K]	±Unc. [K]	Laminar [K]	% Difference
1	FlangeMid Top	314	4	302.2	3.75%
2	FlangeMid Bot	312	4	302.0	3.21%
3	FlangeTop1	315	4	302.0	4.13%
4	FlangeBot1	314	4	302.0	3.82%
5	FlangeTop2	316	4	302.3	4.34%
6	FlangeBot2	N/A	N/A	N/A	N/A
7	FlangeTop3	321	4	302.3	5.83%
8	FlangeBot3	320	4	302.3	5.53%
9	CylinderTop1	332	4	320.1	3.58%
10	CylinderBot1	326	4	316.6	2.88%
11	CylinderTop2	356	4	343.1	3.62%
12	CylinderBot2	339	4	350.5	3.39%
13	CylinderTop3	391	4	400.4	2.40%
14	CylinderBot3	388	4	408.4	5.26%

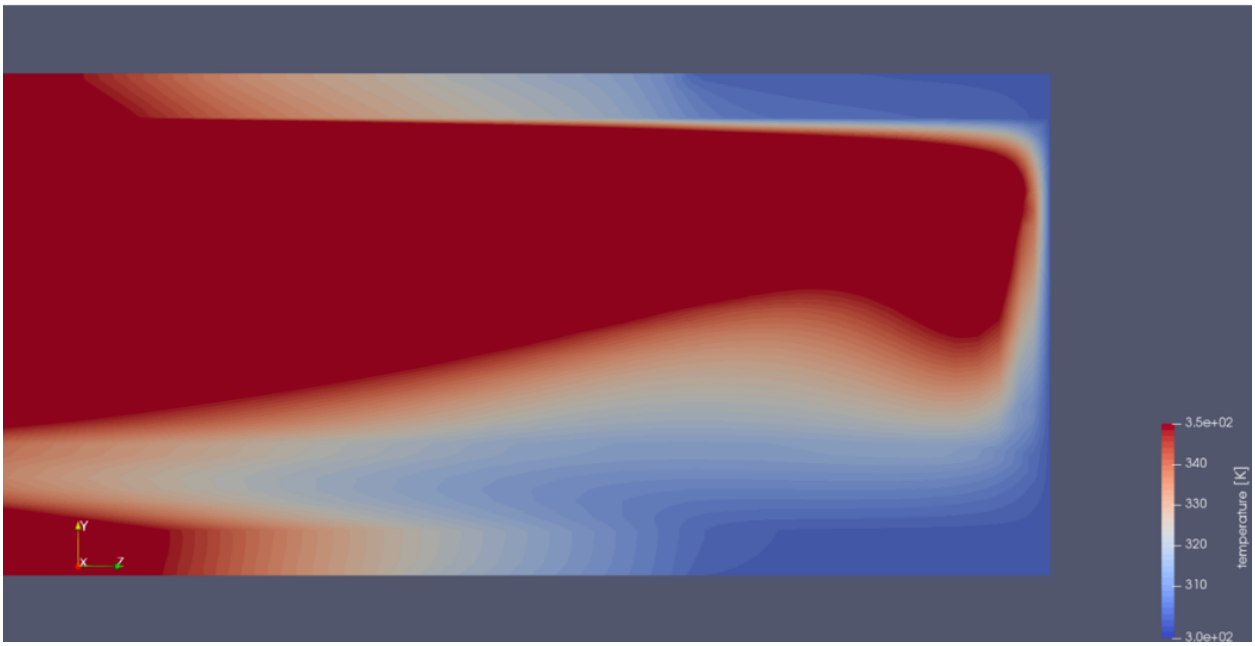

(a) Quartz tube and inner air temperature contour plot

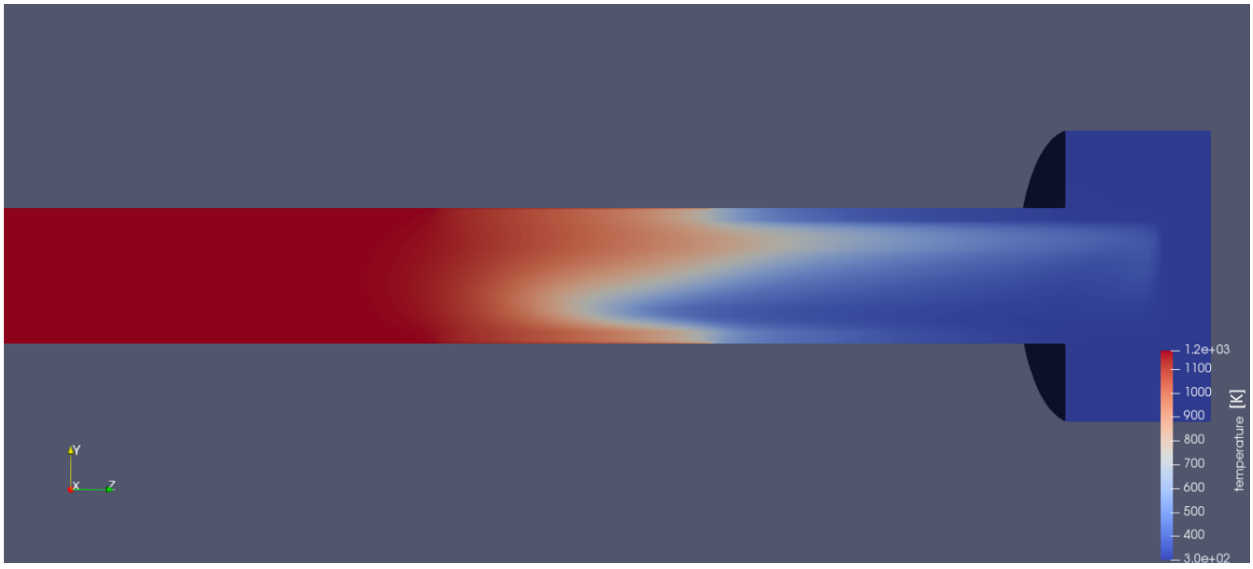

(b) Quartz tube, inner air, flange, and window temperature contour plot

Figure 3.24: Temperature contour plots in Kelvin of the inner air, quartz tube, flange, and window from the laminar simulation including the DO model. In the first image, the cold boundary layer just inside the sapphire window found in all of the results from the UTSI furnace simulations is visible when using a reduced temperature scale. All red regions in the first image are $\geq$350 K. The full temperature profile is shown in the second image. Images taken from ParaView®.

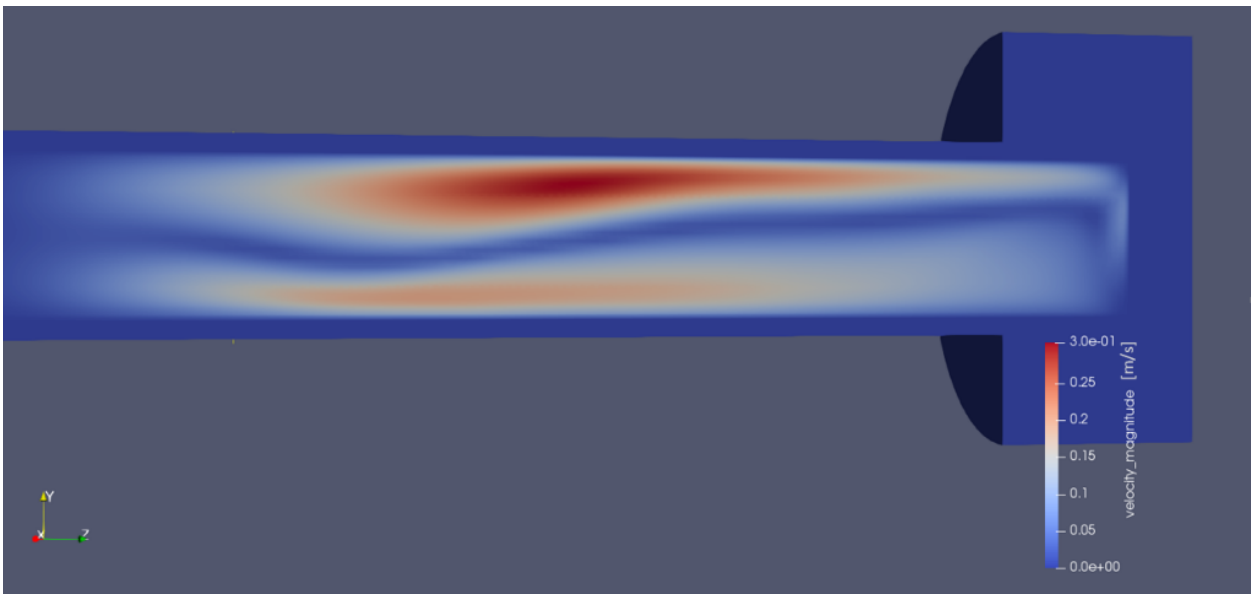

(a) Quartz tube, inner air, flange, and window velocity magnitude contour plot

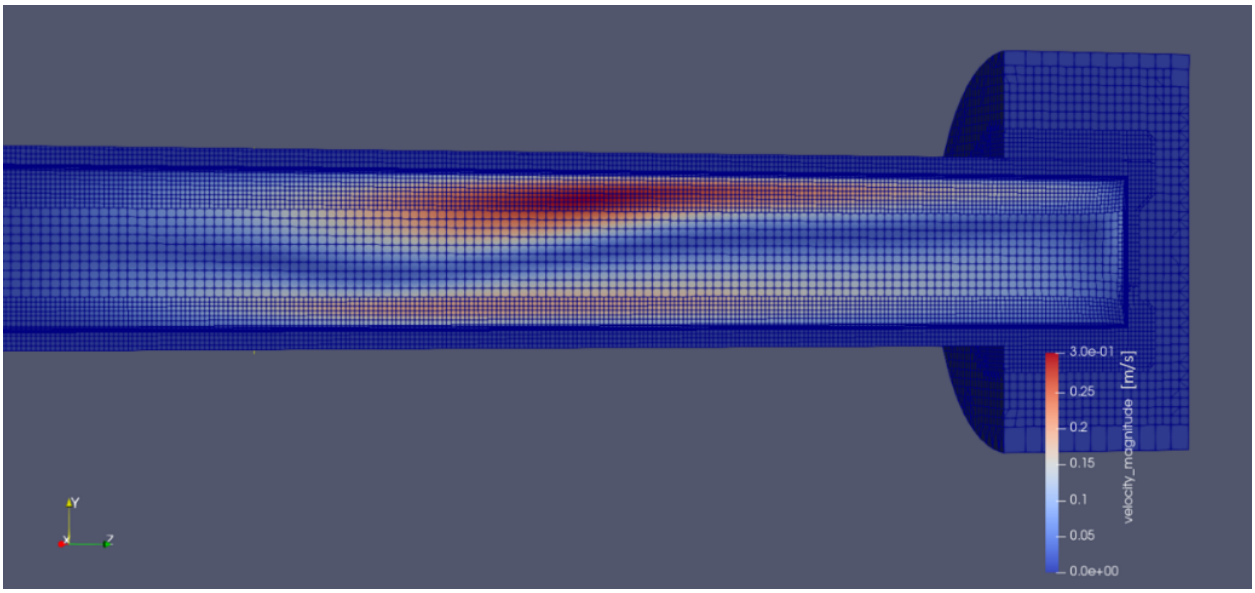

(b) Quartz tube, inner air, flange, and window velocity magnitude contour plot with mesh

Figure 3.25: Velocity magnitude contour plot from the UTSI cell simulation of the quartz cell, inner air, flange, and window from 0-0.3 m/s. Images taken from ParaView®.

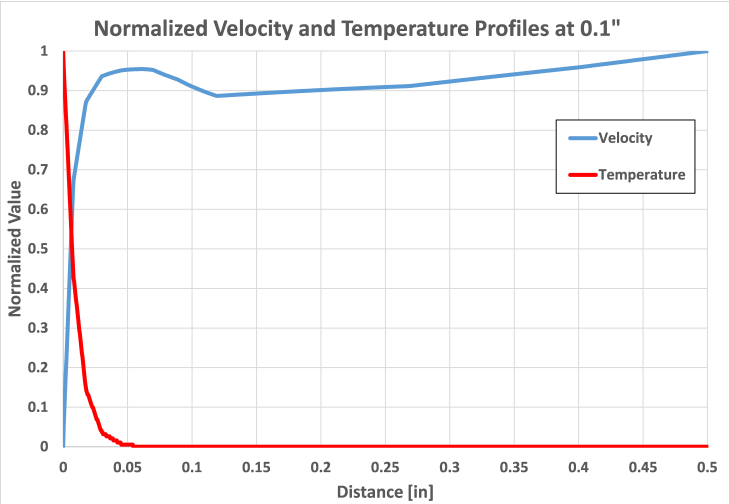

(a) Located at the top of flange, 0.1” from the outermost edge

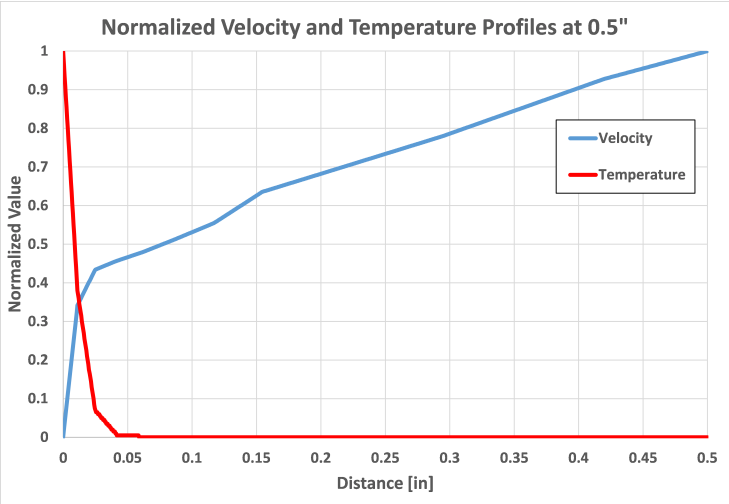

(b) Located at the top of flange, 0.5” from the outermost edge

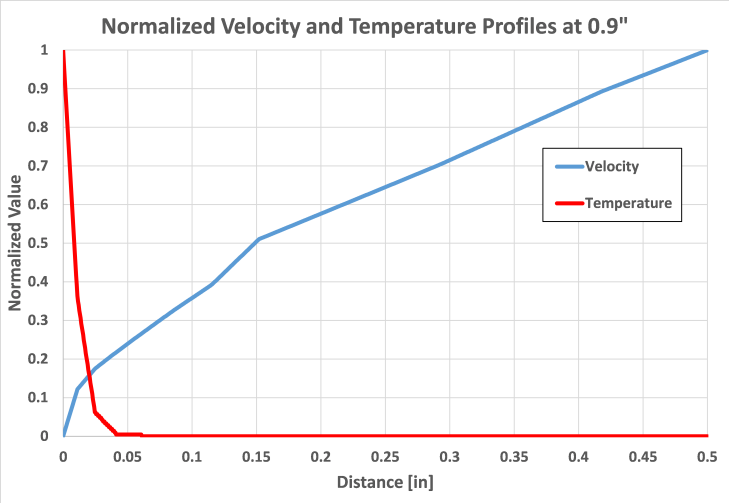

(c) Located at the top of flange, 0.9” from the outermost edge

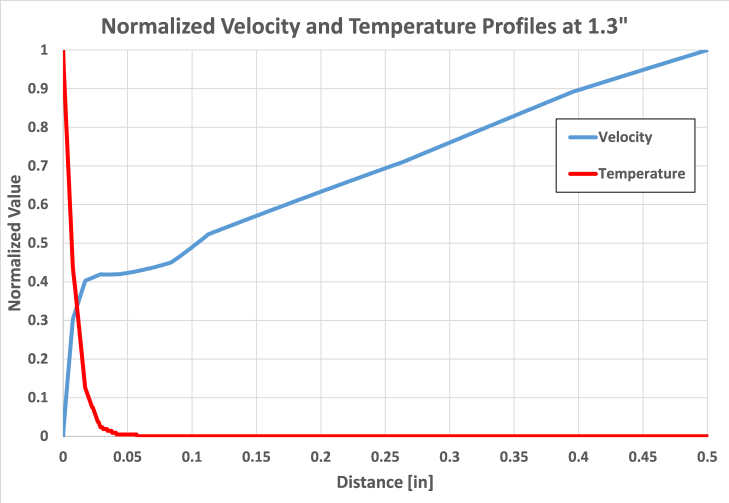

(d) Located at the top of flange, 1.3” from the outermost edge

Figure 3.26: Normalized profiles of velocity and temperature taken from the topmost surface of the flange to 0.5” above the surface. Velocity values are normalized by the value at 0.5” and temperature is normalized according to Equation 3.8.

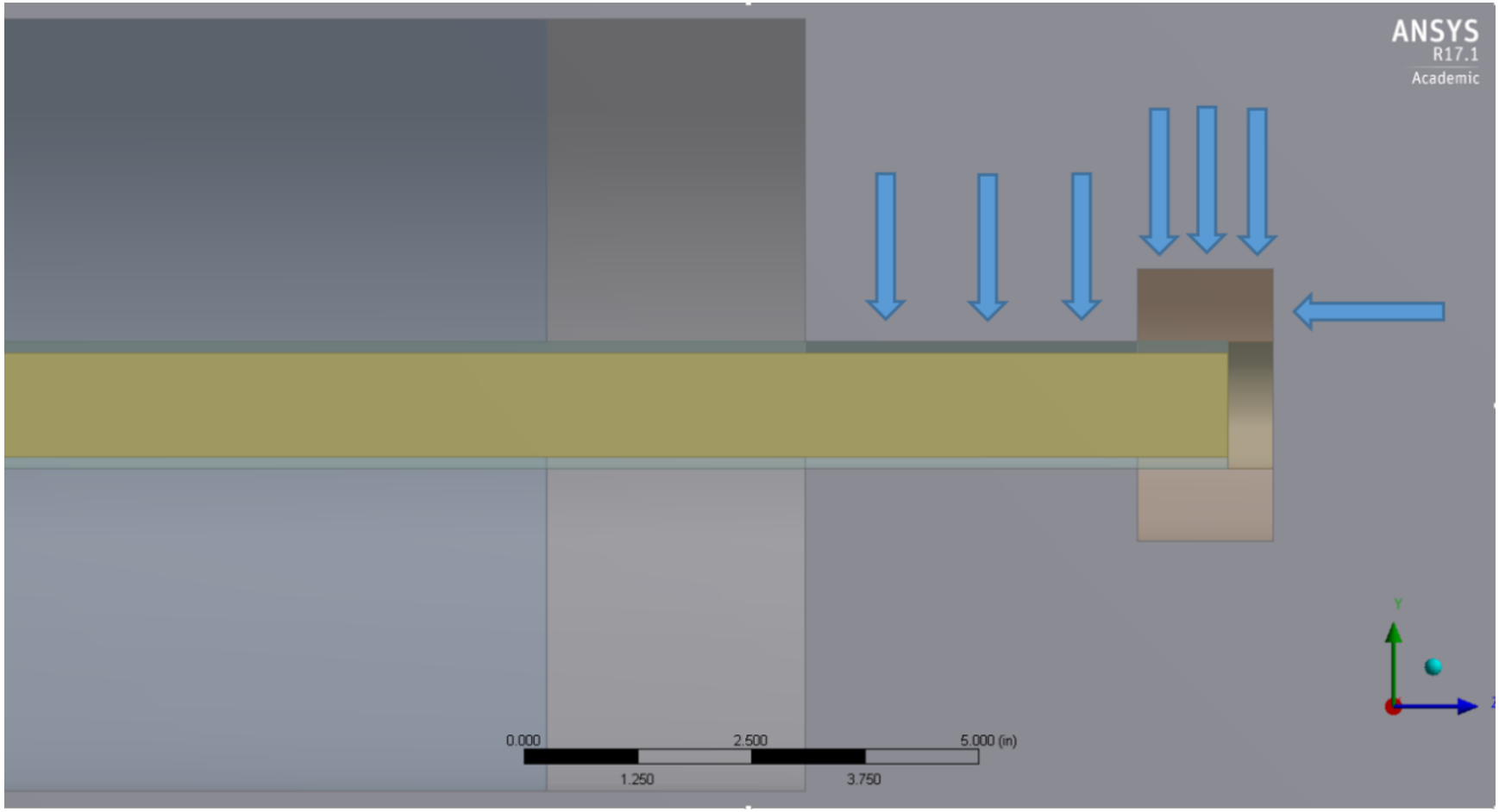

Figure 3.27: Model of the current UTSI cell and furnace in ANSYS® Academic Research Design Modeler, Release 17.1 using quarter symmetry and a simplified flange. The arrows reference the measured value "Top" locations found in Table 3.2. Images used courtesy of ANSYS®, Inc.

3.3.2 Model of 3-Zone Cell

The proposed cell follows the design of the cell built by Christiansen, et al. [12] with the exception of the flanges. In place of a water-cooled brass flange epoxied to the outer tube, a three-piece, stainless steel flange using an O-ring seal will be used. The same methods as that for the UTSI cell for meshing and modeling were used. The CFD model for this new configuration uses the single-zone furnace proposed in the design, which has a predicted uniform temperature region of approximately 10 inches given by the manufacturer, so 10 inches was used for the heated furnace section. The current design uses a 5.5 inch test section, but any size inner alumina tubes of a length that creates a test section fully enclosed by the uniform temperature section of the furnace will suffice. This particular test section length, which is smaller than the expected uniform region, was chosen to accommodate shifts in the uniformity that will occur during flowing tests. The model geometry is shown by Figure 3.28, and a portion from the mesh (1.55 mil nodes) is shown in Figure B.3 in Appendix B.

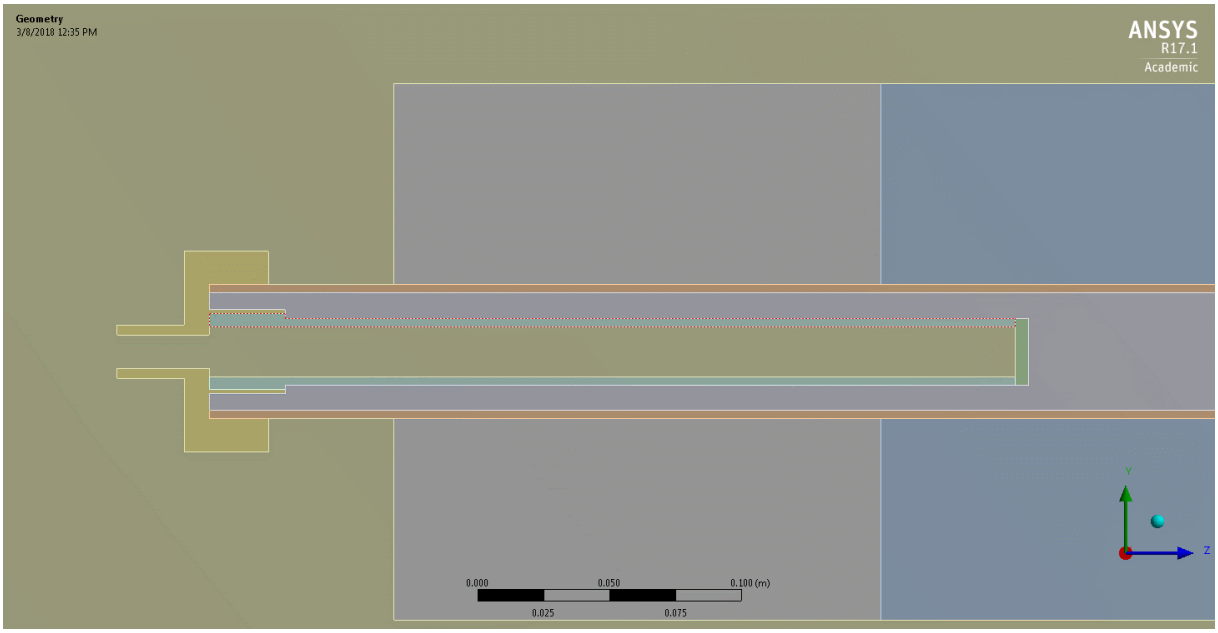

Figure 3.28: Quarter symmetry model for the proposed cell. This version includes the flange, inner tube, outer tube, sapphire window, two furnace sections, inner fluid, and outer fluid.

The flange was modeled as a single piece without O-rings and epoxied sections were treated as part of the inner alumina tube. The continual nitrogen flushing of the inner

tube was not included in this model, and the cell was treated as operating in static mode. All gases were again treated as air and the laminar model was used because, using the same assumptions as for the UTSI cell, the Rayleigh Number predicts a laminar flow regime (Equation 3.9).

$$\mathrm{Ra}_D = \frac{g\beta\Delta T D^3 \rho}{\mu\alpha} \approx \frac{(9.81)\left(\frac{1}{1773}\right)(1773-300)(0.0508^3)(0.1961)}{5.83\times10^{-5}\left(\frac{9.9\times10^{-5}}{0.1961\cdot1.233}\right)} = 1.5\times10^4 \tag{3.9}$$

The results for the centerline temperature found using this model are shown in Figure 3.29. These temperature gradients in the test section are small, with <4K gas gradient along the length of the 5.5 inch test section. The cell temperature distribution also closely resembles that of the previous furnace and cell simulation, with a uniform section for the proposed cell (single-zone furnace) of approximately 2/5 of the total furnace length as opposed to the 2/3 found when modeling the UTSI cell (three-zone furnace).

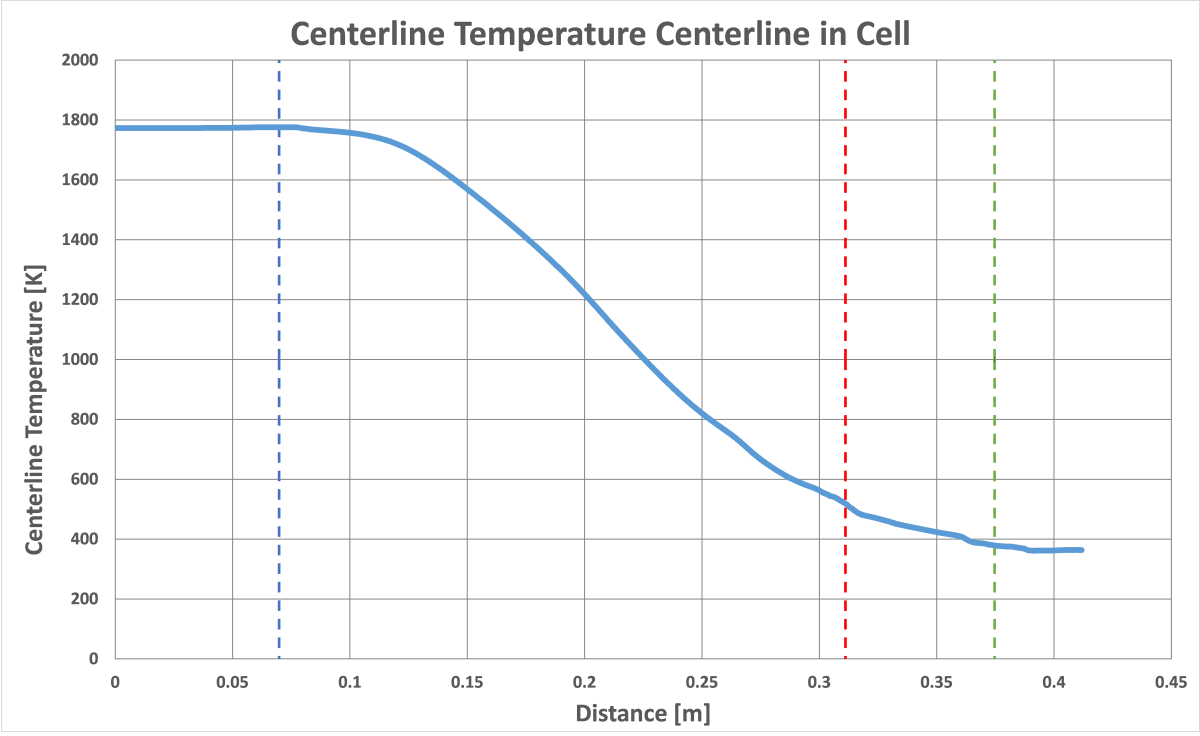

Figure 3.29: Axial temperature results from the laminar simulation. From left to right the colors indicate; the blue dotted line, the end of the test section; the red, the furnace opening; the green, the beginning of the flange. Distance is axial from the center of the furnace.

This simulation did not produce temperatures significantly higher than that of the temperature of the furnace, but the testing region temperature does overshoot the set temperature of the furnace slightly, which has been seen in previous models and amounts to a few kelvin higher (<4K) at the maximum in the window. There are some bumps in the temperature profile, most notably inside the sapphire window at the test section edge and around the region at the entrance to the furnace. Prior simulations using coarser meshes in that region, specifically in the inner tube at the edge of the furnace, produced flow instabilities (oscillating with time step) seen as bubbles with lower temperatures than the surrounding regions that were initially thought to be due to the onset of turbulence. A plot of the centerline temperature results taken from the 1.55 million node mesh shortly before divergence was detected in the Fluent® solver is shown in Figure 3.30. These instabilities were found to decrease in size as the mesh was refined along the centerline, particularly at the location of the bubble visible in the temperature contour plots shown in Figure 3.31. Adding cells resulted in a 1.67 mil node mesh, after which the laminar simulation converged like the UTSI simulations, and these are the results shown in Figure 3.29. Based on this discovery, increasing the nodal density past the level shown in these results would likely smooth the bumps at the window and outside the furnace out of the profile. In general, this mesh was not refined enough to remove all "blockiness", where jumps are seen at the interface between elements of the mesh, leading to the conclusion that a more refined mesh is required to verify that these results remain consistent. The convergence criterion was again the flange temperature, shown in Figure C.4 in Appendix C.

Another question about the new cell is the material capability of handling the higher temperatures, which is the primary reason for choosing to simulate this temperature first. While alumina, sapphire, and the epoxy bond are rated for temperatures above the 1773K setting of the furnace, the flanges are made of stainless steel with a maximum continuous operating temperature of below 1200K [40]. Additionally, the preferred material for the O-ring seals would be a high temperature nylon, such as Zytel® or Kalrez, which can be resealed more than once. These types of O-rings fail at temperatures before 600K. The temperature contours of the flange are shown in Figure 3.32. The temperature of every region stays well below 600K and only rises 100K higher than the current UTSI cell despite

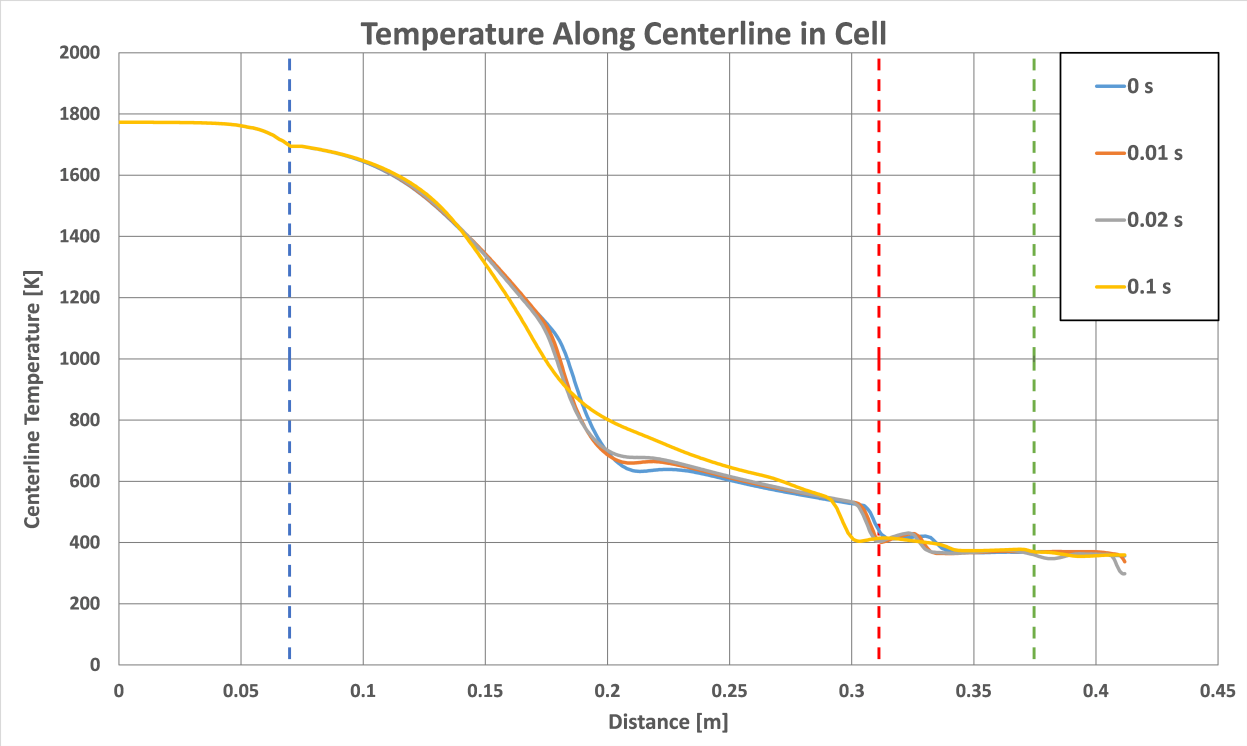

Figure 3.30: Axial temperature results from the 1.55mil node laminar simulation that exhibited unstable behavior over time. From left to right the colors indicate; the blue dotted line, the end of the test section; the red, the furnace opening; the green, the beginning of the flange. Distance is axial from the center of the furnace.

a 600K higher furnace temperature, likely due to the single-zone style furnace limiting the hottest temperatures to closer towards the center of the furnace than the current three-zone style furnace. Plots of temperature, pressure, and density contours from the 1.67 mil node mesh are shown in Figures 3.33, 3.34, and 3.35. Although there is a need for a more refined mesh to verify the consistency of these temperature results, the flange temperature remaining well below to 600K at this extreme temperature, much higher than the operating maximum temperature of the cell will be, is a promising indication that a water-cooling system will not be necessary.

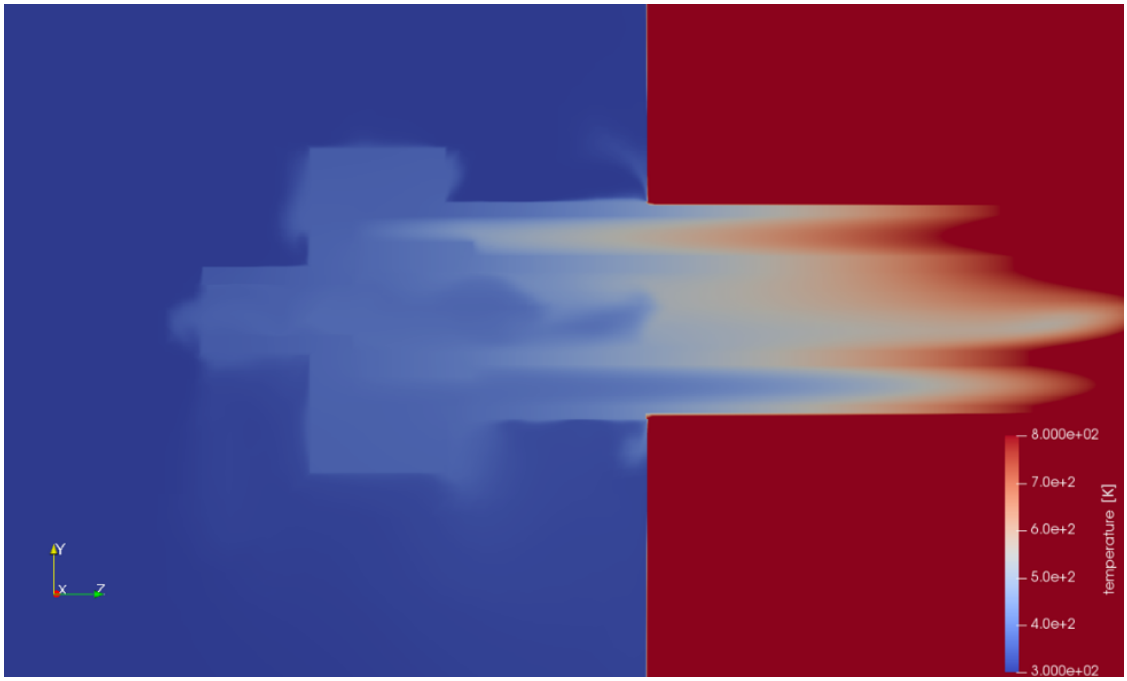

(a) Temperature contour plot from 300 - 800K

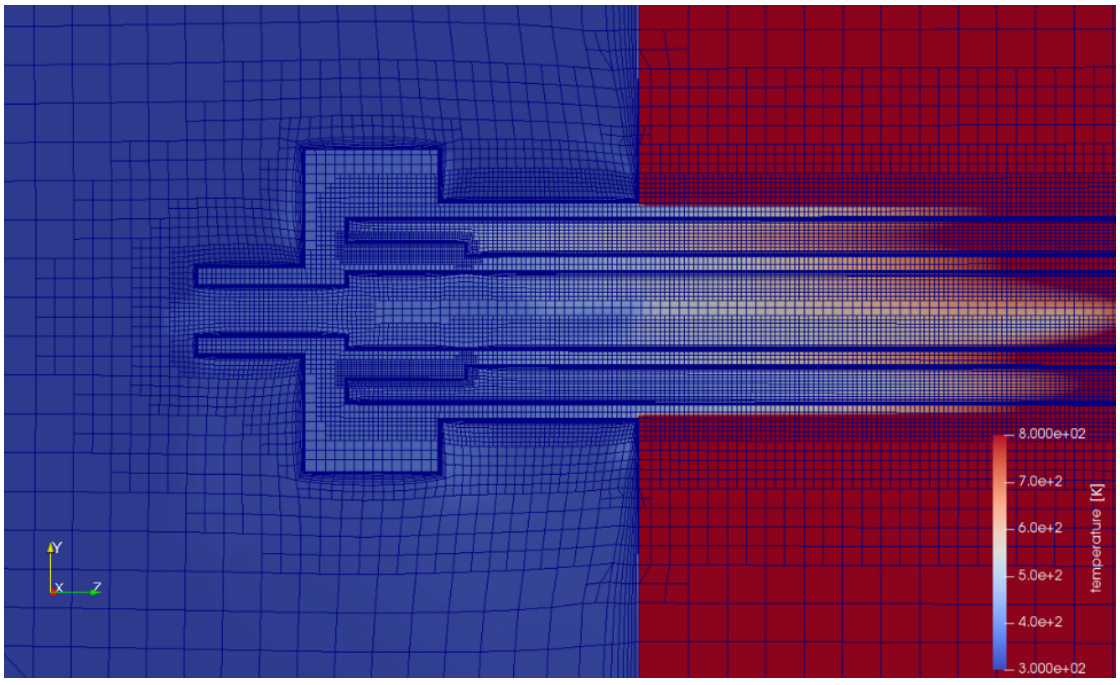

(b) Temperature contour plot from 300 - 800K with mesh overlay

Figure 3.31: Temperature contour plot from the laminar simulation with the 1.55 mil node mesh with a reduced temperature range for visibility (300 - 800K) before refinement along the centerline.

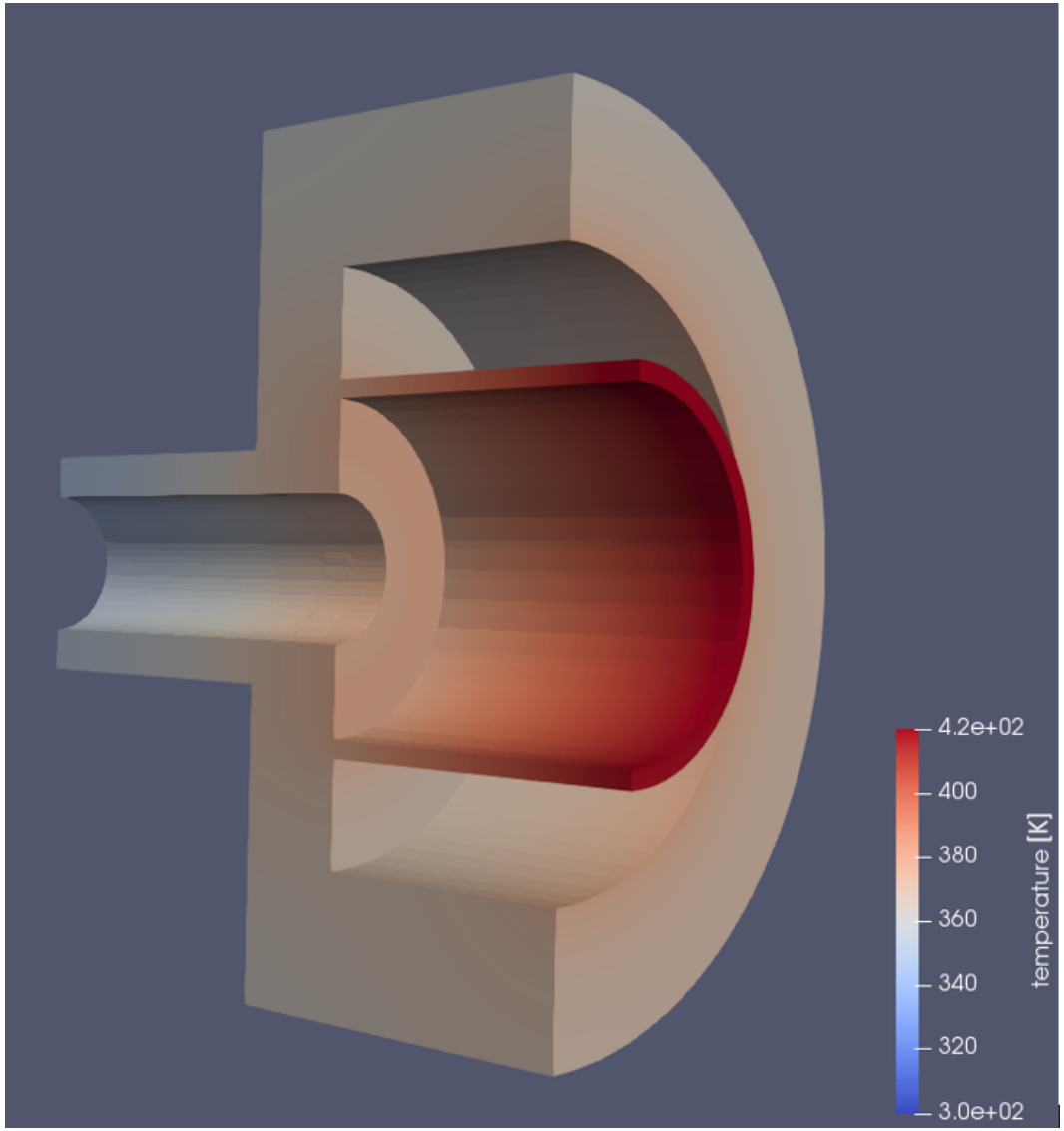

Figure 3.32: Flange temperature contour plot from 300 - 420K. Image taken from ParaView®.

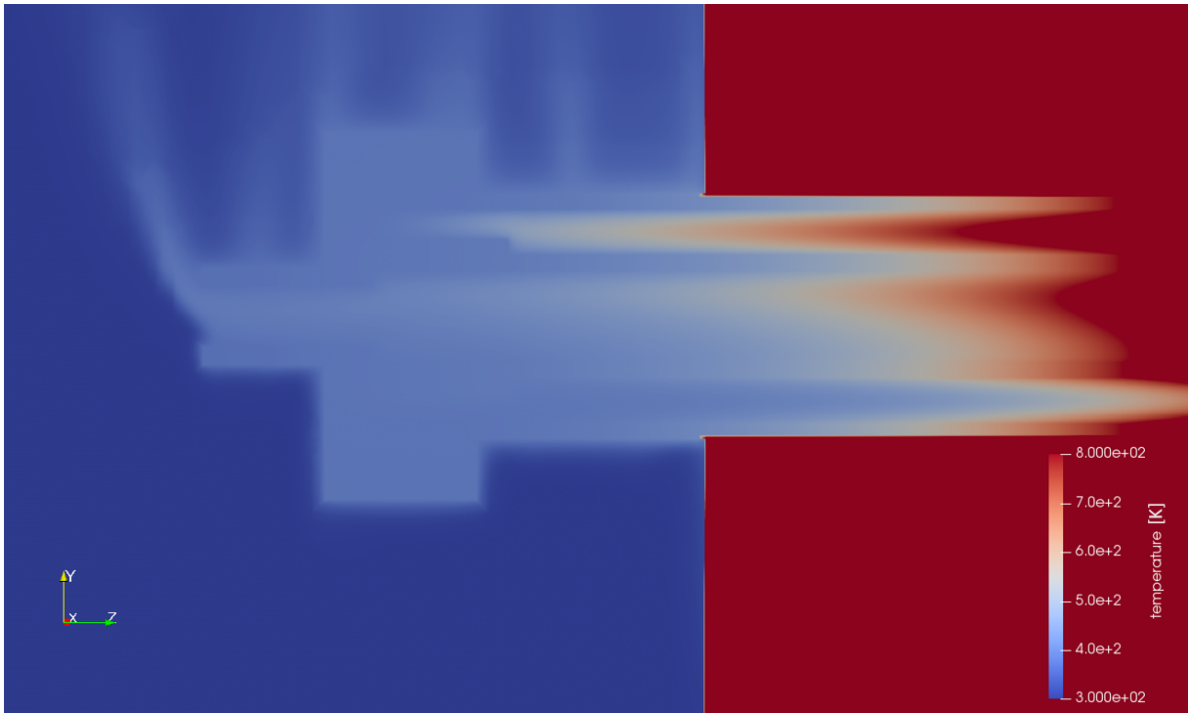

(a) Temperature contour plot from 300 - 800K from the 1.67 mil node mesh

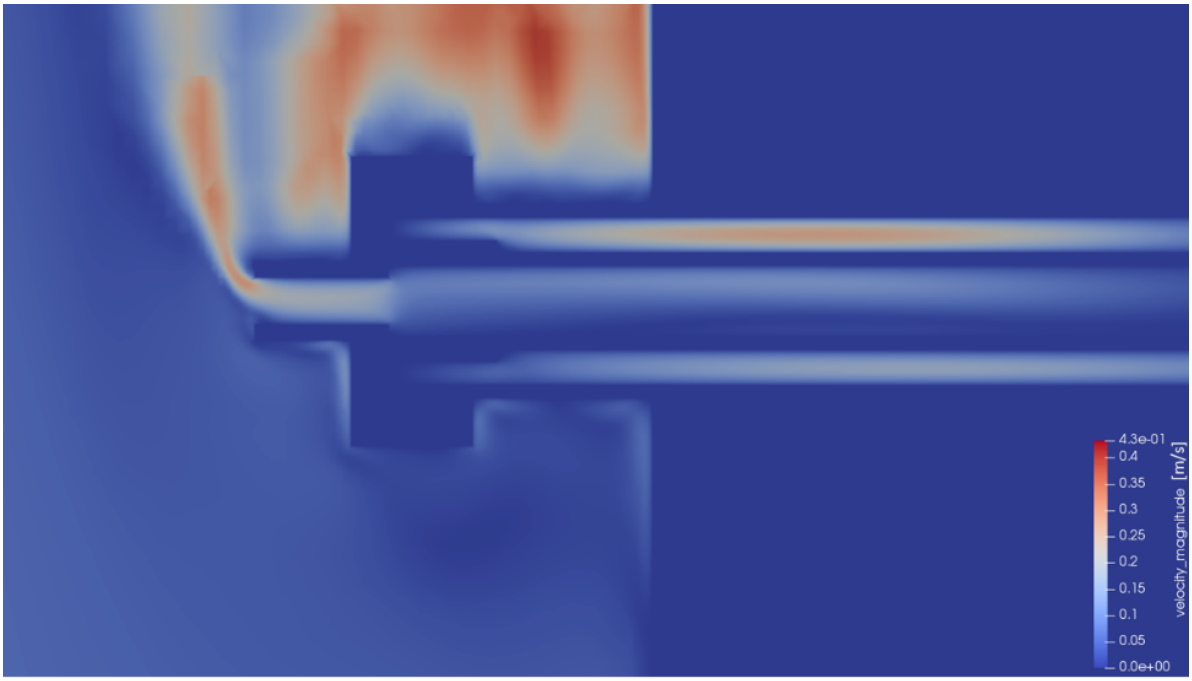

(b) Outer and inner air velocity contours in m/s from the 1.67 mil node mesh

Figure 3.33: The top image shows the temperature contour plot from the laminar simulation with the 1.67 mil node mesh with a reduced temperature range for visibility (300 - 800K) after refinement along the centerline. The bottom image shows the velocity contour plot for the inner and outer air from 0 - 0.43 m/s.

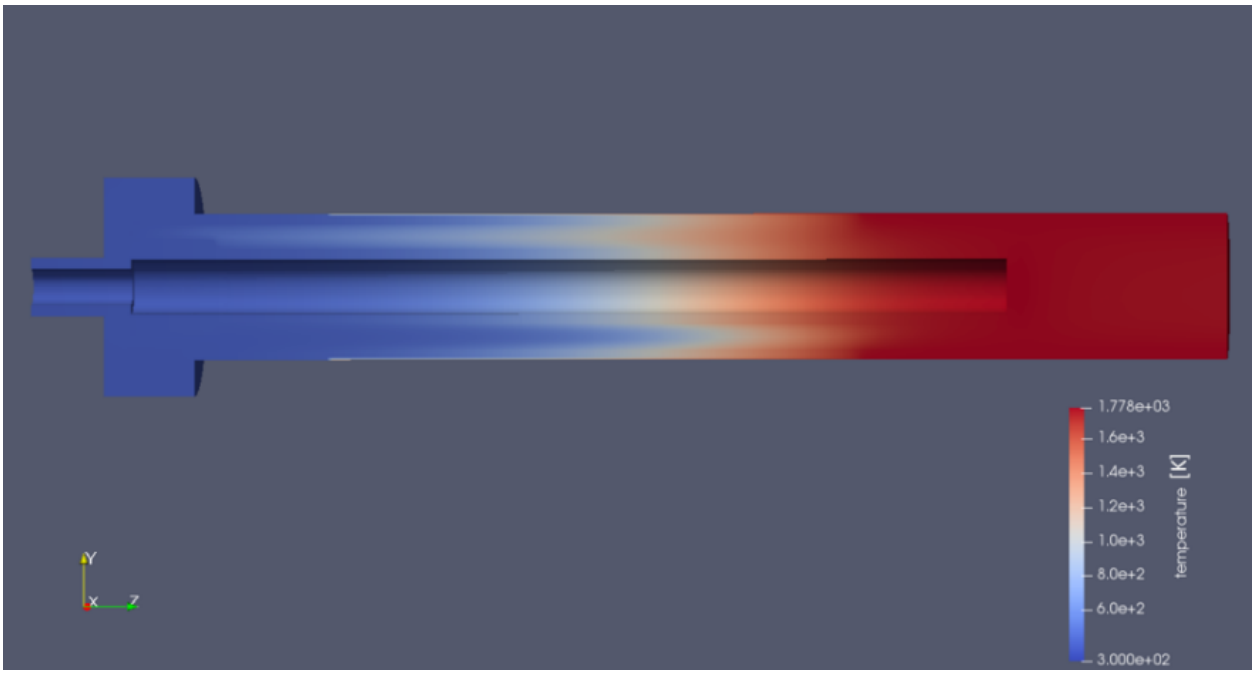

(a) Outer tube, inner tube, window, and inner air temperature contour plot from the 1.67 mil node mesh

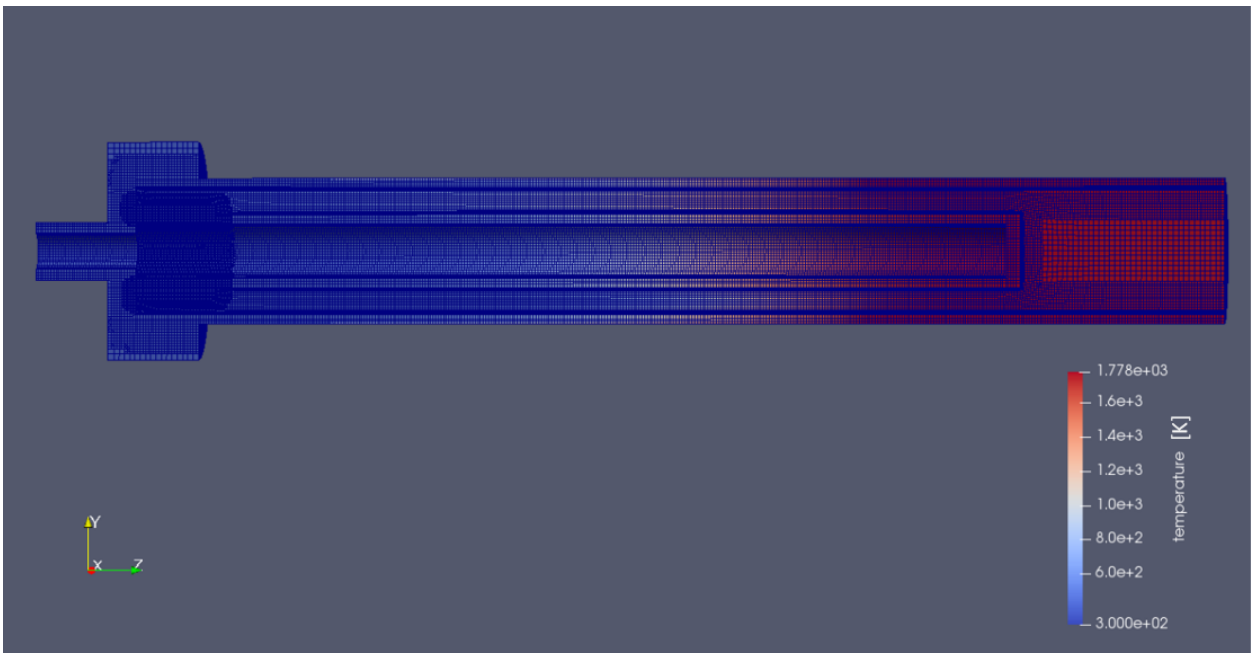

(b) Outer tube, inner tube, window, and inner air temperature contour plot with mesh overlay from the 1.67 mil node mesh

Figure 3.34: Temperature contour plot of the outer tube, inner tube, window, flange, and inner air blocks of the proposed cell from 300 - 1778K.

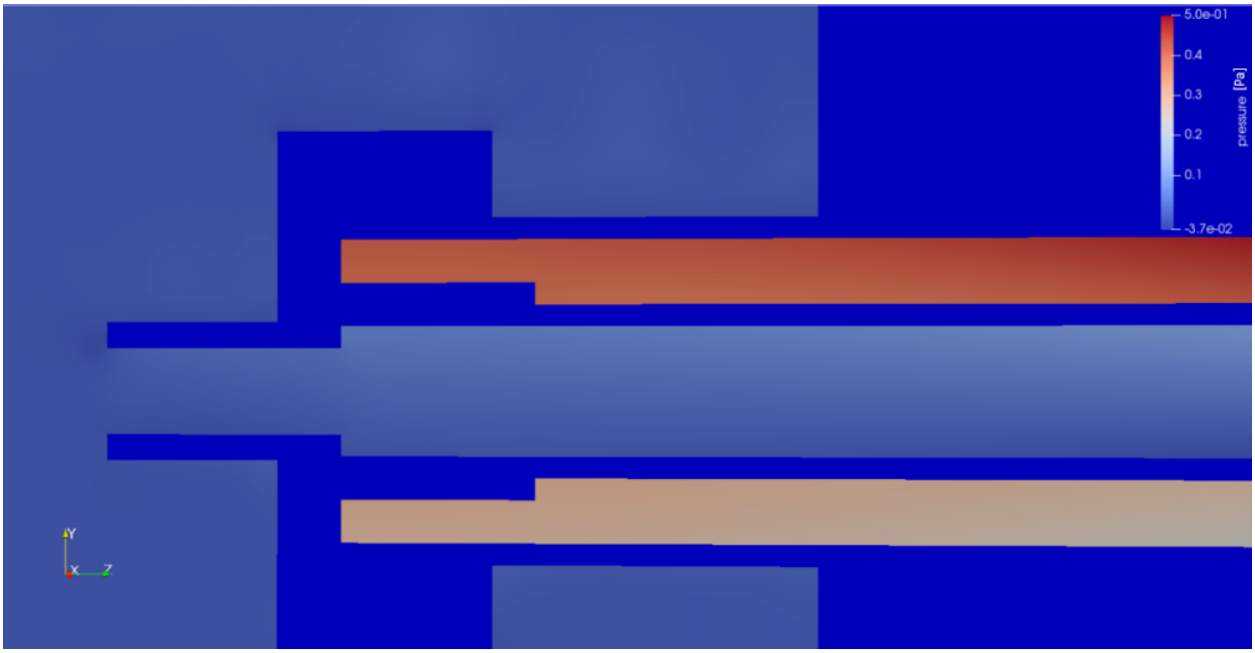

(a) Outer and inner air pressure contour plot in Pa from the 1.67 mil node mesh

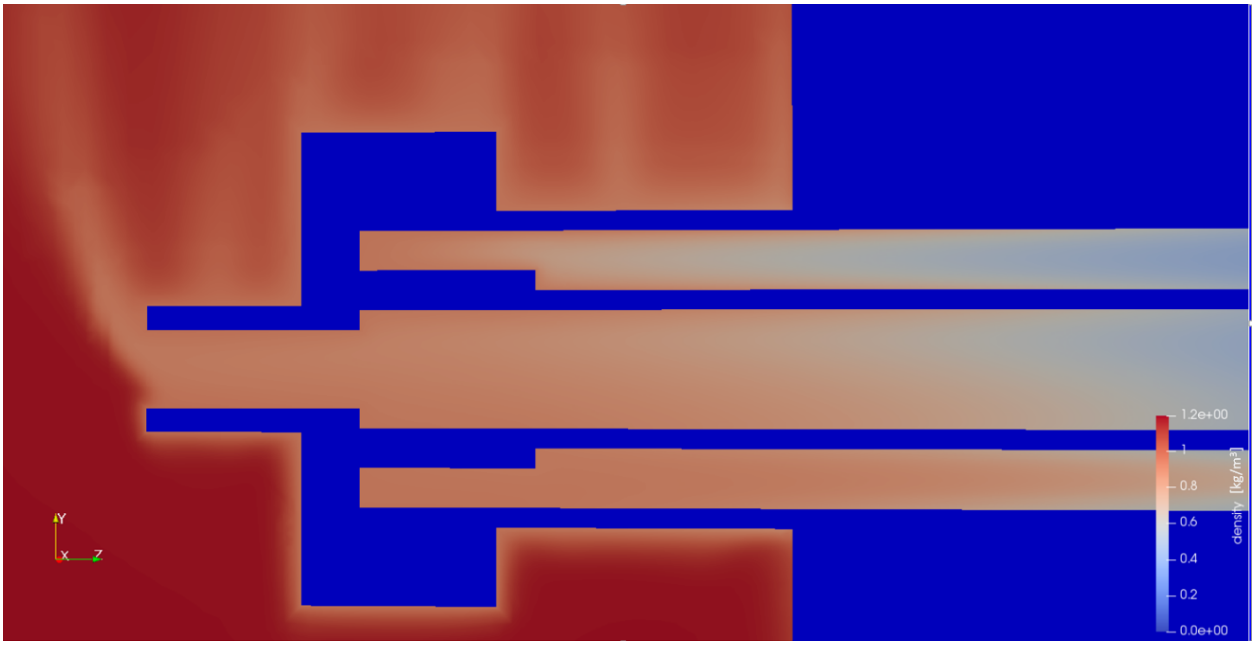

(b) Outer and inner air Density contour plot in kg/m^3 from the 1.67 mil node mesh

Figure 3.35: The top image shows the inner and outer air relative (to 101,325Pa) pressure contour plot from -0.037 - 0.43Pa. The bottom image shows inner and outer air density contour plot from 0.0 - 1.2 kg/m^3

Chapter 4

Conclusions

A solution for the large temperature gradients present in the University of Tennessee Space Institute (UTSI) gas cell has been shown. The three-zone gas cell design overcomes this issue by filling the gradients with a non-reacting gas, N_2, which allows one to make laser absorption measurements at the temperature of interest only. This creates a suitable calibration environment for laser absorption measurements to verify database values, such as those found in HITEMP, for temperatures up to 1773K, with the maximum operating temperature and wavelength regions dependent on the chosen window material. This provides a significant step closer to the estimated 2400K upper limit required to fully characterize most engine processes [12].

Computational Fluid dynamics (CFD) simulations were combined with an analytical model based on an energy balance of the K-Type thermocouple to provide an uncertainty estimate to encompass the true gas temperature. Simulations were then shown modeling the current UTSI furnace and cell to match centerline gas temperatures measured at a furnace setting of 1173K using the K-type thermocouple sheathed in alumina and surface measurements on the flange and cylinder made using a K-type thermocouple. The centerline gas temperatures using the laminar model was found to be in good agreement with those measured centerline values, with each point having a difference of between 4.0 and 46.2K. The modeled flange temperatures were found to be too low, and the measured cylinder and flange temperatures differed from the laminar simulations by between 9.4 and 20.4K, which translates to a 2.40 - 5.83% difference. Varying the geometry of the flange, the

window and flange material properties, and radiation properties failed to significantly alter the temperatures simulated for the flange. Four points were chosen along the top of the flange and the normalized velocity and temperature profiles showed that the resolution of the inflation layers was insufficient to create smooth curves, signifying the need for increased resolution, and a higher density of cells surrounding the flange may affect the temperature in that block. It is also possible that that the complexity of this model and knowledge of the author may be the reason for this discrepancy, caused by incorrect settings, oversimplification of the geometry using quarter-plane symmetry, or CFD considerations. ANSYS® Academic Research Fluent, Release 17.1 is often used for solutions for fluids, so it could also be that the a model of this complexity may limit the accuracy of the overall solution, due to either solver limitations or having to limit the resolution to reduce computational time.

This CFD modeling technique was then applied to the proposed three-zone cell and single-zone furnace to make a prediction of the centerline gas temperatures and the temperature of the flange with a furnace setting of 1773K, the maximum temperature of the furnace. A temperature distribution was taken from this simulation shows that the 5.5 inch test section displays high degree of temperature uniformity in line with the manufacturer's specifications and with gradients of <4K that are only slightly larger than the 3K gradients measured by Christiansen, et al. at 1000K and 101 bar in a cell of a similar design. The flange temperatures found in the same simulation were well below both the 1200K limit for stainless and the 600K limit for the preferred O-ring material, which is an indication that water-cooling will be unnecessary when using a single-zone furnace. Given these simulation results and results presented by Christiansen, et al. it is the author's opinion that the 3-zone high-temperature gas cell will produce a uniform temperature in the test gas section and that the flange temperature will stay below the maximum temperature, 600K, of the preferred O-ring material. These early results show that this design is an effective and simple way to overcome the temperature gradient problem present in the current UTSI cell and will provide a better calibration source than the current UTSI cell for laser absorption spectroscopy measurements in the mid infrared.

4.1 Future Work

On the thermocouple measurements, more work needs to be done for both the centerline gas temperature measurements and surface temperature measurements. For the centerline temperature profile, the most reasonable approach would be using multiple thermocouples with different sized beads to get an estimate for the gas temperature or, if necessary, the full length version of the thermocouple model shown here may meshed directly into the UTSI cell simulations, given how reasonably the results for the simple (1") resulted after applying the Richardson Extrapolation Technique. This would require several days to compute for each point, and the same analysis used in this work could be extended to that model, with the exception of an appropriate wall temperature choice based on the quartz cell temperature at the bead location. The surface temperature measurements should also be done with thermocouples of varying size or with the use of a thermocouple designed for surface temperature measurements.

As a continuation of the simulation work shown here, a more refined mesh for the proposed cell is necessary to verify that the temperature profile and flange temperatures remain consistent. Also, the case of flowing the test gas in the proposed three-zone cell is of particular interest to this research to determine a maximum flow rate that maintains the uniformity of the temperature distribution. This will provide a suitable range for mass flow controller specifications. This extension will require giving up one half plane of symmetry, because the axial flowing condition will nullify the symmetry boundary perpendicular to the length of the cell. However, the approximation using a symmetry plane parallel to the length of the cell and gravity should hold for the same reasons as before.

On the experimental side of the design, two important factors must be judged before the three-zone cell can be fully assembled; first, the sealing capability relative to temperature of the high-temperature epoxy that forms a bond between the alumina inner tube and sapphire/spinel window and the alumina inner tube and flange; second, the transmission capability of the chosen window material must be verified, preferably with a broad scanning laser capable of probing frequencies close to 5μm, to establish a temperature-dependent wavelength range accessible for study.

Bibliography

[1] K. M. Busa, *Development of a Tunable Diode Laser Application Tomography and Allication to Scramjet Engines*. PhD thesis, 2014. 1, 4, 5, 6, 7, 8

[2] F. K. Tittel, D. Richter, and A. Fried, *Solid-State Mid-Infrared Sources*. Topics in Applied Physics, Springer, 2003. 1

[3] S. B. Twiss, D. Teague, J. Bozek, and M. Sink, "Application of infrared spectroscopy to exhaust gas analysis," *Journal of the Air Pollution Control Association*, vol. 5, pp. 75–83, 1955. 1, 2, 3, 4

[4] L. Rothman, I. Gordon, R. Barber, H. Dothe, R. Gamache, A. Goldman, V. Perevalov, S. Tashkun, and J. Tennyson, "HITEMP, the high-temperature molecular spectroscopic database," *Journal of Quantitative Spectroscopy & Radiative Transfer*, vol. 111, pp. 2139–2150, 2010. 1, 7, 10

[5] L. S. Rothman, I. E. Gordon, Y. Babikov, A. Barbe, D. C. Benner, P. F. Bernath, M. Birk, L. Bizzocchi, V. Boudon, L. R. Brown, *et al.*, "The HITRAN2012 molecular spectroscopic database," *Journal of Quantitative Spectroscopy and Radiative Transfer*, vol. 130, pp. 4–50, 2013. 1, 7, 10

[6] X. Liu, J. Jeffries, R. Hanson, K. Hinckley, and Woon, "Development of a tunable diode laser sensor for measurements of gas turbine exhaust temperature," *Applied Physics B: Laser and Optics*, vol. 82, pp. 469–478, 2006. 1, 2, 6, 7, 8, 10, 11, 12, 24

[7] R. Spearrin, W. Ren, J. Jeffries, and B. Hanson, "Multi-band infrared CO_2 absorption sensor for sensitive temperature and species measurements in high-temperature gases," *Applied Physics B: Laser and Optics*, 2014. 1, 2, 3, 6, 7, 8, 10

[8] S. T. Sanders, J. Wang, J. B. Jeffries, and R. K. Hanson, "Diode-laser absorption sensor for line-of-sight gas temperature distributions," *Applied Optics*, vol. 40, 2001. 1, 2, 6, 7, 8, 9, 11

[9] J. T. C. Liu, G. B. Rieker, J. B. Jeffries, M. R. Gruber, C. D. Carter, T. Mathur, and R. K. Hanson, "Near-infrared diode laser absorption disgnostic for temperature and water vapor in a scramjet combustor," *Applied Optics*, vol. 44, 2005. 1, 6, 7, 8, 24

[10] A. Klingbeil, J. Jeffries, and R. Hanson, "Temperature-dependent mid-IR absorption spectra of gaseous hydrocarbons," *J. Quant. Spectrosc. Radiat. Transfer*, vol. 107, pp. 407–420, 2007. 1, 6, 10, 24

[11] D. Lisak and J. Hodges, "Comparison between theoretical calculations and high-resolution measurements of pressure broadening for near-infrared water spectra," *Journal of Molecular Spectroscopy*, vol. 249, 2008. 1, 2, 6

[12] C. Christiansen, T. Stolberg-Rohr, and A. Fateev, "High temperature and high pressure gas cell for quantitative spectroscopic measurements," *J. Quant. Spectrosc. Radiat. Transfer*, vol. 169, pp. 96–103, 2016. 2, 10, 11, 12, 23, 24, 25, 51, 60

[13] J. A. Nwaboh, O. Werhahn, and D. Schiel, "Measurement of CO amount fractions using a pulsed quantum-cascade laser operated in the intrapulse mode," *Applied Physics B*, vol. 103, pp. 947–957, 2011. 2, 3

[14] H. Grosch, A. Fateev, K. L. Nielson, and S. Clausen, "Hot gas flow cell for optical measurements on reactive gases," *J. Quant. Spectrosc. Radiat. Transfer*, vol. 130, pp. 392–399, 2013. 2, 11, 24

[15] V. Evseev, A. Fateev, and S. Clausen, "High-resolution transmission measurements of CO_2 at high temperatures for industrial applications," *J. Quant. Spectrosc. Radiat. Transfer*, vol. 130, pp. 392–399, 2013. 2, 3, 24

[16] D. Heard, A. Fried, and D. Richter, *Analytical techniques for Atmospheric Measurement*. Blackwell Publishing, 2006. 3, 4

[17] Y. Yao, A. J. Hoffman, and C. F. Gmachl, "mid-infrared quantum cascade lasers," *nature photonics*, vol. 6, 2012. 3

[18] I. N. Levine, *Quantum Chemistry, Vol. 1.* II: Molecular Spectroscopy, Atlyn and Bacon, 1970. 4

[19] J. T. Reilly, J. M. Walsh, M. L. Greenfield, and M. D. Donohue, "Analysis of FT-IR spectroscopic data: the voigt profile," *Spectrochimica Acta*, vol. 48A, pp. 1459–1479, 1992. 4, 5

[20] J. Tennyson, P. Bernath, A. Campargue, A. Csaszar, L. Daumont, R. Gamache, J. Hodges, D. Lisak, O. Naumenko, L. Rothman, H. Tran, N. Zobov, J. Buldyreva, C. Bosne, M. Domenica De Vizia, L. Gianfrani, J. Hartmann, R. McPheat, J. Murray, N. Hoa Ngo, O. Polyansky, and D. Weidmann, "Recommended isolated-line profile for representing high-resolution spectroscopic transitions (IUPAC technical report)," *ArXiv e-prints*, 2014. 4, 5, 6

[21] Z. Shippony and W. Read, "A highly accurate voigt function algorithm," *J. Quant. Spectrosc. Radiat. Transfer*, vol. 50, pp. 635–646, 1993. 6

[22] J. Humlicek, "Optimized computation of the voigt and complex probability functions," *J. Quant. Spectrosc. Radiat. Transfer*, vol. 27, pp. 437–444, 1982. 6

[23] J. A. Nwaboh, O. Werhahn, D. Schiel, P. Ortwein, and V. Ebert, "Laser-spectrometric gas analysis: CO2TDLAS at 2 m," *measurement science and techology*, vol. 24, 2013. 6

[24] R. Gamache, R. Hawkins, and L. Rothman, "Total internal partition sums in the temperature range 70-3000 k: Atmospheric linear molecules," *Journal of Molecular Spectroscopy*, vol. 142, pp. 205–219, 1990. 7

[25] N. P. Bansal and R. Doremus, *Handbook of glass properties*. Academic Press, Inc., 1986. 11, 41

[26] S. Krishnan, "An approach to thermocouple temperature measurements that reduces uncertainties associated with radiative corrections," Master's thesis, 2014. https://openscholarship.wustl.edu/cgi/viewcontent.cgi?referer=https://www.google.com/&httpsredir=1&article=1004&context=eng_etds, Accessed: 2018-4-12. 16

[27] S. D. Stephens, "Characterization of convective heat transfer coefficients of a self-aspirated hot gas temperature probe," Master's thesis, 2015. http://trace.tennessee.edu/cgi/viewcontent.cgi?article=4826&context=utk_gradthes, Accessed: 2018-4-12. 16

[28] ANSYS, Inc., *Academic Research Fluent, Release 17.1.* Help System, ANSYS, Inc., 2017. 18, 40, 41

[29] A. Neale, D. Derome, B. Blocken, and J. Carmeliet, "Determination of surface convective heat transfer coefficients by cfd," tech. rep., Concordia University, Technische Universiteit Eindhoven, and Katholieke Universiteit Leuven, 2007. https://www.kuleuven.be/bwf/projects/annex41/protected/data/CON%20Apr%202006%20Paper%20A41-T3-C-06-5.pdf, Accessed: 2018-4-11. 19

[30] J. H. Ferziger and M. Peric, *Computational Methods for Fluid Dynamics 3rd Revision.* Springer, 1997. 19

[31] ThorLabs, Inc., "Total transmission of 5mm thick, uncoated sapphire window," 2017. https://www.thorlabs.com/NewGroupPage9.cfm?ObjectGroup_ID=3982, Accessed: 2018-2-15. 23

[32] M. Alberti, R. Weber, M. Mancini, A. Fateev, and S. Clausen, "High-resolution transmission measurements of CO_2 at high temperatures for industrial applications," *J. Quant. Spectrosc. Radiat. Transfer*, vol. 130, pp. 392–399, 2013. 24

[33] E. R. Dobrovinskaya, L. A. Lytvynov, and V. Pishchik, *Sapphire: Material, Manufacturing, Applications.* Micro- and Opto-Electronic Materials, Structures, and Systems, Springer, 2009. 25, 41

[34] P. Auerkari, "Mechanical and physical properties of engineering alumina ceramics," tech. rep., Technical Research Centre of Finland, 1996. http://www.vtt.fi/inf/pdf/tiedotteet/1996/T1792.pdf, Accessed: 2018-3-8. 25, 41

[35] Mellen Company, "Ts tube furnace," 2017. http://www.mellencompany.com/furnaces/research-tube-furnaces, Accessed: 2018-4-6. 37

[36] Ansys, Inc., "Modeling turbulent flows : Introductory FLUENT training," 2017. http://www.southampton.ac.uk/~nwb/lectures/GoodPracticeCFD/Articles/Turbulence_Notes_Fluent-v6.3.06.pdf, Accessed: 2018-2-26. 39, 40, 41, 42

[37] J. Ahrens, B. Geveci, and C. Law, *ParaView: An End-User Tool for Large Data Visualization*. Visualization Handbook, Elsevier, 2005. 39

[38] D. R. Heldman, *Encyclopedia of agricultural, food, and biological engineering*. Marcel Dekker, Inc., 2003. 40, 41

[39] ANSYS, Inc., "ANSYS solver settings: Introductory fluent training," 2006. http://www.engr.uconn.edu/~barbertj/CFD%20Training/Fluent/4%20Solver%20Settings.pdf, Accessed: 2018-4-16. 40

[40] Azo Materials, "Stainless steel - grade 304 (UNS S30400)," 2017. https://www.azom.com/properties.aspx?ArticleID=965, Accessed: 2018-2-15. 41, 53

[41] DuPont Fluorproducts, "Teflon PTFE fluoropolymer resin," tech. rep., DuPont Fluorproducts, 1997. http://www.rjchase.com/ptfe_handbook.pdf, Accessed: 2018-3-14. 41

[42] Special Metals Corporation, "Inconel alloy 600," 2011. http://www.specialmetals.com/assets/smc/documents/alloys/inconel/inconel-alloy-600.pdf, Accessed: 2018-4-6. 41

Appendices

Appendix A

Simulation Settings

Table A.1: Material Properties used in simulations.

Material	Property	Temperature [K]	Value
Dry Air	Thermal Cond. [W/mK]	300	0.026
		400	0.034
		500	0.040
		600	0.047
		700	0.052
		800	0.058
		900	0.063
		1000	0.068
		1100	0.072
		1200	0.076
		1300	0.081
		1400	0.085
		1500	0.088
		1600	0.092
		1700	0.096
		1800	0.102

Continued on next page

Table A.1 – continued from previous page

Material	Property	Temperature [K]	Value
Fused Quartz	Abs. Coeff. [1/m]	300	0.2
	Thermal Cond. [W/mK]	300	1.3
		400	1.5
		500	1.7
		600	1.7
		700	1.9
		800	2.2
		900	2.5
		1000	2.8
		1100	3.3
		1200	4.0
	Abs. Coeff. [1/m]	300	200
	Index of Refraction	300	1.5
	Density [kg/m^3]	300	2601
SS 304	Thermal Cond. [W/mK]	300	15.5
	Density [kg/m^3]	300	7960
Alumina 99.5%	Thermal Cond. [W/mK]	300	28
		400	25
		500	20
		600	15
		700	11
		800	10
		900	9
		1000	8
		1100	7
		1200	6
		1300	6

Continued on next page

Table A.1 – continued from previous page

Material	Property	Temperature [K]	Value
	Density [kg/m^3]	300	3890
Sapphire	Thermal Cond. [W/mK]	298	31.4
		670	12.56
		1500	4
	Abs. Coeff. [1/m]	300	117
		1700	1100
	Index of Refraction	1773	1.675
	Density [kg/m^3]	300	3980
Teflon (PTFE)	Thermal Cond. [W/mK]	300	0.25
	Density [kg/m^3]	300	2160
Inconel-600	Thermal Cond. [W/mK]	1073	27.5
	Density [kg/m^3]	300	8470

Appendix B

Simulation Meshes

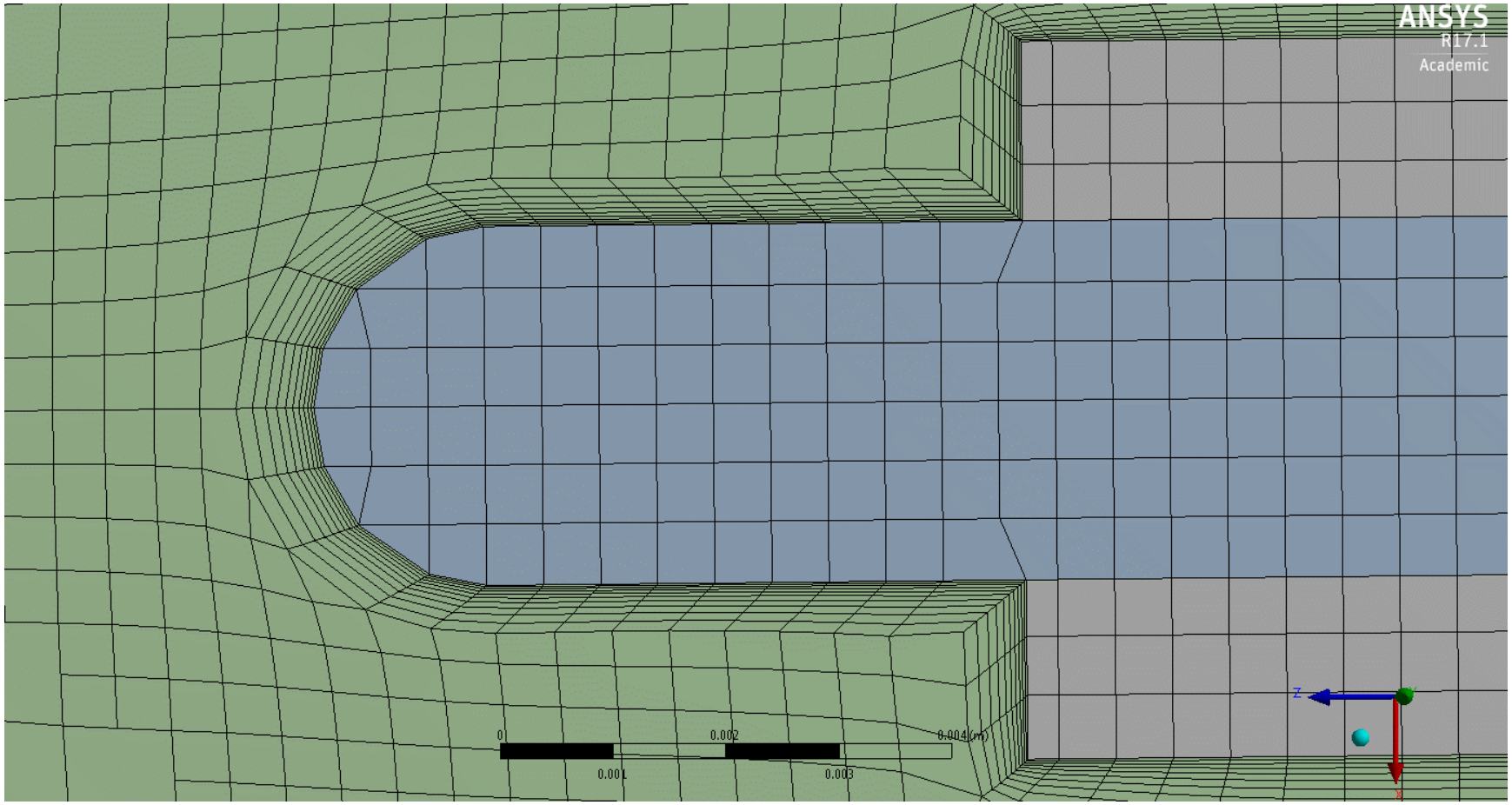

Figure B.1: Portion of the cut-cell style mesh used to model the "middle" thermocouple simulations. Image taken from ANSYS® Mesh.

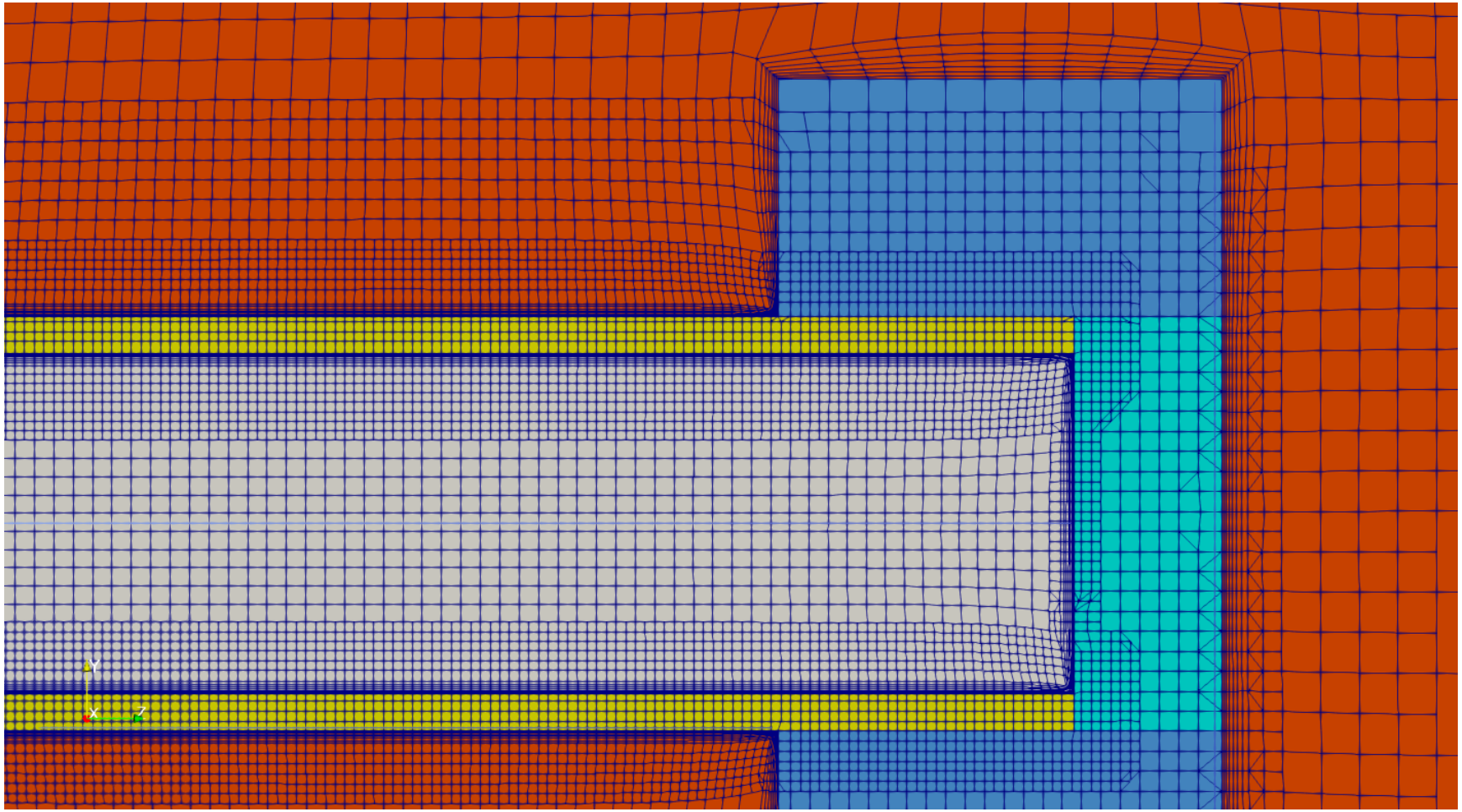

Figure B.2: Portion of the cut-cell style mesh used to model the current UTSI furnace operating in static condition. The colors indicate separate blocks. Shown are the flange (blue), window (teal), quartz tube (yellow), inner air (white), and outer air (orange). Visible along the centerline is the line indicating the cells used for reported temperatures. Image taken from ParaView®.

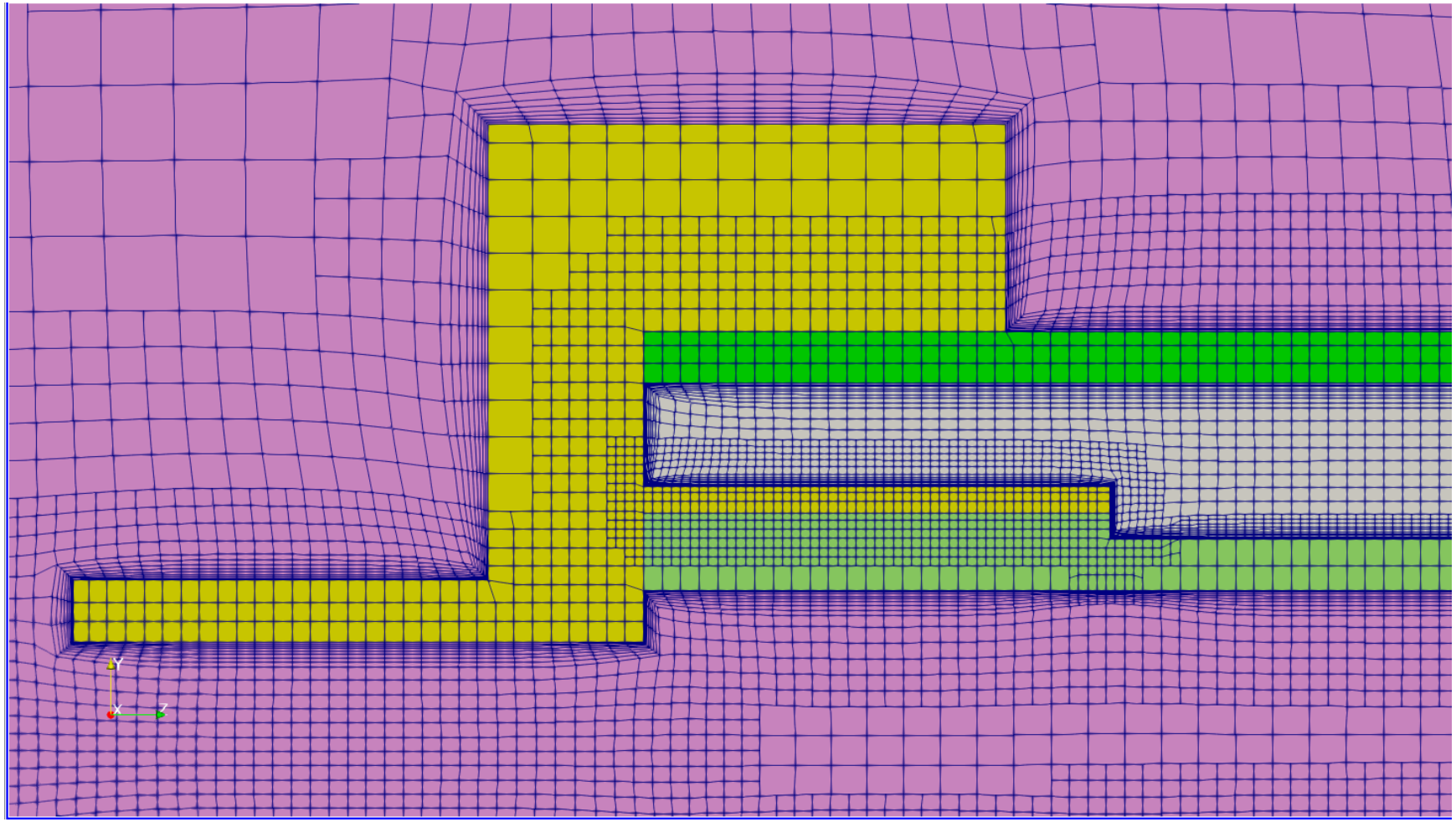

Figure B.3: Portion of the cut-cell style mesh used to model the proposed cell. The colors indicate separate blocks. Shown are the flange (yellow), outer alumina tube (green), inner air (white), outer air (pink), and inner alumina tube (light green). This mesh is symmetric about the centerline. Image taken from ParaView®.

Appendix C

Miscellaneous

Table C.1: Uncertainty sources considered for the K-type thermocouple measurement. Not included is a term for any magnetic effects due to the heating coil, which have not been characterized. Smaller sources of uncertainty, such as the nonlinearity and offset error, were found to be negligible.

Source	Value [K] or [%]
Energy Losses	21.45
Type K	greater of 2.2K or 0.75% (in °C)
Reference Junction	0.5K
Calibration	0.55K
Gain Error	0.004%
Offset Error	600μV
Module Abs. Acc.	±[(Volt Reading x Gain Error)+(Volt Range x Offset Error)]

Table C.2: List of measured thermocouple values and the associated errors taken from Table C.1 taken at the furnace setting of 1173K with the K-Type thermocouple.

Location [in]	Bead Temp [K]	Neg. Unc. [K]	%	Pos. Unc. [K]	%
0.5	324.4	2.3	0.7	21.6	6.7
2.5	370.8	2.3	0.6	21.6	5.8
3.5	422.2	2.3	0.6	21.6	5.1
4.5	507.2	3.9	0.8	21.6	4.3
5.5	721.2	5.5	0.8	24.6	3.4
6.5	949.2	7.2	0.8	26.6	2.8
7.5	1085.2	8.2	0.8	28.0	2.6
8.5	1141.2	8.6	0.8	28.6	2.5
10.5	1160.9	8.7	0.8	28.8	2.5
12.5	1162.7	8.8	0.8	28.8	2.5
14.5	1162.7	8.8	0.8	28.8	2.5
16.5	1160.9	8.7	0.8	28.8	2.5
18.5	1141.2	8.6	0.8	28.6	2.5
19.5	1085.2	8.2	0.8	28.0	2.6
20.5	949.2	7.2	0.8	26.6	2.8
21.5	721.2	5.5	0.8	24.6	3.4
22.5	507.2	3.9	0.8	21.6	4.3
23.5	422.2	2.3	0.6	21.6	5.1
24.5	370.8	2.3	0.6	21.6	5.8
26.5	324.4	2.3	0.7	21.6	6.7

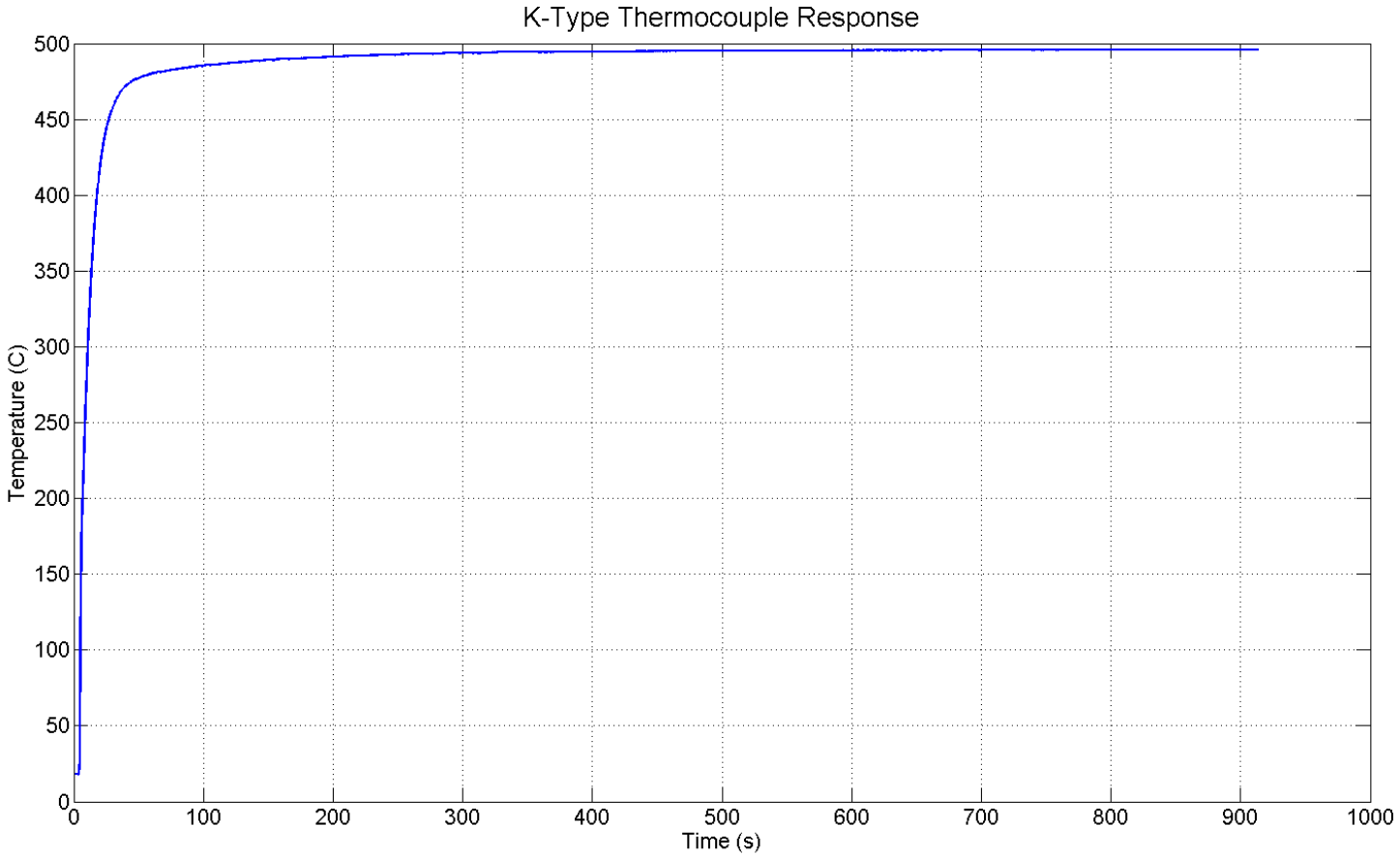

Figure C.1: K-Type thermocouple with alumina sheath time constant measurement made using the Carbolite® tube furnace set to 500°C using the same method of insertion as the temperature tests on the UTSI furnace. The thermocouple and sheath in this case were left sitting just inside the furnace until it had reached steady-state then slid in until the bead was in the center of the uniform region. The time constant was measured to be 17 s with the maximum value taken as the "true" value.

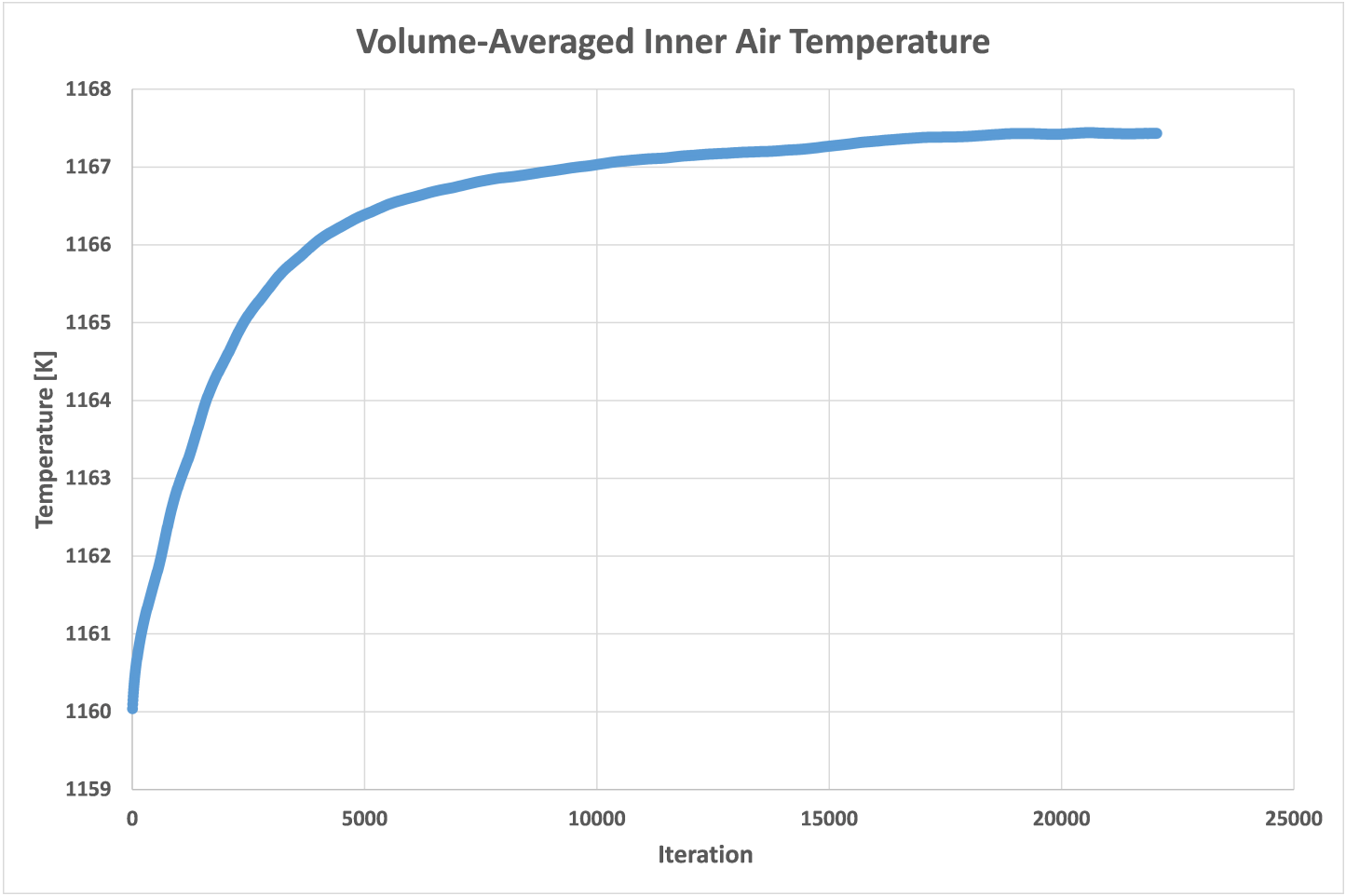

Figure C.2: Volume-averaged inner air static temperature relative to iteration for the steady-state, Boussinesq simulation of the thermocouple inside the furnace. This was used as a convergence criterion for this set of simulations, and this comes from the "middle" mesh.

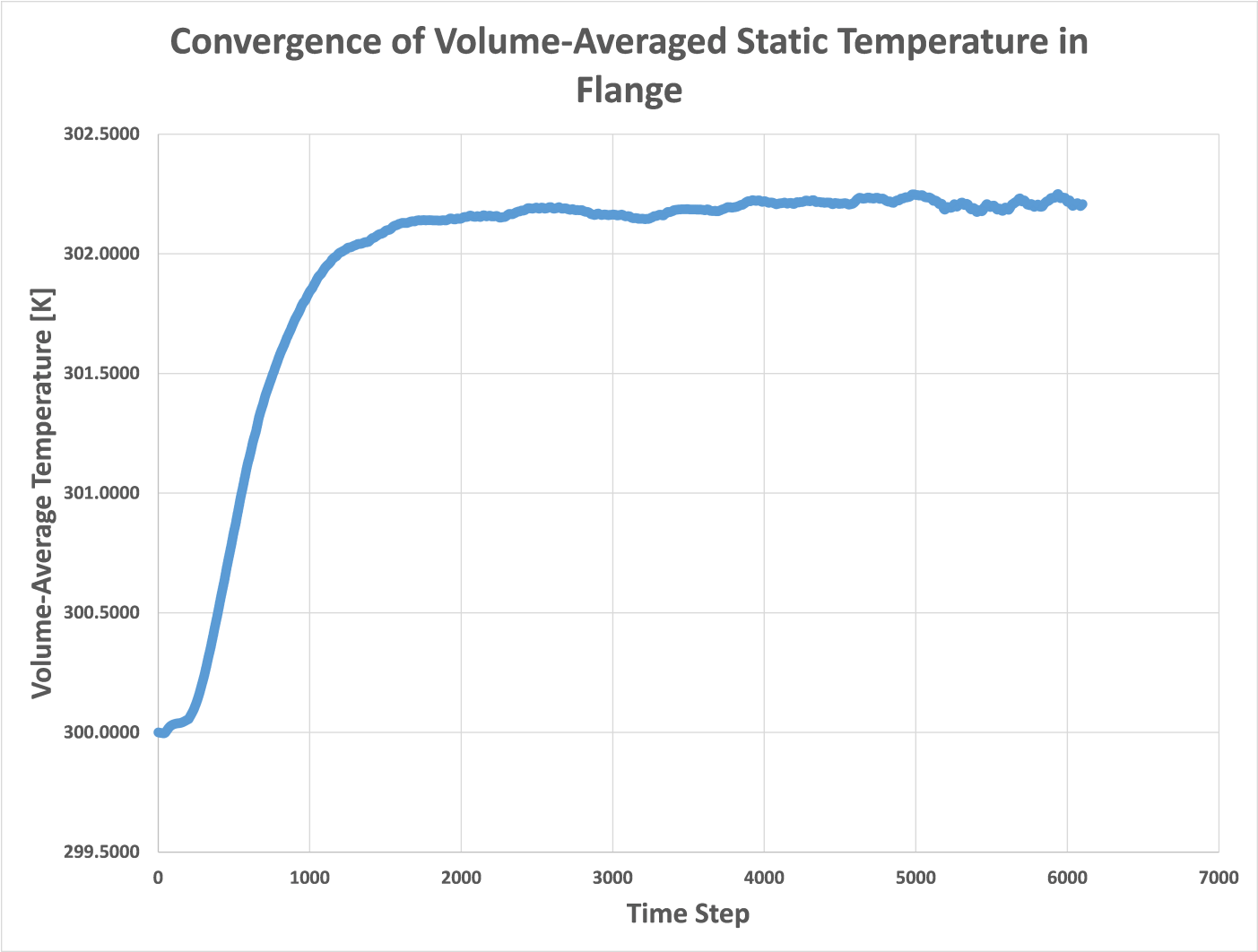

Figure C.3: Volume-averaged flange static temperature relative to time step for the laminar simulation of the current UTSI furnace and cell configuration. The time steps for this simulation ranged from starting values of 0.01 s to final values of 0.4 s and are increased as heat propagates down the cylinder to avoid solver divergence due to large temperature changes.

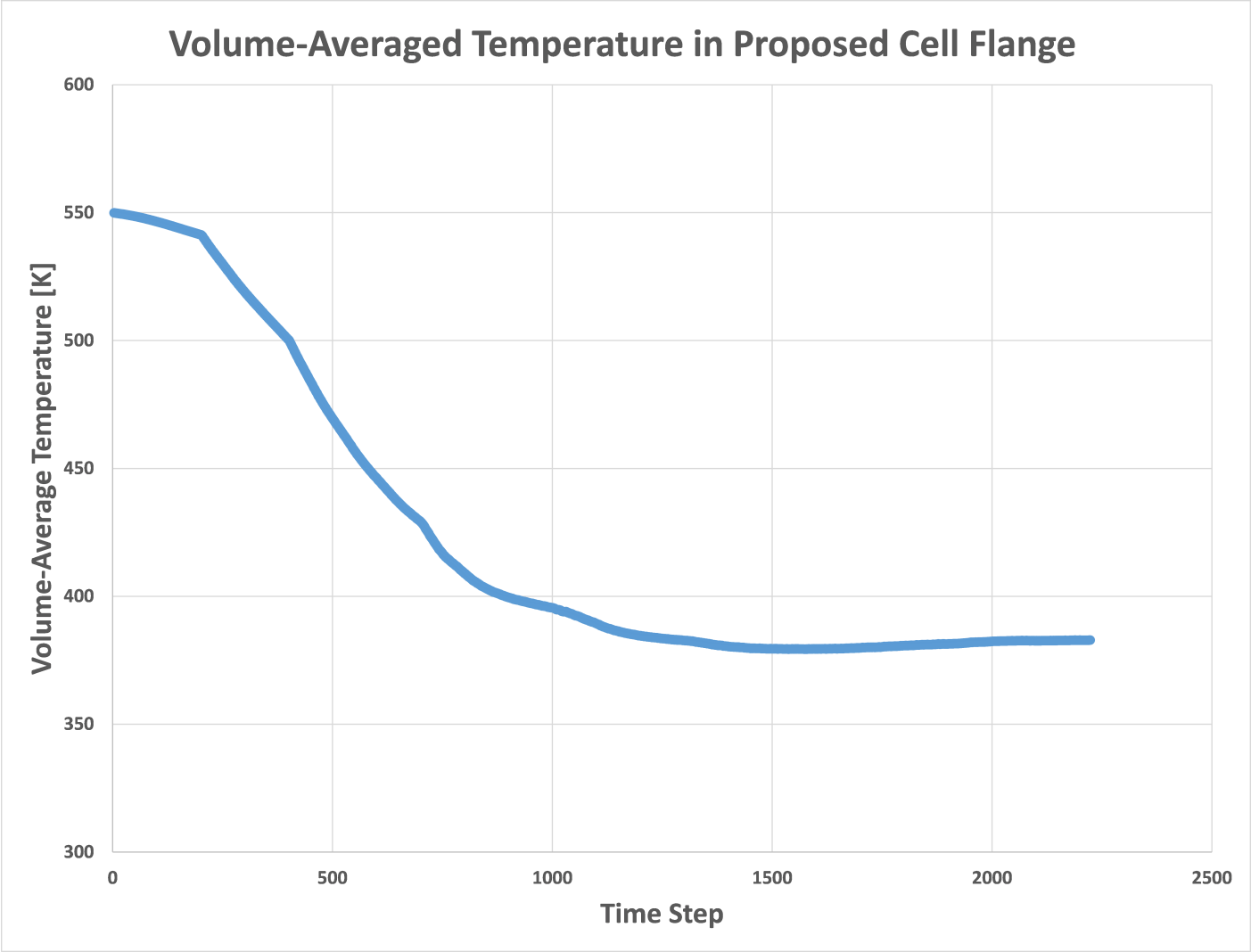

Figure C.4: Volume-averaged flange static temperature relative to time step for the laminar simulation of the proposed furnace and cell configuration. The time steps for this simulation ranged from starting values of 0.01 s to final values of 0.4 s and are increased as heat propagates down the cylinder to avoid solver divergence due to large temperature changes. This plot starts at 550K instead of 300K due to initialization conditions.

Vita

Travis Lee Johnson was born in Nashville, TN to Robert and Debra Johnson and raised in Murfreesboro, TN with his siblings Mandy and Kyle Johnson. He attended Tennessee Technological University and earned B.S. in Pure Physics before coming to the University of Tennessee Space Institute to earn a M.S. in Aerospace Engineering. After graduation, he has accepted an aerospace engineering position at Dynetics and plans to work in industry, drink tons of whiskey, and celebrate being done with school.